12-22-2023

Divergent Self-Assembly of Block Heterochiral Stereoisomer Arrays

Conor Louis O'Neill
Washington University – McKelvey School of Engineering

WASHINGTON UNIVERSITY IN ST. LOUIS

McKelvey School of Engineering
Department of Biomedical Engineering

Dissertation Examination Committee:
Jai Rudra, Chair
Kareem Azab
Jianjun Guan
Wonmuk Hwang
Meredith Jackrel
Srikanth Singamaneni

Divergent Self-Assembly of Block Heterochiral Stereoisomer Arrays

by

Conor O'Neill

A dissertation presented to
the McKelvey School of Engineering
of Washington University in
partial fulfillment of the
requirements for the degree
of Doctor of Philosophy

December 2023
St. Louis, Missouri

Table of Contents

List of Figures iv
List of Tables vii
Acknowledgments viii
Abstract x
Chapter 1: Introduction 1
1.1 Significance 1
1.2 Biomolecular Self-Assembly 2
1.3 Cross-β Fibrils and the KFE Peptide Class 5
1.4 Chirality as a Design Tool 9
1.5 Biomaterials-Based Immunomodulation 12
1.5.1 Vaccines and Immunoengineering 12
1.5.2 Immunological Effects of Nanomaterial Scaffolds 14
1.5.3 Self-Adjuvanting β-Sheet Vaccines 15
1.5.4 Biological Implications of Chirality 18
1.6 Summary 19
Chapter 2: Self-Assembly of Diblock Heterochiral Peptides into Helical Tapes 20
2.1 Abstract 20
2.2 Introduction 21
2.3 Methods 23
2.4 Transmission Electron Microscopy 27
2.5 Spectroscopic Analysis 29
2.6 Geometric Modeling of Helical Tapes 31
2.7 Small- and Wide-Angle X-Ray Scattering 34
2.8 Molecular Dynamics Modeling 36
2.9 Rheology 38
2.10 Polar Amino Acid-Substituted Variants 39
2.11 Conclusions 42
Chapter 3: Modulating Peptide Self-Assembly via Triblock Chiral Patterning 43
3.1 Abstract 43

3.2 Introduction 44
3.3 Methods 46
3.4 Scanning Transmission Electron Microscopy 51
3.5 Spectroscopic Analysis 54
3.6 Small- and Wide-Angle X-Ray Scattering 56
3.7 Molecular Dynamics Modeling 61
3.8 Rheology 64
3.9 Conclusions 67
Chapter 4: Stereoselective Coassembly of Diblock Chiral Isomer Pairs 68
4.1 Abstract 68
4.2 Introduction 69
4.3 Methods 71
4.4 Transmission Electron Microscopy 75
4.5 Spectroscopic Analysis 77
4.6 Small-Angle X-Ray Scattering 81
4.7 Rheology 82
4.8 Conclusions 86
Chapter 5: Immunomodulatory Effects of Block Chiral Peptidic Systems 87
5.1 Abstract 87
5.2 Introduction 87
5.3 Methods 90
5.4 Electron Microscopy and Structural Analysis 93
5.5 Cytotoxicity Studies 97
5.6 Serum Antibody Titers and Isotyping 98
5.7 Cellular Immune Responses 101
5.8 Conclusions 104
Chapter 6: Summary and Future Directions 105
References 107

List of Figures

Figure 1.1: Supramolecular peptide-based structures 4

Figure 1.2: Illustration of L- and D-amino acid chirality 9

Figure 1.3: Post-vaccination immune responses 12

Figure 2.1: PyMOL representations of diblock chiral KFE8 22

Figure 2.2: TEM micrographs of diblock chiral KFE8 27

Figure 2.3: TEM micrographs at alternate magnifications 28

Figure 2.4: LD and DL KFE8 tape width histogram 29

Figure 2.5: CD spectra of diblock chiral KFE8 30

Figure 2.6: FTIR spectra of diblock chiral KFE8 30

Figure 2.7: Bend and twist calculations of geometric LD KFE8 model 33

Figure 2.8: Projection of width distribution onto geometric model 33

Figure 2.9: SAXS and WAXS curves of diblock chiral KFE8 35

Figure 2.10: LD KFE8 MD model construction 37

Figure 2.11: Visualizations of LD KFE8 MD model 37

Figure 2.12: Visualization of proposed edge stitching within LD tapes 38

Figure 2.13: Rheological studies of diblock chiral KFE8 hydrogels 39

Figure 2.14: TEM micrographs of LL and LD RFE8, RFD8, and KFERFD8 41

Figure 2.15: CD spectra of LL and LD RFE8, RFD8 and KFERFD8 41

Figure 3.1: PyMOL representations of triblock chiral KFE12 45

Figure 3.2: STEM micrographs of LLL, LDL, LLD, and LDD KFE12 52

Figure 3.3: STEM micrographs of DDD, DLD, DDL, and DLL KFE12 53

Figure 3.4: Histogram of fibrillar block chiral KFE12 diameters 53

Figure 3.5: LDL and DLD KFE12 twisted fibril pitch histogram 53

Figure 3.6: CD spectra of triblock chiral KFE12 55
Figure 3.7: FTIR spectra of triblock chiral KFE12 56
Figure 3.8: SAXS Log-Log plots of triblock chiral KFE12 57
Figure 3.9: Plate thicknesses and heterogeneity factors of triblock chiral KFE12 57
Figure 3.10: Guinier fitting of triblock chiral KFE12 SAXS data 58
Figure 3.11: Debye-Bueche fitting of triblock chiral KFE12 SAXS data 59
Figure 3.12: WAXS diffraction curves and d-spacings of triblock chiral KFE12 60
Figure 3.13: Comparison of LLL KFE12 energy-minimized MD models 62
Figure 3.14: LLL KFE12 MD model ensemble fitting, comparison to LL KFE8 63
Figure 3.15: LLL KFE12 SAXS and WAXS fitting to model filament ensemble 63
Figure 3.16: Frequency-sweep rheology of triblock chiral KFE12 hydrogels 64
Figure 3.17: Calculated complex viscosities of triblock chiral KFE12 hydrogels 65
Figure 3.18: Strain-sweep rheology of triblock chiral KFE12 hydrogels 66
Figure 3.19: Calculated phase angles of triblock chiral KFE12 hydrogels 66
Figure 4.1: PyMOL representations of diblock chiral KFE8 pairs 71
Figure 4.2: TEM micrographs of diblock chiral KFE8 pairs 76
Figure 4.3: CD spectra of diblock chiral KFE8 pairs 78
Figure 4.4: FTIR spectra of diblock chiral KFE8 pairs 78
Figure 4.5: Isotope-edited IR of diblock chiral KFE8 pairs 80
Figure 4.6: SAXS Log-Log and T_{plate} P(r) plots of diblock chiral KFE8 pairs 81
Figure 4.7: Plate thicknesses and heterogeneity factors of diblock chiral KFE8 pairs 82
Figure 4.8: Strain-sweep rheology of 1:1 diblock chiral KFE8 pairs 83
Figure 4.9: Strain-sweep rheology of 3:1 and 1:3 diblock chiral KFE8 pairs 85
Figure 5.1: STEM micrographs of 10%-$OVA_{323-339}$-conjugated KFE8 systems 94
Figure 5.2: STEM micrographs of 10%-$OVA_{323-339}$-conjugated KFE12 systems 95

Figure 5.3: CD spectra of 10%-$OVA_{323-339}$-conjugated KFE8 systems 96

Figure 5.4: CD spectra of 10%-$OVA_{323-339}$-conjugated KFE12 systems 96

Figure 5.5: Cytotoxicity analysis of 10%-$OVA_{323-339}$-conjugated KFE12 systems 97

Figure 5.6: Total mouse antibody titers raised against $OVA_{323-339}$-tagged KFE systems 99

Figure 5.7: Isotyping of antibodies raised against $OVA_{323-339}$-tagged KFE systems 101

Figure 5.8: $CD4^+$ T-cell responses raised against $OVA_{323-339}$-tagged KFE systems 103

List of Tables

Table 2.1: SAXS characteristics of diblock chiral KFE8 34

Table 2.2: WAXS d-spacing of diblock chiral KFE8 35

Table 2.3: Power law fit parameters for diblock chiral KFE8 hydrogels 39

Table 3.1: SAXS characteristics of triblock chiral KFE12 59

Table 3.2: Triblock chiral KFE12 WAXS data collection and results 61

Table 4.1: SAXS characteristics of diblock chiral KFE8 pairs 82

Acknowledgments

To my parents, David and Kathy, and my brothers, Robby and Matt – this work would have never begun without the encouragement you've given, the strength you've lent, or the curiosity and persistence you fostered and then managed to tolerate. You've made every city feel like home, no matter the distance. To my fiancée Brianna, our dog Charlie, our cats Cloud and Cleo, and our rabbit Nibbler – I can't imagine the past five years without you and the joy you bring me every moment of every day. None of this would have been possible without you all and I will forever be grateful for your boundless love and support. Thank you will never be enough.

To my research mentor, Dr. Jai Rudra – your guidance has helped to define me as a scientist, the unwavering foundation you provided has made every ostensible catastrophe into nothing more than a bump in the road, and your inextinguishable sense of humor has never failed to give work a sense of life. I can't begin to thank you for giving me the opportunity to join your lab and the resources to learn, explore, and contribute to a truly fascinating field.

To my fellow Rudra lab members – it's been an absolute pleasure working with each of you. To my undergraduate research assistants, Jonathan, Lauren, Nathan, and Amanda – thank you for making mentorship so easy, for the enthusiasm you brought to every task, and for being my hands, eyes, ears, and memory when I needed it most.

Additional thanks to the National Institute of Allergy and Infectious Diseases (R01 AI130278-01A1) and the National Science Foundation (CAREER 2047517) for funding support.

Conor O'Neill

Washington University in St. Louis

December 2023

Dedicated to my parents.

ABSTRACT OF THE DISSERTATION

Divergent Self-Assembly of Block Heterochiral Stereoisomer Arrays

by

Conor O'Neill

Doctor of Philosophy in Biomedical Engineering

Washington University in St. Louis, 2023

Professor Jai Rudra, Chair

The autonomous organization of parts into ordered architectures, or biomolecular self-assembly, is an elementary natural process that defines and guides the construction and function of living organisms. This phenomenon has emerged as a potent tool for the creation of novel biomaterials, with peptide-based instances benefitting from intrinsic modularity, ease of *de novo* design and synthesis, biocompatibility, and chemical versatility. These properties enable methodical modifications that generate suprastructures with a wide variety of morphologies and functionalities, supporting a broad range of biomedical applications. Further, the chiral nature of amino acids permits synthesis of either left- or right-handed peptides; in recent years, this has advanced from complete D-substitution to the incorporation of both L- and D-residues into 'heterochiral' sequences. When peptides consist of multiple identical domains, segmenting chiral inversions according to these repeat units gives rise to 'block' heterochirality. Through combinatorial exploration of model cross-β peptides, this work furthers our understanding of chiral patterning and its powerful influence over hierarchical supramolecular assembly.

Chapter 1: Introduction

Partially adapted from: Conor L. O'Neill, Paresh C. Shrimali, Zoe E. Clapacs, Megan A. Files, Jai S. Rudra (2021). Peptide-based supramolecular vaccine systems. Acta Biomaterialia.

1.1 Significance

In nature, a narrow set of secondary structures, primarily α-helices and β-sheets, determine the conformation and function of the proteins making up living organisms. In self-assembling systems, the same associative preferences guide biomolecules into larger structures such as lipid bilayers, DNA, colloids, and mitotic spindles. Inspired by these and other naturally occurring instances of self-assembly, researchers have recognized the potential of supramolecular systems as tractable biomaterials. Owing to their inherent modularity and ease of synthesis, peptides have emerged as highly advantageous systems for exploration of the determinants guiding self-assembly, while their biological properties have led to applications as self-adjuvanting immunomodulatory scaffolds (Hernandez et al., 2023). By altering the sequence patterns and lengths of these biomolecules, a variety of distinct architectures have been achieved, including fibrils, ribbons, tapes, nanotubes, vesicles, micelles, and nanocages (Clover et al., 2020; Marini et al., 2002; O'Neill et al., 2021). Despite decades of *de novo* peptide design, the impact of greater chiral patterns, such as block heterochirality, has yet to be established and offers an additional means of controlling assembly mode, morphology, bulk material properties, biocompatibility, and immunological activity. In concert with conventional design elements, segmented heterochirality exponentially expands the array of available building blocks and represents a simple yet powerful strategy for the generation and modification of custom biomaterials.

1.2 Biomolecular Self-Assembly

Defined as the spontaneous and autonomous organization of constitutive parts into an ordered whole, self-assembly is a potent and convenient tool for peptide-, protein-, and polymer-based material fabrication (S. Zhang et al., 2002). The two primary requirements for this process are shape complementarity between individual molecules and the ability to form non-covalent interactions. These interactions, including hydrogen bond networks, electrostatics, hydrophobicity effects, and van der Waals forces, can cumulatively compose stable intermolecular associations that reliably propagate into regular supramolecular structures. For peptides in particular, the wide range of available amino acids enables strategic modification of primary sequences to produce specific secondary structures such as α-helices and β-sheets, which in turn drive their precise intermolecular arrangement. Self-assembly can also be achieved by peptidomimetics composed of a peptide domain chemically bound to other macromolecules including lipids, nucleic acids, and sugars. Like self-assembling peptides, whole protein subunits can undergo assembly via non-covalent interactions to form three-dimensional architectures. As context for the research topic of this thesis, we briefly discuss the design rules and structural determinants of several prominent peptide- and protein-based nanomaterial classes: coiled coils, β-sheets, peptide amphiphiles, and protein subunit nanoparticles.

The canonical structure of a coiled coil is a left-handed supercoil of two or more right-handed α-helices stabilized by non-covalent bonds (Woolfson, 2005; Wu & Collier, 2017). The α-helices characteristic to a coiled coil typically follow a heptad repeat pattern with its residues (‘*abcdefg*’) occupying the positions illustrated in *Figure 1.1A*, though several exceptions exist (Hicks et al., 1997; Kreitler et al., 2019; Parry, 2006). By controlling the identities of the amino acids at different locations in the heptad, the emergent structure of the coiled coil can be tailored (*Figure 1.1B,C*).

β-sheets are composed of parallel or antiparallel β-strands that are stabilized by backbone hydrogen bonding (*Figure 1.1D,E*) and assemble into sheets displaying a characteristic right-handed twist (Chothia et al., 1977; K. C. Chou et al., 1982; Pauling & Corey, 1951). β-sheets can be designed *de novo* by iterating on motifs from naturally occurring peptides, referencing the measured propensities of amino acids to be found in particular secondary structures and taking cues from established rational design methods (P. Y. Chou & Fasman, 1974; Kim & Berg, 1993; King et al., 2015; Quinn et al., 1994). β-rich self-assembling peptide morphologies can be modified by varying their amino acid sequences, although the effect is less intuitively predictable than in coiled coils. As the basis of our exploratory systems, β-sheet structure, in particular cross-β (*Figure 1.1F,G,H*), is discussed further in *Section 1.3*.

In their simplest form, peptide amphiphiles (PAs) are structural or functional peptides conjugated to lipid tails that assemble into nanofibers, bilayers, micelles, or vesicles (*Figure 1.1I*) (Berndt et al., 1995; Yu et al., 1996). The peptide components of complex PAs often contain a stabilizing β-sheet-forming domain or a polyionic domain for improved solubility. Hydrophobic packing of alkyl tails, hydrogen bonding between β-strands, and electrostatic interactions between charged amino acids drive PA assembly in aqueous environments and determine morphology, persistence length, and packing density (Cui et al., 2010; Paramonov et al., 2006; Stendahl et al., 2006). Further, when a β-sheet-forming domain in a PA contains both hydrophilic and hydrophobic amino acids, their relative positions can be altered to produce different fibril morphologies such as helical and twisted ribbons (Cui et al., 2014).

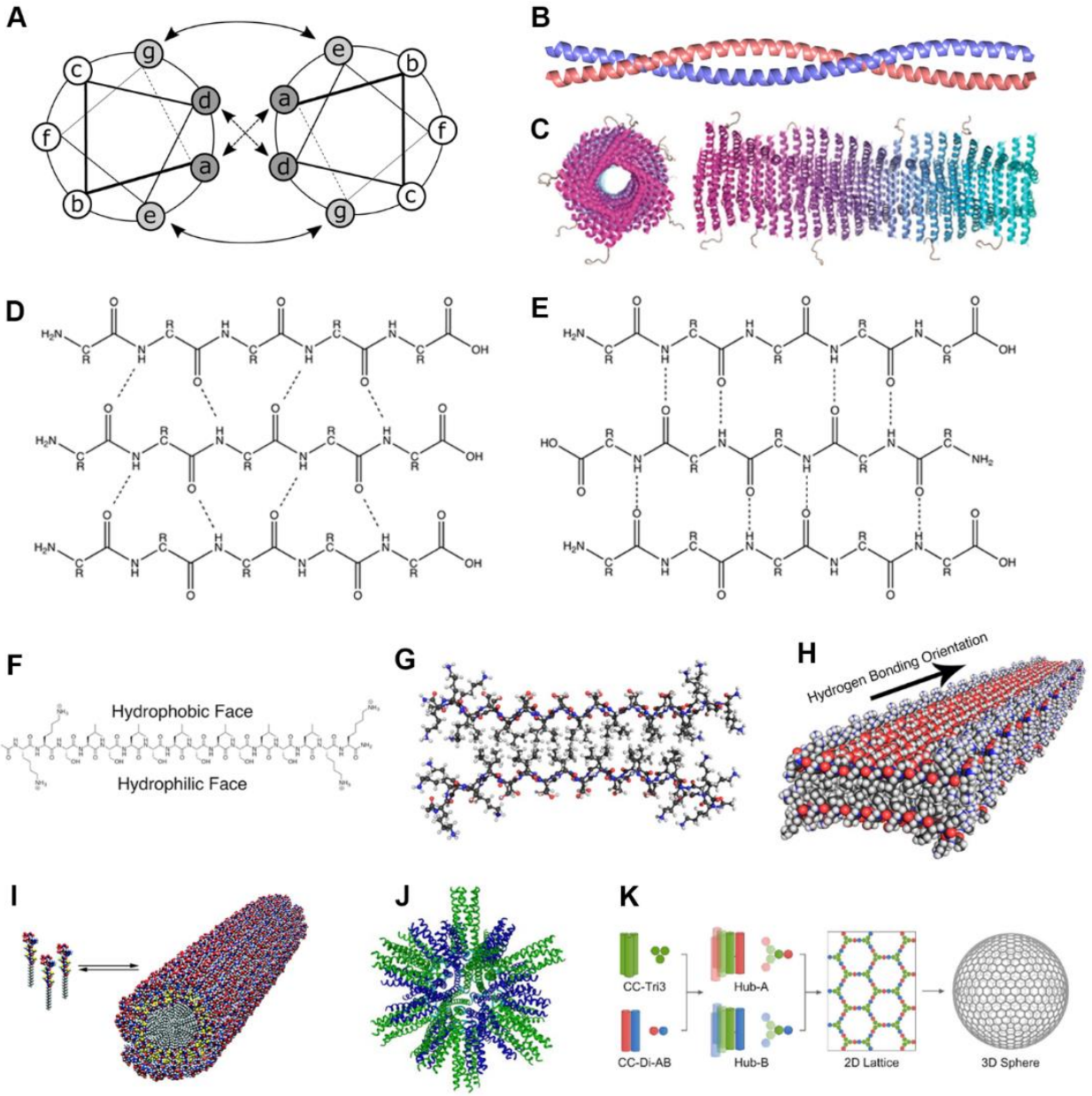

Figure 1.1. Supramolecular peptide, peptide amphiphile, and protein subunit nanoparticle structures. (A,B) Coiled coils are oligomers composed of two or more α-helices that typically display an '*abcdefg'* heptad repeat (Burkhard et al., 2000). (C) Coil29 self-assembles into filamentous nanotubes in which individual coiled coil peptides associate with their N-termini facing radially outward [*adapted with permission from (Wu et al., 2017), copyright American Chemical Society*]. β-sheets adopt either (D) parallel or (E) antiparallel orientation, both of which are stabilized by extensive hydrogen bonding networks (Richardson, 1977). β-sheets with alternating hydrophilic and hydrophobic residues are (F) facially amphipathic and (G) laminate into bilayers that (H) propagate along the hydrogen bonding axis [*adapted with permission from (Moore & Hartgerink, 2017), copyright American Chemical Society*]. (I) Peptide amphiphiles contain peptide head groups and lipid tails that assemble into cylindrical (shown) or spherical micelles [*reprinted with permission from AAAS (Hartgerink et al., 2001)*]. (J) Protein subunit nanoparticles incorporating trimeric and pentameric coiled coils assembly into polyhedral nanoparticles [*adapted with permission from (Raman et al., 2006), copyright Elsevier*]. (K) Coiled coil homotrimers covalently linked to the components of a heterodimeric coiled coil through disulfide bridges interact to form a hexagonal lattice that gives rise to closed nanocages [*adapted with permission from (Beesley et al., 2018), copyright American Chemical Society*].

In addition to secondary structures, fully folded tertiary structures can be employed to generate self-assembled nanoparticles that imitate the natural repetitiveness, geometry, size, and shape of pathogens (*Figure 1.1J,K*). Researchers have developed refined natural and synthetic protein subunits that offer the collective strength of multivalent antigen presentation, stability, and immunogenicity to induce levels of protective immunity comparable to live/attenuated vaccines (Bachmann & Jennings, 2010).

1.3 Cross-β Fibrils and the KFE Peptide Class

While early synthetic β-sheets resembled globular proteins, contemporary self-assembling β-sheet conformations are more reminiscent of amyloids (Goldschmidt et al., 2010; Hamley, 2007). As amino acid residues within a β-strand alternate between being positioned above and below the hydrogen-bonding plane, peptides with alternating hydrophobic and hydrophilic residues form facially amphipathic sheets (*Figure 1.1F*) (Mandel-Gutfreund & Gregoret, 2002; Moore & Hartgerink, 2017). In solution, cross-β strands assemble into bilayer fibrils with a hydrophobic core and hydrophilic surfaces (*Figure 1.1G,H*) (Davies & Aggeli, 2011; Fishwick et al., 2003; Pantoja-Uceda et al., 2006; Rughani et al., 2009). These are stabilized by traditional β-sheet H-bond networks, hydrophobic packing, and, if present, electrostatic interactions between charged side chains and π-π stacking of aromatic groups (Biancalana et al., 2008; Gazit, 2002; Seroski et al., 2020). Several well-characterized amphipathic peptides with various sequences have been reported, including $(AEAEAKAK)_2$ (EAK16), $(RADA)_4$ (RADA16), $(FKFE)_2$ (KFE8), QQKFQFQFEQQ (Q11), and VKVKVKVKV^{D}PPTKVKVKVKV (MAX1) (Caplan et al., 2002a; Collier & Messersmith, 2003; Leon et al., 1998; Marini et al., 2002; Schneider et al., 2002; Yokoi

et al., 2005; S. Zhang et al., 1993). Nilsson and coworkers used the prototypic sequence $(XKXE)_2$, where X denotes a hydrophobic amino acid, to show that supramolecular- and bulk-scale properties of the resulting structures can be tuned by modifying the degree of hydrophobicity and aromaticity of the X residues (Bowerman et al., 2009, 2011). Alterations to other peptides have similarly produced biomaterials with variable physicochemical properties (Haines-Butterick et al., 2007; Hong et al., 2003; Kyle et al., 2010; Lee et al., 2013b; S. Zhang & Altman, 1999).

The propensity of short polymers with distinct hydrophobic and hydrophilic regions to self-assemble into ordered structures in aqueous environments is a well-known phenomenon. This is primarily due to the hydrophobic effect, which tends to draw hydrophilic regions toward the solvent and hydrophobic regions away from the solvent and toward each other, resulting in structures like micelles, vesicles, and tubules (S. Zhang et al., 2002). However, under improper ionic strength conditions this cohesive influence can be overwhelmed by like-charge repulsion between the polar faces of interacting peptides. A convenient means of describing these competing forces is through DLVO theory (named for Derjaguin, Landau, Verwey, and Overbeek), which applies to cases in which intermolecular interactions are affected by both electrostatic and van der Walls forces (Adair et al., 2001). This theory assumes that these factors act independently of each other and that their potential energy contributions are superimposable. This approximation is relatively accurate at intermolecular distances as low as ~5 nm. A study by Lauffenburger and coworkers shows that, in agreement with DLVO theory, Ac-$(FKFE)_3$-NH_2 (KFE12) assembles if intermolecular electrical double-layer repulsion is lower than net van der Waals attraction (Caplan et al., 2000). For KFE12 at low pH (~3), DLVO theory predicts that critical coagulation concentration (CCC) is determined by anion concentration, as lysine side chains are positively charged while glutamic acid side chains are protonated and thus uncharged. Adding salt to peptide

solutions effectively screens the charges on the peptide surface, and DLVO theory predicts that KFE12 will be able to self-assemble if charges are screened to the point that the kinetic inhibition provided by electrostatic repulsion between lysine side chains falls to the order of *kT*. The theory further predicts that the CCC should depend on anion valence raised to the negative-sixth power. This study showed that relative CCC values for three salt solutions (KCl, K_2SO_4, and $K_3Fe(CN)_6$) do in fact follow this dependence. The authors also verified the prediction that KFE12 should self-assemble when there is no net charge on the peptide, as assembly was achieved when the solution was neutralized with NaOH.

As first observed for EAK16, cross-β fibril entanglement results in hydrogelation at sufficiently high concentrations (S. Zhang et al., 1993). This occurs for many $(FKFE)_n$-based peptides in pure water, including KFE8, KFE12, and KFE16 (Caplan et al., 2002a, 2002b; Leon et al., 1998). Interestingly, hydrogels composed of KFE12 fibrils are more rigid than those formed by either KFE8 or KFE16. Rigidity of KFE12 hydrogels was found to be further enhanced by increased solution ionic strength, while substituting glutamine for glutamic acid to obtain $(FKFQ)_3$ allows ionic strength to be utilized as a gelation trigger (Caplan et al., 2002a). Despite the enhanced rigidity of KFE12, KFE8 has been the primary focus of investigations into this class, presumably due to its status as the shortest KFE peptide capable of self-assembly. To this end, it has been shown that removing a single terminal residue from KFE8 (FKFEFKF and KFEFKFE) significantly altered and under some conditions entirely prevented assembly (Lee et al., 2013b). Though KFE12 and KFE16 remain highly relevant to the field, the abbreviated sequence and retained self-assembly and hydrogelation propensities of KFE8 have led to its status as the most extensively studied member of the $(FKFE)_n$-derived peptide class.

First described by Marini et al., the cross-β packing mode of our parent model peptide, KFE8, consists of anti-parallel strands with a one-residue register shift, resulting in its N-terminal phenylalanines overhanging either edge of its two laminated sheets (Marini et al., 2002). This gives rise to fibrils with widths of ~7 nm (two peptides across), helical pitch of ~19 nm, and lengths on the micron scale. The assemblies have been found to have the same left-handed supramolecular handedness as many amyloid fibers, as well as comparable dimensions (Chamberlain et al., 2000; Marini et al., 2002). Interestingly, Saiani and coworkers found that the rearranged sequence $(FEFK)_2$ assembles into β-sheet fibrils with ~4 nm diameters, as did FEFEFKFK (Mohammed et al., 2007). These results correspond to one-peptide width for $(FEFK)_2$ and FEFEFKFK fibrils, in contrast to two-peptide width for KFE8 and four-peptide width for $(FEFEFKFK)_2$ (Bowerman et al., 2009; Mohammed et al., 2007; K. Wang et al., 2005). These simple variations, caused only by inverting the positions of two complementary polar residues or by extending the sequence to include two repeat units, can directly alter the number and arrangement of peptides within cross-β assemblies, in turn modulating the supramolecular and rheological properties of resulting hydrogels. Nilsson and coworkers later continued along this line, comparing $(FKFE)_2$ to the four permuted variants FKFKFEFE, KEFFFFKE, $(KFFE)_2$, and FFKEKEFF (Lee et al., 2013a). These peptides all have identical length, amino acid composition, net hydrophobicity, and net charge, yet their ability to self-assemble and the morphology of the resulting structures vary substantially. Together, these studies demonstrate the tunability of β-sheet peptides and the range of structural properties achievable via conventional approaches to modification.

1.4 Chirality as a Design Tool

Despite the expansive catalog of strategies utilized to create these structures, the adaptable design of self-assembling peptides can be traced back to a single factor: the chemical versatility of their constitutive amino acids. While the varying degrees of hydrophobicity, charge, size, and functional groups of amino acids continue to be exploited as a means of altering self-assembly, until recently their perhaps most fundamental feature has been largely overlooked. The position of amino acid side chains, better known as chirality (*Figure 1.2*), deviates from the L-form in only a select few instances in nature. In peptide design, however, strategically incorporating D-amino acids has begun gaining prominence as a powerful tool to dramatically alter the physicochemical and biological properties of self-assembled peptide suprastructures (Garcia et al., 2018). The use of chirality in *de novo* design effectively doubles the number of available building blocks, which in turn exponentially expands the array of possible sequences.

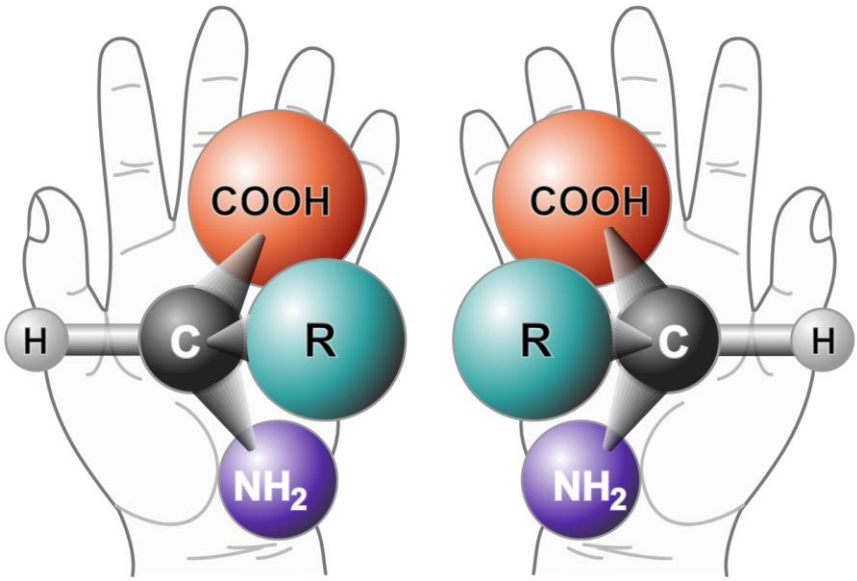

Figure 1.2. Illustration of L- and D-chiral amino acids, also referred to as left- and right-handed chirality.

The unique properties of peptides incorporating D-amino acids provide a diverse platform for their use in biological applications. Their utility is highlighted by examples demonstrating the antibacterial activity of various partially D-chiral peptides, as well as the observation that D-Trp^{8}-somatostatin is approximately eight times more potent than all-L somatostatin (Rivier et al., 1975; Sanchez et al., 2014; Wade et al., 1990). Knowledge of functional D-amino acids in natural systems also continues to expand, notably including cell wall regulation in bacteria and the neurological roles of D-Ser and D-Asp in mammals (Cava et al., 2011; Genchi, 2017). Within peptide self-assembly, the resistivity of D-peptides to proteolysis has been well-documented, presenting the opportunity to tune degradation rates of scaffolds by doping L-peptides with their enantiomers (Luo et al., 2008; Nagy et al., 2011; Swanekamp et al., 2014; Wade et al., 1990). Other relevant studies into D-amino acids have included the impact of stereocomplexation on enantiomeric mixtures, an associated enhancement of mechanical rigidity in hydrogels composed of coassembled systems, and explorations of point-mutated heterochiral peptides (Garcia et al., 2018; Marchesan, Easton, et al., 2012; Marchesan et al., 2014; Nagy et al., 2011).

As predicted by Pauling and Corey, several D-peptides have been shown to coassemble with their L-enantiomers to generate architectures with structures and properties unlike those formed by either peptide individually (Nagy et al., 2011; Pauling & Corey, 1953; Swanekamp et al., 2012). This includes KFE8, with a subsequent paper depicting the proteolytic stability of 1:1 LL:DD KFE8, along with those of pure LL KFE8, pure DD KFE8, and 3:1 LL:DD KFE8 (Swanekamp et al., 2014). As proteases selectively recognize and cleave L-amino acids, peptides containing D-amino acids exhibit reduced degradability, carrying strong implications for their use as hydrogel depots or vaccine carriers *in vivo* (Swanekamp et al., 2014). Racemic coassembly has been similarly demonstrated for a self-assembling β-hairpin peptide (MAX1) and its enantiomer

(DMAX1) by Schneider and coworkers, who found that these assemblies exhibited enhanced rheological strength dependent on the relative proportions of the stereoisomers (Nagy et al., 2011; Nagy-Smith et al., 2017).

Beyond fully substituting for the L-amino acids of known self-assembling peptides, partial replacement with D-amino acids is capable of significant alteration to the underlying structure of assemblies (Clover et al., 2020; Melchionna et al., 2016). Short heterochiral peptides have been extensively studied by Marchesan and coworkers, revealing a conceptual framework that describes the assembly behaviors of homo- and heterochiral tripeptides composed of hydrophobic amino acids (Garcia et al., 2018; Marchesan et al., 2014, 2015; Marchesan, Waddington, et al., 2012; Melchionna et al., 2016; Vargiu et al., 2016).

These studies demonstrate that even well-established and extensively studied peptidic systems can be entirely transformed without altering peptide length, charge, hydrophobicity, or side chain identity. Building upon these illustrations of partial D-substitution and stereocomplexation between enantiomeric sequences, this thesis work aims to explore segmented substitution patterns, which we refer to as ‘block heterochirality.’ As we improve our understanding of the interactions responsible for these phenomena, the breadth of previously unobserved packing modes and morphologies continues to expand along with their potential applicability as tailorable immunomodulators.

1.5 Biomaterials-Based Immunomodulation

1.5.1 Vaccines and Immunoengineering

The body shields itself from infectious threats through a series of concerted immune responses. During initial exposure or vaccination, dendritic cells (DCs), macrophages (MΦs), and B cells, collectively known as antigen-presenting cells (APCs), internalize antigens and undergo maturation upon encountering danger signals (Hubbell et al., 2009). These mature APCs then display antigens to $CD8^+$ and $CD4^+$ T cells through major histocompatibility complexes (MHCs) I and II, respectively, in draining lymph nodes (dLNs) and secondary lymphoid organs (*Figure 1.3*). Antigen-specific B cells engage with $CD4^+$ T cells to engender various helper T-cell (T_H) phenotypes that initiate and polarize B-cell clonal proliferation to generate plasma cells or memory B cells (Batista & Harwood, 2009). Together, these T- and B-cell pools form the basis of lasting immunological memory.

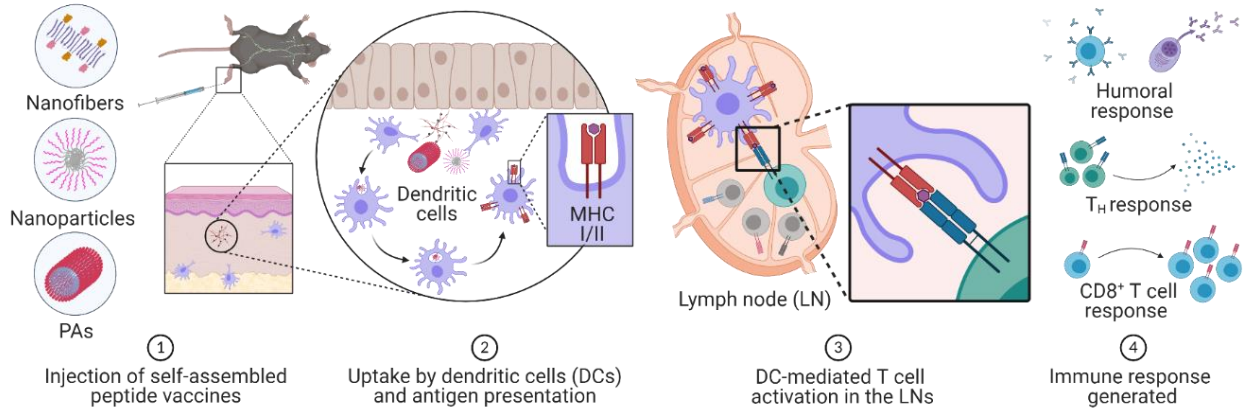

Figure 1.3. Evolution of immune responses following supramolecular peptide-based vaccine delivery. After vaccine administration [1], tissue resident APCs such as DCs and MΦs internalize the constructs and process them through either the exogenous or endogenous pathway [2] to present the antigenic epitopes on MHC II or MHC I molecules, respectively. The antigen-laden APCs then migrate to the dLNs for antigen presentation to $CD4^+$ or $CD8^+$ T cells. The interaction between MHC molecules and TCRs is supported by costimulatory signals, including ligand/receptor interactions and cytokine signaling that [3] enhance T-cell responses and drive differentiation. T_H cells then direct further immune activation through cytokine signaling and interaction with B cells and $CD8^+$ T cells. Activated B cells interact with antigen-specific T cells and differentiate into plasma cells that produce long-lived antibody responses. Crosstalk between $CD4^+$ and $CD8^+$ T cells [4] leads to the production of cytotoxic T lymphocytes that detect and eliminate infected cells. Created with BioRender.com.

Immunoengineering aims to improve the efficacy of vaccines and therapeutics to combat infectious diseases, cancers, and autoimmune conditions. While broadly acting substances may effectively stimulate the innate immune system, their lack of specificity may impede induction of anamnestic immunological memory. Therefore, it is critical to consider the nature of the pathogenic agent, the pathogenesis of the disease, and the type of protection required when engineering vaccines or immunotherapies.

Vaccination aims to generate lasting immunological memory against both infectious and non-infectious diseases and has proven to be one of the most successful public health initiatives in history (Lahariya, 2016). Despite this, vaccines for a number of intractable diseases like malaria, human immunodeficiency virus (HIV), cancers, and autoimmune diseases have not yet been identified, tested, and approved by regulatory bodies (Cable et al., 2020). To date, approximately 100 vaccines have been licensed for clinical use in the United States, most of which utilize inactivated or attenuated pathogens (United States Food and Drug Administration, 2020). While whole-organism vaccines stimulate robust and long-lived immunity, their potential to cause undesirable side effects has prompted the use of subunit vaccines that contain only antigenic proteins or epitopes derived from the target pathogen (Vetter et al., 2018). These subunit vaccines address many of the disadvantages of traditional formulations; however, their reduced immunogenicity necessitates co-administration of adjuvants to elicit immune responses sufficient for memory formation. As adjuvants are themselves reactogenic and often poor T-cell immunopotentiators, significant effort has been devoted to developing alternative means of improving subunit vaccine efficacy (Villarreal & Casale, 2020).

1.5.2 Immunological Effects of Nanomaterial Scaffolds

As our knowledge of immunology expands, the exploitation of specific pathways continues to come into focus as a key aspect of vaccines and immunotherapies. A major goal of the cross-disciplinary field of immunoengineering is to exert spatial and temporal control over the activity of the immune system, primarily by using rationally designed biomaterials to produce safer vaccines and probe understudied immune pathways (Hotaling et al., 2015; Hubbell et al., 2009). While many commonly used polymeric, metallic, and ceramic biomaterials are immunologically inert, biologically derived macromolecules such as proteins, peptides, and peptidomimetics are prone to immune recognition (Sahoo et al., 2018; Zhao et al., 2017). These biomolecules can serve as antigens, delivery vehicles, and adjuvants in subunit vaccines to localize release, protect therapeutics from proteolytic degradation, and induce the appropriate immune phenotype required for protection. Beyond their applications as prophylactic or therapeutic vaccine carriers, biomaterial-based co-delivery of multiple pharmacological agents or innate immune system-activating signals can be used as efficient combinatorial therapies (Dellacherie et al., 2019; Eppler & Jewell, 2020).

Due to their chemically defined nature, ease of *de novo* design and synthesis, biocompatibility, and degradability, peptides serve as useful building blocks for fabricating biomaterials with various physicochemical properties and functionalities (Mart et al., 2006). Using the diversity of available natural and non-natural amino acids, peptides can be programmed to self-assemble into hierarchical architectures, notably fibrils, tapes, ribbons, nanotubes, vesicles, micelles, and nanocages (Mandal et al., 2014). The chemical versatility of their constitutive amino acids grants peptides a high degree of tunability, permitting sequence modifications that alter assembly, target specific cells or organs, impede enzymatic degradation, impart stimulus-responsiveness, or enable

conjugation to other organic or inorganic molecules. In the context of vaccines, the multivalency of peptide suprastructures facilitates repetitive presentation of antigens on their surface, leading to enhanced uptake by immune cells and higher antibody titers relative to monovalent antigens (Zacco et al., 2015). This self-adjuvancy allows for the marginal efficacy of subunit vaccines to be overcome without the use of toxic adjuvants and reduces the total amount of antigen required to attain protective immunity, both of which help avoid deleterious side effects.

1.5.3 Self-Adjuvanting β-Sheet Vaccines

While numerous tissue engineering applications have confirmed that self-assembling β-sheet fibrils are well-tolerated, Rudra et al. reported that fibrils functionalized with immunogenic epitopes are self-adjuvanting and lead to high antibody titers against the presented antigens (Rudra et al., 2010). When the glutamine-rich peptide Q11 was conjugated to $OVA_{323-339}$ (ISQAVHAAHAEINEAGR), the assemblies induced antibodies levels comparable in magnitude and persistence to $OVA_{323-339}$ administered in complete Freund's adjuvant (CFA). Further, unlike the exogenously adjuvanted $OVA_{323-339}$ formulation, the Q11-$OVA_{323-339}$ fibrils did not cause local inflammation at the injection site. Malaria model experiments supported that this self-adjuvancy is highly relevant to vaccine development, eliciting durable and protective anti-malaria antibodies (Rudra, Mishra, et al., 2012). Mechanistic studies revealed a critical role for $CD4^+$ T cells in the observed humoral response, which was independent of the TLR2, TLR5, and NALP3 inflammasome pathways (Rudra, Mishra, et al., 2012; Rudra, Sun, et al., 2012). While antibodies are relatively easy to generate, the activation threshold for efficient priming of $CD8^+$ T cells is higher due to costimulatory requirements from APCs (Carpenter et al., 2016). Intranasal delivery of Q11 nanofibers bearing the MHC I epitope $OVA_{257-264}$ (SIINFEKL) were found to effectively

protect against infection with a mouse-adapted human influenza strain (PR8) expressing $OVA_{257-264}$ (Chesson et al., 2014). Si et al. demonstrated that, compared to parenteral vaccination, intranasal delivery of Q11 nanofibers bearing the influenza acid polymerase epitope $PA_{224-233}$ (SSLENFRAYV) induced higher levels of lung-resident effector and memory $CD8^+$ T-cell responses and protected mice against an influenza challenge (Si et al., 2018). The inclusion of the pan-DR T-cell epitope PADRE into IL-17-Q11 nanofibers increased anti-IL-17 antibody production while reducing imiquimod-induced psoriasis in mice without added adjuvants (Alexander et al., 1994; Shores et al., 2020). Further, the declining antibody titers over time could be recovered by a recall exposure to the IL-17-PADRE-Q11 construct. In addition to eliciting antibodies against foreign proteins, peptide nanofiber vaccines targeting autologous molecules like TNF-α can overcome B-cell tolerance and generate antibodies that prevent inflammation (Mora-Solano et al., 2017). As an alternative to monoclonal antibody therapies, active immunization is comparatively cost-efficient, produces lasting effects, and elicits a polyclonal response that includes different isotype specificities that can enhance the breadth of protection. Full-length proteins (e.g., GFP) can be bound to fibers using phosphonate-cutinase or other orthogonal chemistries to expand the repertoire of possible functional antibodies against pathogens (Hudalla et al., 2013). In lieu of chemistries that only permit functionalization of mature fibrils, controlling the rate of β-sheet formation enables multiple full-length proteins to be incorporated without impeding self-assembly (Hudalla et al., 2014).

Comparable immunological results were obtained when antigens were displayed by alternative β-sheet-forming peptides such as KFE8, EAK16, RADA16, Nap-$G^DF^DF^DY$, and $(RVQV)_3$ (Z1), suggesting that self-adjuvancy is an intrinsic feature of this materials class (Chesson et al., 2014, 2018; Ding et al., 2016; Grenfell et al., 2015; X. Li et al., 2020; Rudra et al., 2016; Rudra, Sun, et

al., 2012; Y. Wang et al., 2019; C. Yang et al., 2018; H. Zhang et al., 2017). Nanofiber vaccines can carry a wide array of antigens, including bacterial or viral epitopes and addictive drug haptens. Fibrils composed of KFE8 linked to a cocaine hapten modified at the P3 site have been found to stimulate anti-cocaine antibody production without the need for exogenous adjuvants (Rudra et al., 2016). This significantly decreased cocaine-induced hyperactivity while avoiding the potential systemic toxicity associated with the strong adjuvants required by alternative strategies.

One considerable advantage of peptide nanofibers is their ability to form self-supporting and injectable hydrogels at high concentrations, a property that can be exploited for simultaneous presentation of antigens and sustained release of immunomodulatory compounds. For example, a hydrogel formed by KFE8 admixed with the West Nile virus immunoprotective envelope protein domain III (EIII) resulted in significantly higher anti-EIII antibody titers in mice than free EIII co-administered with alum (Friedrich et al., 2016). Its effectiveness was also supported by reduced weight loss and a threefold higher survival rate (60%). Woodrow and coworkers investigated optimized charge distribution and density to modulate the self-assembling properties of the model sequence Z1 and its derivatives with substituted residues or terminal groups (H. Zhang et al., 2017). These peptides assembled at lower concentrations than similar amphipathic peptides, demonstrated increased hydrogel mechanical strength, and elicited robust $CD8^+$ T-cell responses. In contrast to *de novo* designed peptides, the naturally occurring β-sheet-forming amyloidogenic peptide I10 (SNNFGAILSS) can trigger NF-κB signaling without significantly affecting cell viability in a HEK reporter cell line expressing the human heterodimer TRL2/6 (Al-Halifa et al., 2020; Babych et al., 2018). Beyond infectious disease and addiction models, a number of β-sheet-rich peptide constructs have been used as adjuvants in a variety of cancer models to minimize

tumor burden (Huang et al., 2012; S. Li et al., 2020; X. Li et al., 2020; Luo et al., 2017; Mohammadi et al., 2021; Z. Wang et al., 2017, 2020).

1.5.4 Biological Implications of Chirality

While selecting from naturally occurring L-amino acids allows for control of physicochemical properties such as charge, hydropathy, and polarity, incorporating their D-enantiomers further enriches this diversity and impacts self-assembly behavior (Appavu et al., 2015; Clover et al., 2020; Gao et al., 2012; Luo et al., 2008; Melchionna et al., 2016; Nagy et al., 2011; Swanekamp et al., 2012; Y. Wang et al., 2019; Z. Wang et al., 2020; Xu et al., 2019). The geometric change in backbone-side chain arrangement of D-enantiomers makes them resistant to proteases, preventing *in vivo* degradation (Luo et al., 2008; Swanekamp et al., 2014). To demonstrate this, Nilsson and coworkers exposed L- and D-KFE8 fibrils to three proteases (chymotrypsin, trypsin, and proteinase K) and found that while the L-KFE8 fibrils were ~50% degraded after 24 hours and ~95% degraded after five days, the D-KFE8 fibrils were only marginally degraded after five days (Swanekamp et al., 2014). Adjusting the stoichiometric ratio (1:1 or 3:1 L/D) of the enantiomers allowed for additional control over the proteolytic stability of the hydrogels. Biostability and biodistribution studies in mice demonstrated that L- and D-enantiomers of Nap-GFFYGRGD degrade at different rates in plasma (95% or L-enantiomer and 17% of D-enantiomer digested after 24 hours) and preferentially accumulate in different organ systems (C. Yang et al., 2015). In a study comparing L- and D-KFE8 fibrils bearing $OVA_{323-339}$, the improved *in vivo* stability of the D-enantiomers was associated with enhanced and persistent antibody responses while retaining the non-inflammatory status of the L-enantiomers (Appavu et al., 2015).

1.6 Summary

The KFE peptide class not only presents a synthetic avenue for vaccine development, but also provides a framework for the study of chirality effects that fundamentally alter intermolecular forces and resultant structural properties. The presented work builds upon the aforementioned studies by advancing our understanding of chiral patterning in the form of block heterochirality. This effort has generated an expansive array of assemblies formed by systems utilizing this concept, including all combinatorial instances of diblock (KFE8) and triblock (KFE12) heterochirality. Further, we examine the stereoselective coassembly or self-sorting propensities observed for KFE8 analog pairs, as well as their emergent supramolecular morphologies and bulk properties. In addition to these structural analyses, we assess the biological implications of block heterochirality and attempt to resolve the roles played by chiral composition and morphology in regulating cytocompatibility, immunogenicity, and degradability. The outcome of these studies lays the groundwork for a peptide library that enables tailoring of physicochemical and biological properties through variable sequences, lengths, chiral patterns, and component multiplicity.

Chapter 2: Self-Assembly of Diblock Heterochiral Peptides into Helical Tapes

Partially adapted from: Tara M. Clover, Conor L. O'Neill*, Rajagopal Appavu, Giriraj Lokhande, Akhilesh K. Gaharwar, Ammon E. Posey, Mark A. White, Jai S. Rudra (2020). Self-Assembly of Block Heterochiral Peptides into Helical Tapes. Journal of the American Chemical Society.[1] (*equal contributors)*

2.1 Abstract

Patterned substitution of D-amino acids into the primary sequences of self-assembling peptides influences molecular-level packing and supramolecular morphology. We report that block heterochiral analogs of the model amphipathic peptide KFE8 (Ac-FKFEFKFE-NH_2), composed of FKFE repeat motifs with opposite chirality, assemble into helical tapes with dimensions greatly exceeding those of their fibrillar homochiral counterparts. At sufficient concentrations, these tapes form hydrogels with significantly reduced storage moduli but retain the shear-thinning behavior and consistent mechanical recovery of the homochiral analogs. Varying the identity of charged residues (FRFEFRFE and FRFDFRFD) produced similarly sized non-helical tapes, while a peptide with non-enantiomeric L- and D-blocks (FKFEFRFD) formed helical tapes closely resembling those of the heterochiral KFE8 analogs. A proposed energy-minimized model suggests that a kink at the interface between L- and D-blocks leads to the assembly of flat monolayers with non-identical surfaces that display alternating stacks of hydrophobic and charged groups.

2.2 Introduction

Self-assembling oligopeptides with alternating polar and non-polar residues are attractive minimal systems that assemble into highly soluble fibrillar scaffolds with diverse applications in engineering and medicine (Bowerman & Nilsson, 2012; Hamley, 2011). The model cross-β fibrillizing peptide KFE8 (Ac-FKFEFKFE-NH_2) and its variants have been extensively applied to better understand the roles of hydrophobicity, charge, ionic strength, sequence length, residue patterning, and functionalization on molecular self-assembly and resulting morphological and bulk material properties (Bowerman & Nilsson, 2012; Lee et al., 2013a, 2013b; Marini et al., 2002; Zhou et al., 2016).

An established method of controlling scaffold degradation is to incorporate peptides composed of 'non-natural' D-amino acids (Luo & Zhang, 2012; Melchionna et al., 2016). Studies using homochiral (all-L or all-D) enantiomers of self-assembling peptides have demonstrated differences in fibril handedness, proteolytic susceptibility, and bioactivity (Appavu et al., 2015; Marchesan et al., 2013; Swanekamp et al., 2014; Vargiu et al., 2016). Further, rippled β-sheets consisting of alternating L- and D-peptides have been shown to form hydrogels with enhanced viscoelasticity, while studies comparing homochiral and heterochiral combinations of syndiotactic and isotactic peptides found that the heterochiral combinations exhibited faster gelation kinetics but reduced viscoelasticity (Nagy et al., 2011; Swanekamp et al., 2012; Taraban et al., 2012).

As opposed to complete substitution, selective incorporation of D-amino acids is a facile approach to modulate the physicochemical and biological properties of peptide-based hydrogels (Garcia et al., 2018; Marchesan et al., 2014; Schneider et al., 2002). Recent findings by Marchesan and coworkers have revealed a conceptual framework describing the assembly behaviors of homochiral and heterochiral tripeptides consisting of hydrophobic amino acids (Garcia et al., 2018;

Marchesan et al., 2014, 2015). These studies, among many others, have laid the foundation for further exploration of chirality, in particular patterned chirality, as a design tool to control emergent properties of peptide biomaterials.

In this work, we investigate the impact of block chirality patterns on peptide self-assembly and resultant supramolecular and bulk material properties by inverting the chirality of either one or both FKFE motifs of KFE8 with (D-Phe)-(D-Lys)-(D-Phe)-(D-Glu) (notated 'fkfe'). This method generates four block chiral analogs: the well-established homochiral analogs LL (FKFEFKFE) and DD (fkfefkfe) and the 'diblock heterochiral' analogs LD (FKFEfkfe) and DL (fkfeFKFE) (*Figure 2.1*). We report that this process, altering the chirality of a single repeat unit, fundamentally alters the packing mode, supramolecular morphology, and hydrogel viscoelasticity of KFE8.

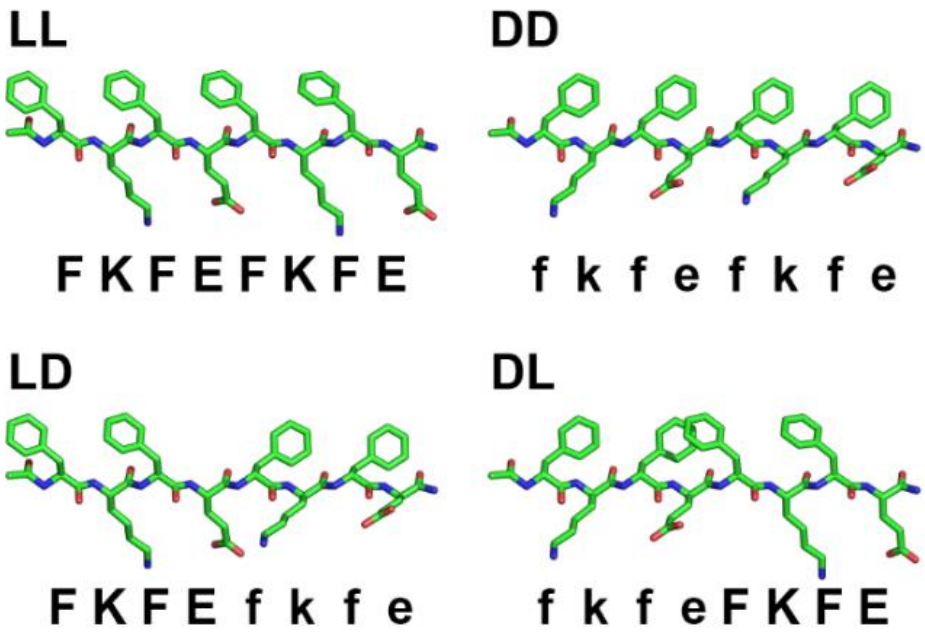

Figure 2.1. Structures of the diblock homochiral (LL, DD) and diblock heterochiral (LD, and DL) analogs of KFE8, collectively referred to as the 'block chiral' analogs of KFE8.

2.3 Methods

Peptide Synthesis. All peptides were synthesized using standard Fmoc Chemistry on a CS Bio (Menlo Park, CA) CS336X solid phase peptide synthesizer. Rink Amide MBHA resin from Novabiochem (Waltham, MA) was swelled in dry DMF for 1 hour, and peptides were double coupled using HBTU (O-(benzotriazol1-yl)-N,N,N′,N′-tetramethyluronium hexafluorophosphate) and HOBt (1-Hydroxybenzotriazole) chemistries. Peptides were cleaved from the resin using a cocktail of trifluoroacetic acid (TFA), triisopropylsilane (TIS), and water (95:2.5:2.5). The crude peptide was pelleted using centrifugation, resuspended in cold diethyl ether, washed five times, lyophilized, and stored at -20°C.

Peptide Purification and Identification. Crude synthesis products were solubilized in 1:1 acetonitrile (ACN)/TFA and purified to >90% purity by reverse-phase HPLC using an Agilent (Santa Clara, CA) RP-C18 column (Zorbax SB-C18, 21.2x150 mm, 5 μm) on a Varian Pro-Star system with ACN/H_2O gradients. For semi-preparative purification, a gradient of water and ACN (0.1% TFA) at a flow rate of 18 mL/min was used and was monitored by UV absorbance at 214 and 254 nm. The fractions were collected and lyophilized. Purity was confirmed by analytical HPLC using a Agilent RP-C18 column (Poroshell 120 SB-C18, 4.6 x 150 mm, 2.7 μm). Peptide mass was confirmed by MALDI-TOF-MS using a α-cyano-4-hydroxycinnamic acid matrix from Bruker Daltonics (Billerica, MA).

Peptide Self-Assembly. Each peptide was weighed and dissolved in 1:1 ACN/H_2O at 1.0 mM. The tubes were vortexed to ensure complete dissolution of the peptide and separated into 500-μL aliquots. The solutions were serially diluted to yield 0.5 mM and 0.25 mM solutions. All tubes were frozen at -80°C, lyophilized, and stored at 4°C as dry powders. Self-assembly was achieved

by dissolving thawed aliquots in the appropriate amount of water to produce solutions at 1.0 mM, 0.5 mM, or 0.25 mM.

Transmission Electron Microscopy. Solutions of KFE8 (0.25 mM in DI water) were applied directly to a 200-mesh carbon coated copper grid by inversion onto a 10-μL sample droplet for 30 seconds. Excess sample was blotted using filter paper. The grids were stained with 2% uranyl acetate for 60 seconds and excess stain was removed using filter paper. KFE8 images were acquired using a JEOL (Akishima, Japan) JEM-2100 transmission electron microscope (TEM) with an accelerating voltage of 200 kV. RFE8, RFD8, and KFERFD8 images were acquired with a JEOL JEM-1400 TEM with an accelerating voltage of 120 kV.

Width and Pitch Measurements. TEM images were analyzed using ImageJ. Length scales were set using JEOL software-generated scale bars. Width measurements were performed by manually drawing lines perpendicular to nanofiber or tape edges, and their lengths were calculated by ImageJ. Pitch measurements were similarly performed in ImageJ by manually drawing lines between alternating helical turns.

Circular Dichroism. CD spectra of the KFE8 solutions (0.25 mM in water) were recorded on a Jasco (Hachioji-shi, Japan) J-815 circular dichroism spectrometer. Spectra of the peptide solutions were collected at 20°C in a 1-mm quartz cuvette between 260 and 190 nm using a bandwidth of 1.00 nm, 0.5-nm step, and 2-second averaging time per step. A graphing software was used to subtract background and convert to molar ellipticity.

Fourier-Transform Infrared Spectroscopy. Fourier-transform infrared (FTIR) spectra were measured with a Thermo Nicolet (Austin, TX) FTIR Nexus spectrometer equipped with a Smart Performer single-reflection ATR accessory and a Ge crystal sample stage. For each construct,

lyophilized peptide was loaded onto the FTIR sample stage and hydrated with 0.5 µL of ultrapure deionized water. A background spectrum of air was collected before sample measurement according to the standard operating procedures for the instrument, and a water spectrum was measured and subtracted from each sample spectrum. Spectra were checked for an appropriate ratio of amide I and II band intensity, low noise, and the absence of other artifacts to confirm proper data acquisition and buffer/water subtraction. All spectra represent the accumulation of 264 scans with a step size of 4 cm^{-1}. All measurements were repeated at least three times using three independent sample preparations, and variation across sample preparations was found to be insignificant. Data were analyzed using Thermo Scientific (Waltham, MA) GRAMS/AI software. Second derivative spectra were calculated from the absorbance spectra in the amide I region using a third-order Savitzky-Golay filter with a nine-point window. Second derivative spectra were then inverted and baseline-corrected assuming flat baseline segments connecting minima between 1710 and 1610 cm^{-1}. Inverted second derivative spectra peaks between 1710 and 1610 cm^{-1} were then fit with six or seven Gaussian curves, as determined by Akaike Information Criterion (AIC). The area under each fitted peak was calculated and the positions of the peaks were compared to values reported in the literature (Barth, 2007; Dong et al., 1990; Jackson & Mantsch, 1995).

Small- & Wide-Angle X-ray Scattering. SAXS data of the KFE8 solutions (1 mM and 0.5 mM in water) were collected using a Rigaku (Woodlands, TX) BioSAXS-1000 camera on an FRE++ X-ray generator with an ASC-96 Automated Sample Changer held at 10°C. A matching buffer was collected for each sample. Processing was performed in SAXSLab (Rigaku) and SAXNS-ES (https://xray.utmb.edu/SAXNS). WAXS data were collected at room temperature using 10-mM KFE8 solutions and matching buffers. Solutions were pipetted into a 2-mm MiTeGen (Ithaca, NY) MicroRT polyester capillary on a Rigaku R-AXISIV++ and processed using Fit3D, SAXNS-ES,

and Primus to merge with the SAXS data. Analysis was performed in Primus and gnuplot for curve fitting.

Molecular Dynamics Modeling. The MD KFE8 model developed by Dr. Wonmuk Hwang and coworkers (Marini et al., 2002) was used as starting model for LD model construction. A single strand of LD was created from the KFE8 peptide by changing the handedness of residues 5-8 (FKFE) from L- to D-amino acids. This was accomplished by fixing atoms within the amino acid backbone and exchanging the R-group and the Cα-hydrogen via a 120° rotation about the peptide axis. A protofilament consisting of 24 LD KFE8 β-strands was built using the symmetry of an ideal β-sheet without twist. The model was then energy minimized using CNS (Brünger et al., 1998) before performing MD equilibration using the WAXSiS server (Chen & Hub, 2014; Knight & Hub, 2015).

Rheology. Shear-thinning properties of the block chiral KFE8 hydrogels (10 mM in water) were measured using a TA Instruments (New Castle, DE) Discovery HR-2 rheometer equipped with a parallel-plate geometry 20 mm in diameter. The hydrogels were loaded into the rheometer and a shear rate sweep of 0–100 s^{-1} was performed at room temperature. Time sweep tests were performed on the gels to calculate their storage moduli. Peak storage modulus values were measured after subjecting the gels to a constant strain of 1% for 30 minutes. Mechanical recovery was assessed by monitoring storage modulus changes at low (1%) and high (100%) strain values. All analysis was performed using TRIOS software (TA Instruments), with viscosity versus shear rate curves being fit to a power law model.

2.4 Transmission Electron Microscopy

Various self-assembled morphologies have been reported (e.g., fibrils, tapes, and ribbons) with diameters typically ranging from 3–20 nm and lengths on or near the micron scale (Aggeli et al., 2001; Bowerman & Nilsson, 2012; Lee et al., 2013a; Marchesan, Waddington, et al., 2012; Marini et al., 2002; Schneider et al., 2002; S. Zhang et al., 1993). Transmission electron microscopy (TEM) images indicate that the homochiral peptides LL and DD reliably form nanofibers with dimensions (LL: ~8.1 ± 0.3 nm width, ~19 nm pitch; DD: ~7.9 ± 0.3 nm width, ~20 nm pitch) (*Figure 2.2A,B*) in agreement with published values (Marini et al., 2002; Swanekamp et al., 2012). In contrast, the LD and DL peptides assemble into supramolecular helices (*Figure 2.2C,D*) often appearing to possess pitch values of ~900–1200 nm. A broad width distribution was observed (~108 ± 55 nm), however, ~90% of tapes were 50–150 nm wide with an average of ~92 ± 22 nm (*Figure 2.4*). The helical morphology and approximate dimensions of the heterochiral assemblies were confirmed using two independent synthesis batches.

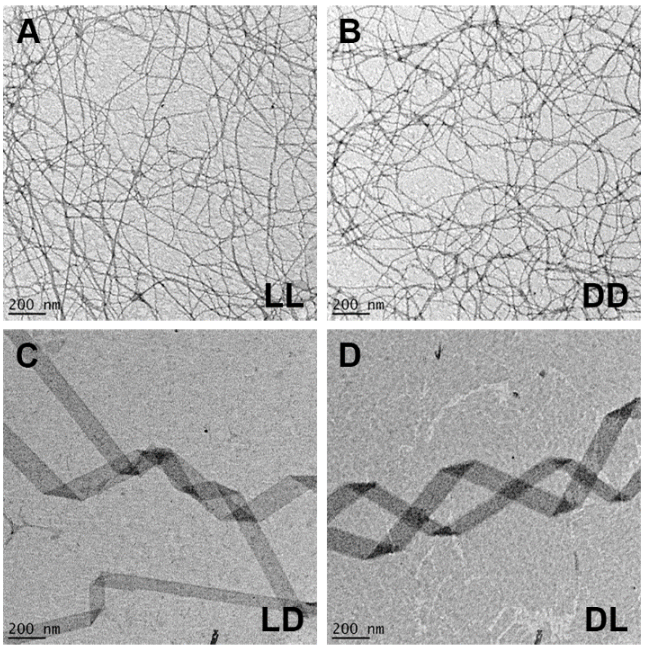

Figure 2.2. Negative-stain TEM images for (A) LL, (B) DD, (C) LD, and (D) DL KFE8 analogs at 0.25 mM in water.

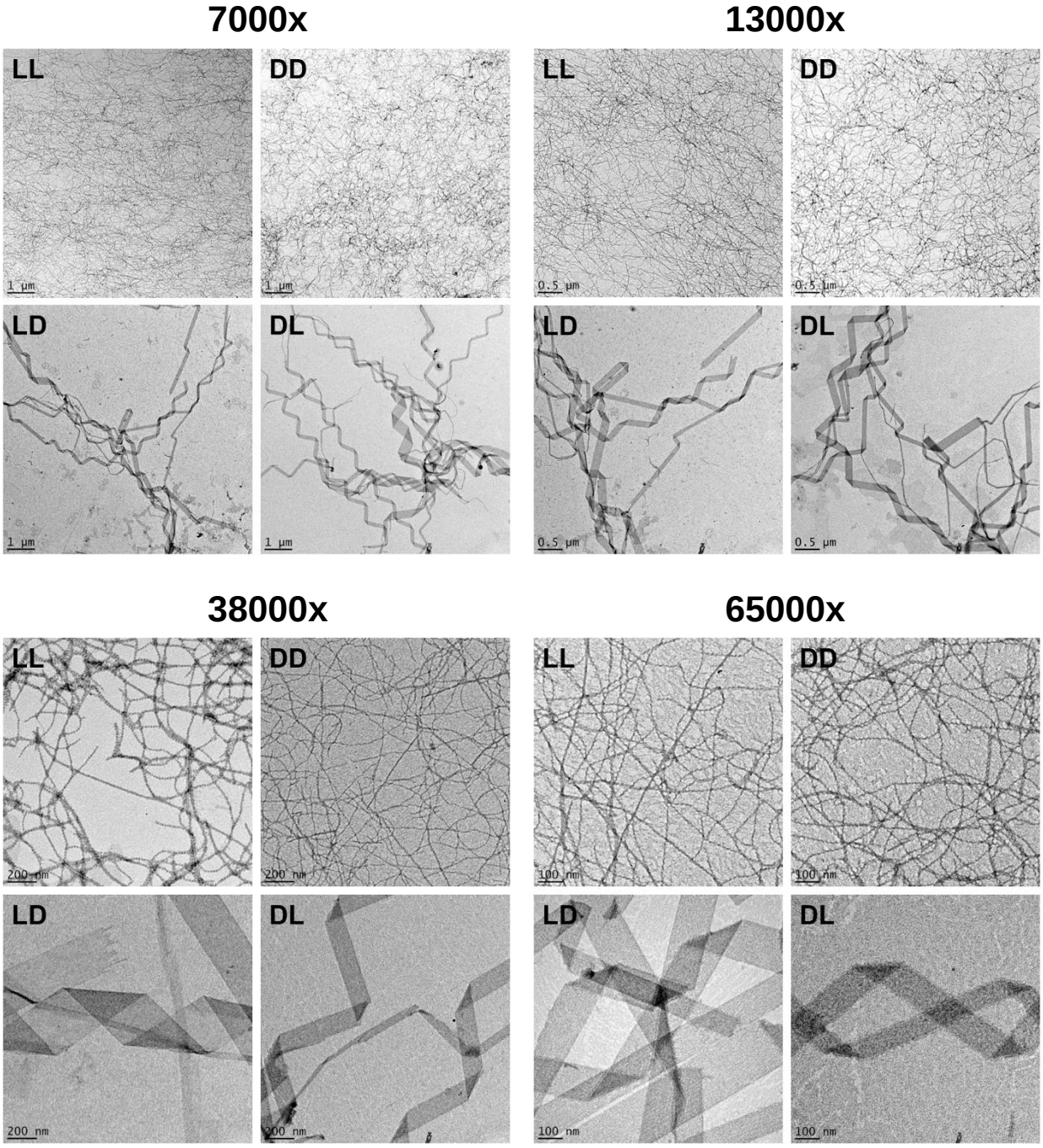

Figure 2.3. Representative TEM images of LL, DD, LD, and DL assemblies (0.25 mM in water) from 7000x to 65000x magnification.

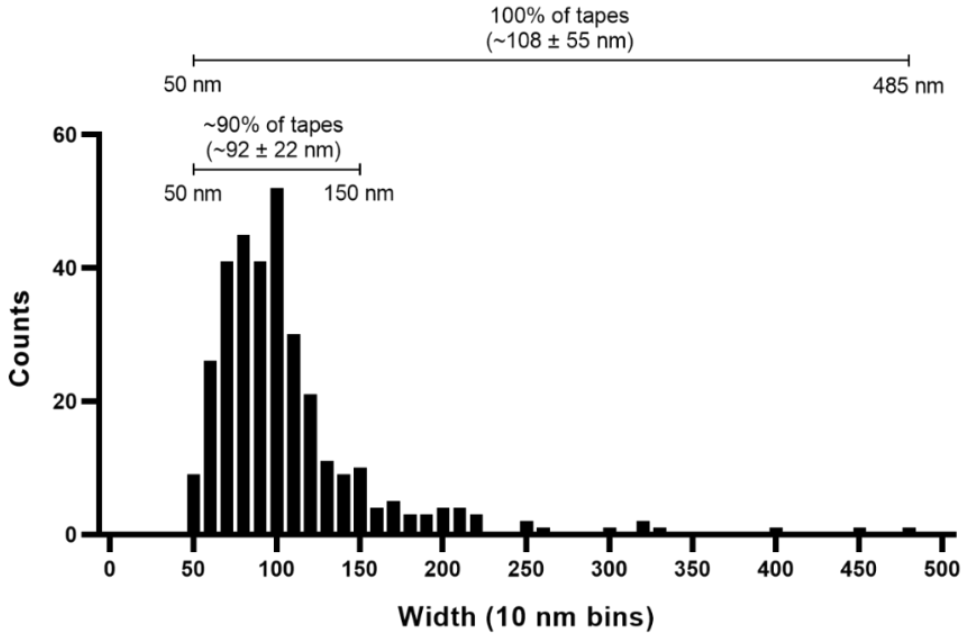

Figure 2.4. Histogram of LD and DL tape width measurements (n=331). Bin size is 5 nm. The distribution peaks at ~100 nm, and ~90% of measurements were between 50 and 150 nm (~92 ± 22 nm). The remaining ~10% of measurements, all greater than 150 nm, substantially impacted overall width statistics (~108 ± 55 nm) despite their relatively low prevalence.

2.5 Spectroscopic Analysis

Circular dichroism (CD) spectroscopy was used to determine the secondary structures of the analogs. The members of each enantiomeric pair produce mirror image spectra, with the chirality of the C-terminal blocks corresponding to their overall sign at wavelengths relevant to β-rich structures. Minima at ~204 nm and shoulders at ~214 nm confirm the expected cross-β structure of the homochiral peptide fibrils, while the LD and DL signatures are indicative of β-sheet and random coil morphologies (*Figure 2.5*). Second derivative FTIR spectra of all samples show major absorbances near 1630 cm^{-1} and 1695 cm^{-1}, verifying β-sheet secondary structure with antiparallel strand orientation (*Figure 2.6*).

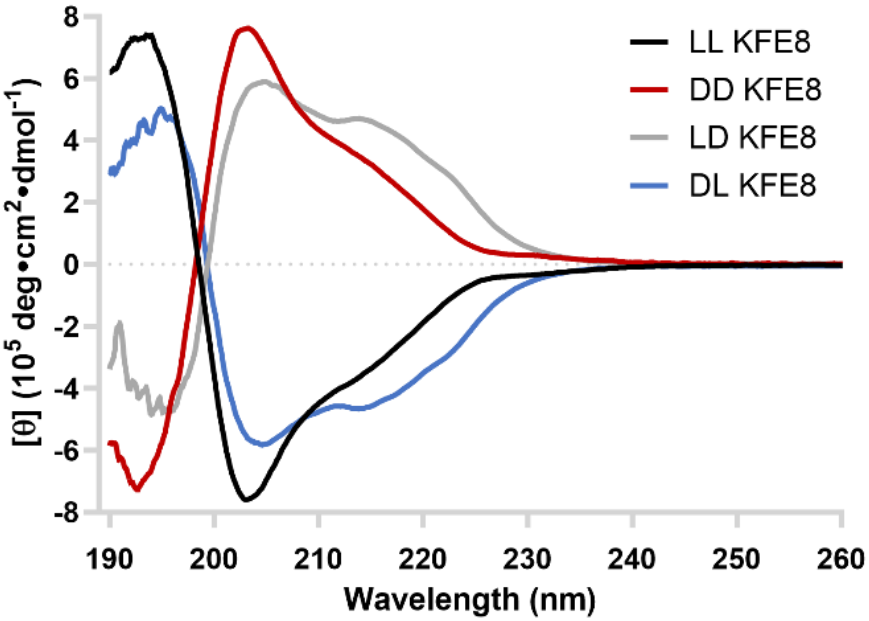

Figure 2.5. Circular dichroism (CD) spectra for the LL, DD, LD, and DL analogs of KFE8 in DI water (0.25 mM).

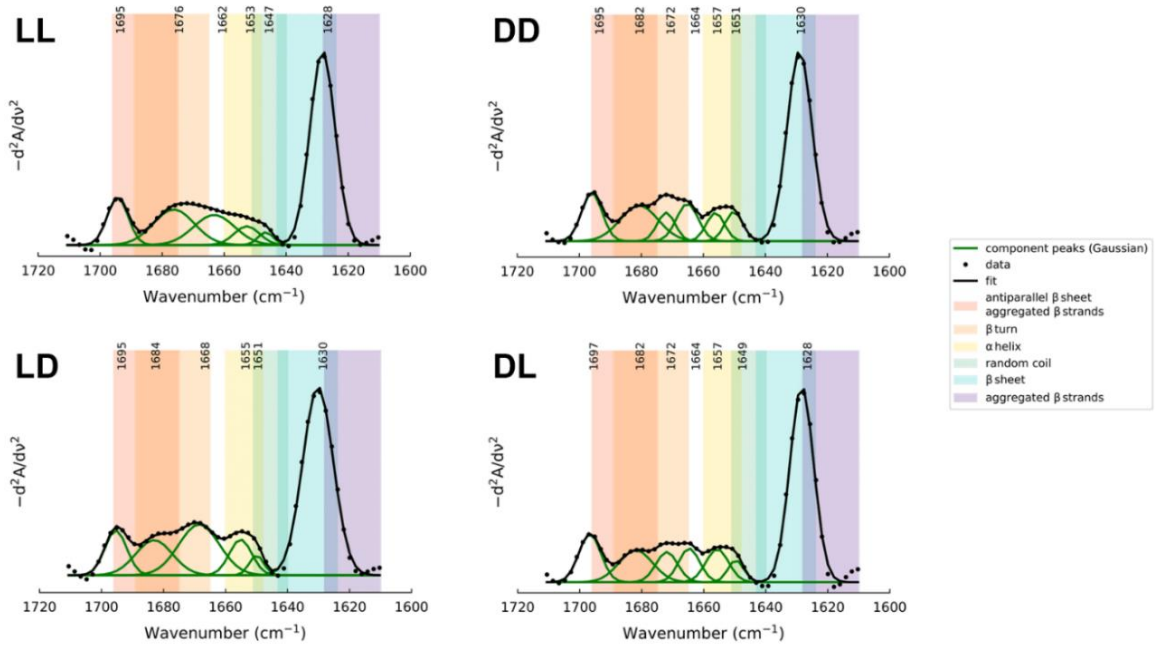

Figure 2.6. Second derivative FTIR spectra for the LL, DD, LD, and DL analogs of KFE8.

2.6 Geometric Modeling of Helical Tapes

Intrigued by how a small heterochiral peptide with monomer dimensions on the order of a few nanometers can assemble into comparatively enormous supramolecular helical structures, we modeled supramolecular helical tapes to estimate the bend and twist angles that would yield structures of the specified pitch and radius. Helical structures cannot form without both bend and twist. Twist in the absence of bend results in a non-helical twisted fiber. The absence of bend is the result of a lack of anisotropy between the faces of a fiber, most commonly achieved in fibers that are two β-strands thick (a 'ribbon'), such that the hydrophilic faces are exposed to solvent and hydrophobic faces are oriented toward the center of the fiber. Conversely, the presence of bend is typically the result of anisotropy between the faces of a fiber, and this is typically observed in fibers that are a single β-strand thick (a 'tape'), such that one face is more hydrophilic and the other is more hydrophobic.

Regularly spaced 'folds' of the tape-like assembly are consistently observed in TEM images of both the LD and DL peptides, serving as clear evidence of supramolecular helical structures (*Figure 2.2C,D*). As varying the identity of the charged residues produced flat tapes without regularly spaced folds (*Figure 2.18*), it appears that this feature is not attributable to the surface adsorption process. TEM image analysis reveals that the pitch of the helical tapes formed by LD and DL peptides is typically between ~900 and ~1200 nm (*Figures 2.2–2.4*). We note that because the TEM images represent surface-adsorbed material in vacuo, the measured helix dimensions should not be expected to precisely reflect helix dimensions in aqueous solution. However, the regularity and reproducibility of the helical dimensions suggest that the surface-adsorbed material provides a reasonable first approximation of the helical tape proportions.

We model the LD and DL helical tapes as being composed of stacked rectangular blocks, with each block having the dimensions of a peptide monomer in an extended or β-strand-like conformation. As described by Aggeli et al., the radius and helical pitch of a tape composed of stacked monomer units are dictated by the bend, or rotation about the axis of the β-strand backbone, and the twist, or rotation about the axis of the fiber, of the monomers composing the tape. The helical pitch (p) and radius (r) and are given by:

$$p = b_2 \left(\frac{2\pi}{\gamma_\theta}\right)\left(1 + \left(\frac{\gamma_\nu}{\gamma_\theta}\right)^2\right)^{-1} \qquad \text{(Equation 2.1)}$$

$$r = b_2 \left(\frac{\gamma_\nu}{\gamma_\theta{}^2}\right)\left(1 + \left(\frac{\gamma_\nu}{\gamma_\theta}\right)^2\right)^{-1} \qquad \text{(Equation 2.2)}$$

where γ_ν and γ_θ are bend and twist, respectively, and b_2 is the interstrand distance (Aggeli et al., 2006). Taking the interstrand distance determined from WAXS data (0.478 nm) and the helical pitch and radii determined by TEM imaging and dimension measurements, we use these equations to estimate the bend and twist angles that would yield helical structures of the specified pitch and radius.

Based on this modeling, assembly of heterochiral peptides into supramolecular helices with a pitch of ~1 μm and a radius of 100 nm is achieved when the bend (γ_ν) is 0.077° and the twist (γ_θ) is 0.124° (*Figure 2.7A*). The corresponding values for tape widths from 10 nm to 500 nm are shown in *Figure 2.8*. Alternatively, assembly of homochiral peptides into tighter helices with a pitch of 20 nm and a radius of 7 nm is achieved with increased bend and twist of 3.24° and 1.50°, respectively (*Figure 2.7B*).

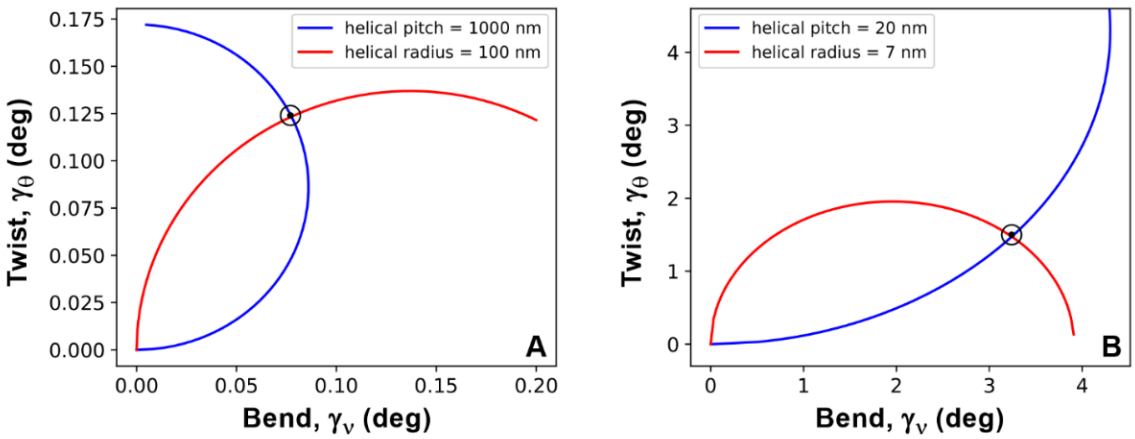

Figure 2.7. Representative bend and twist calculations. A helix with a given pitch and radius is the result of a unique combination of bend and twist. The combination of bend and twist angles that yield a helix of a specified pitch and radius are given by the intersection of a curve representing all combinations of bend and twist angles that yield a given helical pitch, and a second curve representing all combinations of bend and twist angles that yield a given helical radius. (A) The curve representing all combinations of bend and twist angles that yield a pitch of 1 μm (blue) that intersects (black dot) with the curve representing all combinations of bend and twist angles that yield a radius of 100 nm (red) at a single non-zero location (0.077°, 0.124°), giving the unique combination of bend and twist angles that yield a helix of the specified pitch and radius. (B) Same as in (A), except using a pitch of 20 nm (blue) and a radius of 7 nm (red), which intersect (black dot) to give bend and twist angles of 3.24° and 1.50°, respectively.

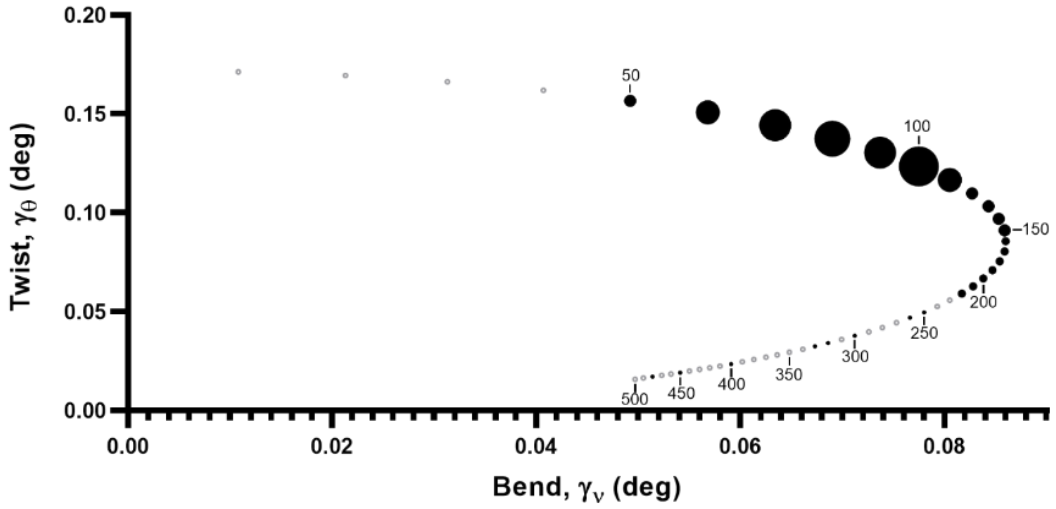

Figure 2.8. Bend and twist calculations for tapes with a pitch of 1 μm and radii ranging from 10 nm to 500 nm at 10-nm intervals, increasing clockwise. Point size represents prevalence of a given radius (10-nm-wide bins) as observed by TEM (*Figures 2.2*, *2.3*), with unfilled gray circles denoting empty bins.

2.7 Small- and Wide-Angle X-Ray Scattering

Small- and wide-angle X-ray scattering (SAXS and WAXS) confirm morphological differences between the homochiral and heterochiral peptides at both the molecular and supramolecular levels. The LL and DD peptides form fibrils ~9.8 Å thick, consistent with the reported β-sheet helical structure (Luo & Zhang, 2012). In contrast, the LD and DL peptides form tapes ~6.7 Å thick, corresponding to monolayer sheets. Low-q behaviors observed by SAXS indicate that the Gaussian chain distribution correlation length increases from ~100 Å for the homochiral peptides (LL and DD) to ~350 Å for the block heterochiral peptides (LD and DL), representing a larger gel mesh size (*Figure 2.9A, Table 2.1*) (Koshimizu et al., 2009). The SAXS curves transition from Gaussian chain-type scattering at low-q ($q<0.03$ Å^{-1}) to Debye-Bueche heterogeneous crosslink-type scattering at higher-q values ($q>0.05$ Å^{-1}), while Debye-Bueche heterogeneity factors drop from 35–40 Å for LL and DD to ~22 Å for LD and DL, both of which indicate a loss of associative interactions between fibrils.

Table 2.1. SAXS characteristics of the peptide filaments and gels.

Peptide	R_g (Å)	Filament R_{cs} (Å)	Thickness Plate R_t (Å)	Chain Length (Å)	Debye-Bueche (Å)
LL	97*	21.2(1)	9.8(1)	123(5)	35(1)
DD	97*	21.2(1)	9.7(2)	94(3)	40(2)
LD	115*	25.1(4)*	6.4(5)	355(47)	21.8(2)
DL	115*	23.8(3)*	6.8(2)	338(46)	22.3(2)

*Curves not linear. Table lists the Guinier radius of gyration (R_g), filament Guinier cross-sectional radius (R_{cs}), Guinier sheet thickness (R_T), Gaussian chain correlation length, and Debye-Bueche heterogeneity parameter for each peptide (*Figure 2.9A*).

WAXS curves show both similarities and differences between the homochiral and block heterochiral analogs (*Figure 2.9B, Table 2.2*). The strongest common peak appears at 4.74–4.78 Å ($q=1.32$ Å^{-1}) and represents β-sheet spacing. The LD and DL peptides have unique peaks at 5.4

Å and 9.6 Å, the first of which consists of a close doublet at 5.5 and 5.3 Å that matches the 5.4 Å (q=1.14 $Å^{-1}$) reflection observed in $Aβ_{42}$ amyloid films. The second, seen as a kink in the slope of the curves at 9.6 Å, roughly corresponds to β-solenoid spacing typically observed at ~9.4 Å (q=0.66 $Å^{-1}$) (Toyama & Weissman, 2011). A simple anti-parallel model (*Figures 2.10, 2.11*) of the heterochiral peptide forms monolayer β-sheets with a characteristic 9.5 Å repeat that approximately matches that of a β-solenoid (*Figure 2.11*) (Castelletto et al., 2017).

Table 2.2. d-spacing of WAXS peaks.

Peptide	Peak-1 (Å)	Peak-2 (Å)	Peak-3 (Å)	Peak-4 (Å)	Peak-5 (Å)	Peak-6 (Å)	Peak-7 (Å)
LL	--	--	5.00	4.77	--	3.33	2.16
DD	--	--	5.02	4.78	--	3.35	2.14
LD	9.6	5.4	--	4.74	4.64	3.63	2.14
DL	9.6	5.4	--	4.74	4.62	3.60	2.20

Table shows the d-values (d=2π/q) for the major peaks of the WAXS scattering curves shown in *Figure 2.9B*.

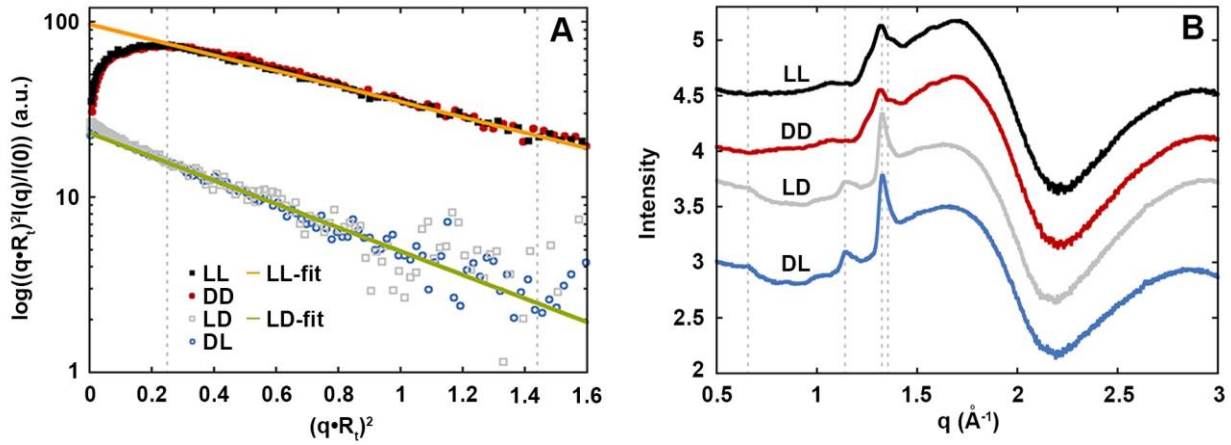

Figure 2.9. SAXS and WAXS data for the homochiral and block heterochiral peptides. (A) Kratky-Porod SAXS plots and Guinier radius of gyration of thickness fits to LL and DD data (R_t=9.8 Å) and LD and DL data (R_t=6.7 Å). Guinier fits used data in the range $(q•R_t)^2$ = 0.25 to 1.44, as marked by the vertical dashed lines. (B) WAXS curves. The dashed lines mark the published 9.4 Å β-solenoid (q=6.6 nm^{-1}), 5.4 Å $Aβ_{42}$ amyloid (q=11.4 nm^{-1}), 4.76 Å β-sheet (q=13.2 nm^{-1}), and 4.64 Å β-mismatch (q=13.5 nm^{-1}) peaks.

2.8 Molecular Dynamics Modeling

The proposed LD model maintains the typical anti-parallel H-bond network. The model's amino acid backbone is unchanged while the D-residues' R-groups were relocated by a rotation of 120° about the peptide backbone axis (*Figure 2.10A*). This positions the D-Phe phenyl rings below the β-sheet and produces a kink at the Glu4-(D-Phe)5 L-D interface. This also introduces an internal stain that counters and partially flattens the natural twist of the β-sheet, resulting in a much longer helical pitch than seen in homochiral KFE8 fibrils. The alternating hydrophobic and hydrophilic side chains no longer laminate to form a bilayer and the heterochiral filament is instead a monolayer (*Figure 2.11*). Thus, our SAXS data and energy-minimization modeling outcomes both confirm the likelihood of a monolayer, suggesting that the LD supramolecular structures are likely tapes with a fundamentally different packing mode than homochiral LL ribbons.

The imperceptibly small 0.13° twist per β-strand calculated from our geometric model is likely not H-bond induced, as in the homochiral peptides, but rather due to interactions between their terminal-capping acetyl and amide groups. The basic unit of the filament is an LD dimer, which has D2 symmetry perpendicular to the sheet and filament axes. The non-identical upper and lower surfaces each have four Phe, two Glu, and two Lys stacks interspersed (*Figure 2.11*). The lower surface in this representation has a central Phe-stacked ridge, while the upper surface has a Lys-filled groove. However, neither surface is predominantly hydrophobic, preventing the heterochiral filament from forming the laminated bilayers seen in homochiral KFE8. It is possible that the wide sheets seen in TEM are the result of filament edge interactions, as illustrated in *Figure 2.12*.

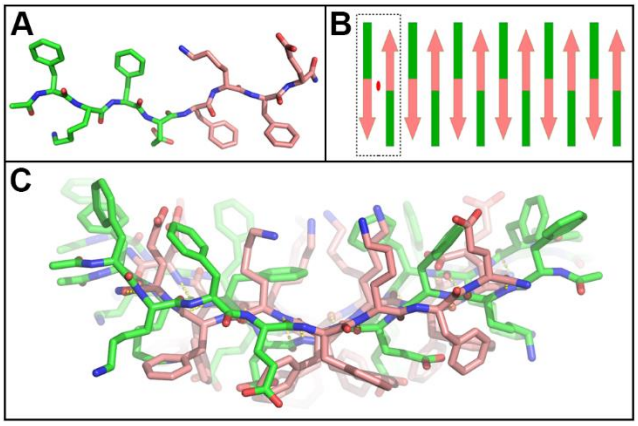

Figure 2.10. MD modeling reveals that the energy-minimized LD fibril structure consists of peptides with a ~160° rotation about the 'L-D' (E4-f5) plane. (B) Peptides in the proposed structure assemble to form a fibril with a repeating unit (dashed box) that possesses internal 2-fold symmetry (red ellipse) between two antiparallel units. (C) The energy-minimized protofilament model is a monolayer whose non-identical faces include a Phe-stacked ridge (lower, middle) and a Lys-filled groove (upper, middle).

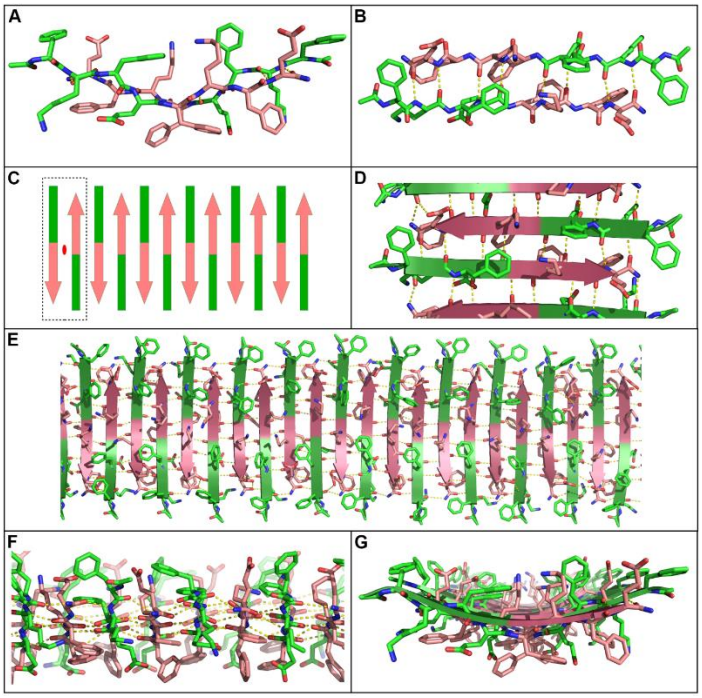

Figure 2.11. Visual representations of the energy-minimized LD KFE8 peptide model (L-block: green, D-block: pink). The LD peptide forms an untwisted β-sheet with ~34-Å-diameter curvature. (A) The two β-strands that form the basis of the LD antiparallel β-sheet filament. (B) Top-down view showing the antiparallel β-sheet hydrogen bonding pattern. (C) Schematic of the anti-parallel β-sheet formed by the DL peptide. The repeating unit (dashed box) possesses internal 2-fold symmetry (red ellipse) between two antiparallel units. (D) Close-up view of the filament. (E) Top-down view of the antiparallel β-sheet filament. (F) Edge-on view of the acetylated N-terminal L-Phe and amidated C-terminal D-Glu. (G) End-on view of the filament.

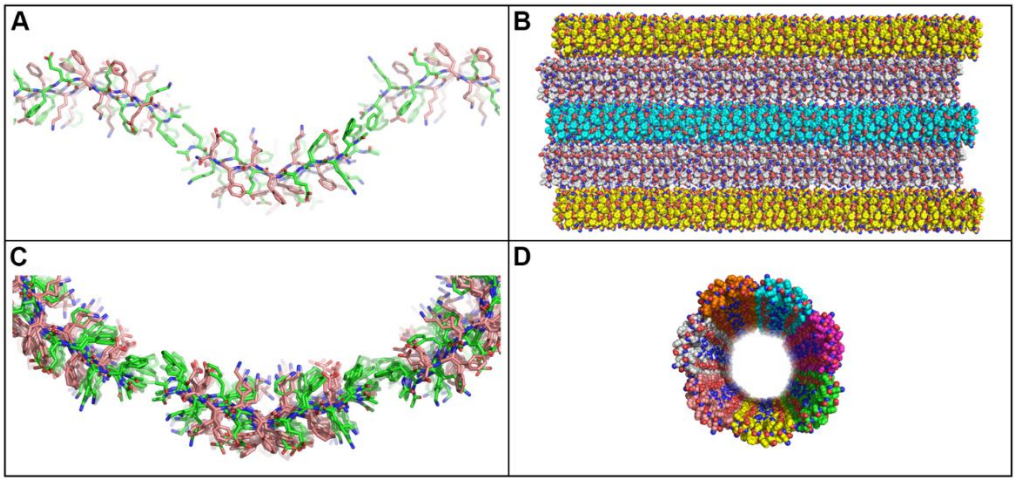

Figure 2.12. Possible edge interactions of the LD KFE8 β-sheet filaments. The LD peptide model β-sheet filament exposes the N-terminal acetylation and L-Phe. These could interact to form two possible larger order assemblies: a wide undulating sheet (A,B) or a tubular assembly with ~80+ Å diameter (C,D), though only the former is observed. The sheet model assumes interactions between the edges of the β-sheet filaments in an alternating up/down pattern.

2.9 Rheology

As supramolecular peptide assemblies are used as scaffolds for *in vitro* cell culture and *in vivo* tissue regeneration, we sought to compare the rheological properties of the homochiral and block heterochiral analogs. The steady flow curves for all peptide gels show decreasing viscosity with increasing shear rate, demonstrating shear-thinning behavior (*Figure 2.13A*). This can be quantitatively compared by fitting the viscosity versus shear rate curves to a power law model (*Table 2.3*) (Chauhan et al., 2018). Higher flow consistency indices for the LL and DD gels confirm their stability and strong interfibrillar associations relative to LD and DL. All gels exhibit excellent shear-thinning properties, with power law indices of -0.15 and -0.13 (negative values likely indicate sample slip) for LL and DD, respectively, and 0.03 for both LD and DL (Fraiha et al., 2011). The block heterochiral peptide gels possess approximately three-fold lower storage moduli at all shear rates (*Figure 2.13A, inset*). In contrast, all gels maintain their stability and exhibit consistent mechanical recovery after being subjected to multiple low- or high-strain cycles (*Figure*

2.13B). This is a desirable property for hydrogels intended for biomedical applications, as viscosity is reduced under the shear stress of injection before recovering *in situ* (Guvendiren et al., 2012).

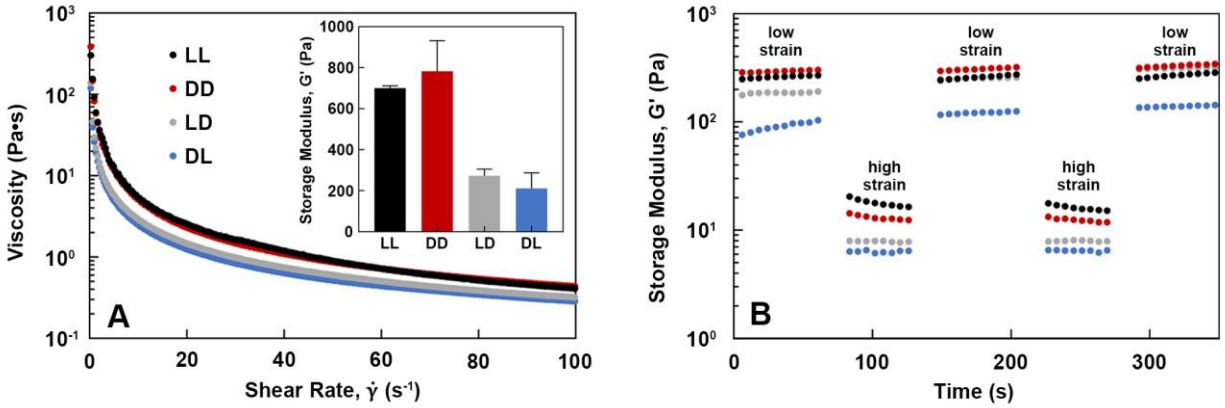

Figure 2.13. Rheological studies of peptide hydrogels (10 mM in water). (A) Shear-thinning behavior and storage moduli (inset). (B) Mechanical recovery following cyclic strain to failure.

Table 2.3. Shear-thinning power-law fit parameters.

Peptide	K	N
LL	80.0	-0.15
DD	73.9	-0.13
LD	28.2	0.03
DL	23.4	0.03

Table shows the flow consistency index (K, viscosity at shear rate 1 s^{-1}) and power-law index (n) given by the equation $\eta = K\dot{\gamma}^{(n-1)}$, where η is viscosity and $\dot{\gamma}$ is shear rate (Chauhan et al., 2018; Ginzburg et al., 2018; Truby & Lewis, 2016). Higher K values for the LL and DD gels confirm their stability and strong interfibrillar associations relative to the LD and DL gels. The power law index (n) is a direct measure of shear-thinning behavior, with n=1 indicating that a material is Newtonian, n>1 indicating shear-thickening behavior, and n<1 indicating shear-thinning behavior.

2.10 Polar Amino Acid-Substituted Variants

The generality of this phenomenon was examined using LL and LD analogs of RFE8 (FRFEFRFE) and RFD8 (FRFDFRFD). LL and LD KFERFD8 (FKFEFRFD) were also synthesized to determine whether enantiomeric blocks are explicitly required. In the homochiral variants, fibril morphology

(*Figure 2.14*) and secondary structure (*Figure 2.15*) appeared to be unaffected by the substitution of lysine (K) with arginine (R) in RFE8. In contrast, additionally substituting glutamic acid (E) with aspartic acid (D) in RFD8 greatly impacted hierarchical assembly, as evidenced by a large population of fibrils with lower aspect ratios and loss of the characteristic CD signature of KFE8.

The morphology of LL KFERFD8 fibrils was found to be similar to LL KFE8 and produced an identically shaped, lower-magnitude CD spectrum, indicating that the presence of the FRFD block partially impedes assembly but that the homochiral peptides with non-enantiomeric blocks remain capable of fibrillization. However, the length of LL KFERFD8 fibrils is variable but consistently an order of magnitude shorter (583 ± 291 nm) than the multiple-microns-long fibrils of LL KFE8. As controlling the aspect ratio of epitope-bearing fibrillar scaffolds is a major goal for peptide-based immunomodulation, controlling this property through the ratio of KFE8-to-KFERFD8 monomers has considerable potential value. A recent paper achieved such control over the self-assembling cross-β peptide Q11 using a second population of 'capping' peptides (Fries et al., 2020). As such, attaining similar or improved results using only a single peptide is a promising avenue for continued investigation, along with the possibility of further influencing length through ratiometric combination with LL KFE8.

All LD variants form tapes resembling those of KFE8. Varying charged residue identities (LD RFE8 and RFD8) results in flat tapes without regularly spaced folds, suggesting that the observed helicity of KFE8 is not merely a surface adsorption artifact. Interestingly, LD KFERFD8 regains the helicity and apparent structural integrity of LD KFE8. Despite these morphological similarities, CD data indicated divergent secondary structure between the LD variants, in particular the curiously inverted CD sign of RFD8 and KFERFD8, and complementary spectroscopic analyses may provide additional insight into the molecular-level effects of these substitutions.

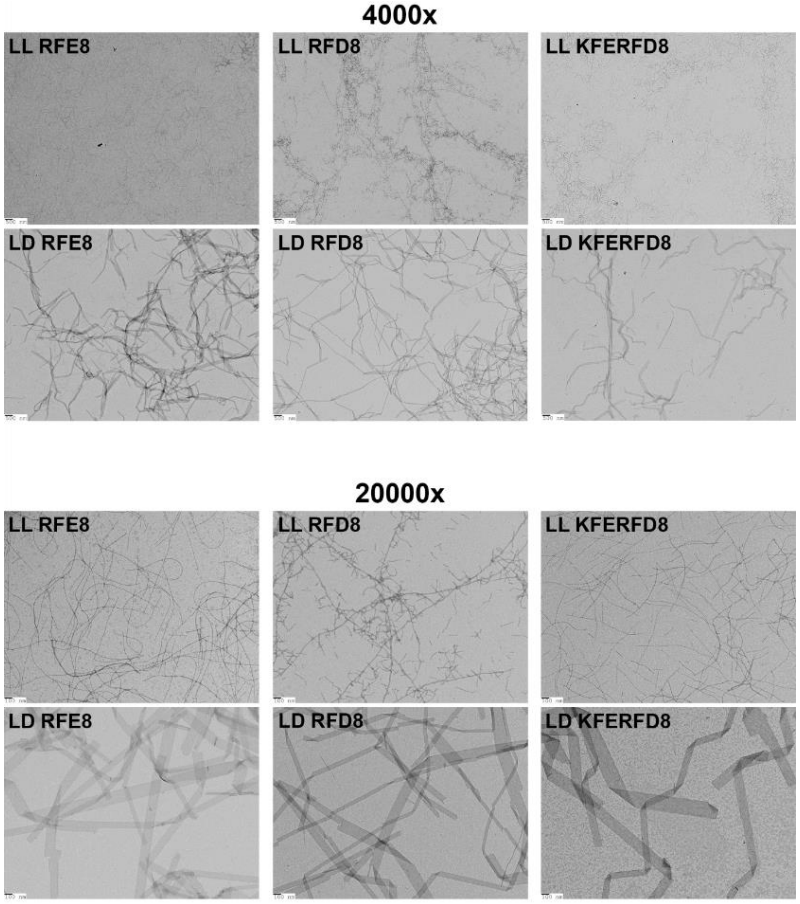

Figure 2.14. Representative TEM images of LL and LD RFE8 (left column), RFD8 (center column), and KFERFD8 (right column) peptide assemblies at 0.25 mM in DI water. Shown at 4000x (top) and 20000x (bottom) magnification.

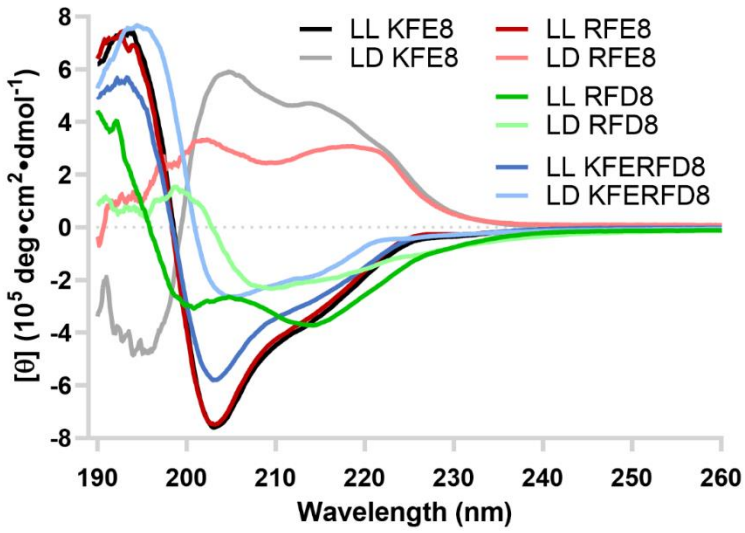

Figure 2.15. CD spectroscopy data (0.25 mM) for the LL and LD analogs of KFE8 (FKFEFKFE), the charged residue-substituted variants RFE8 (FRFEFRFE) and RFD8 (FRFDFRFD), and the non-enantiomeric blocked KFERFD8 (FKFEFRFD).

2.11 Conclusions

In this chapter, we present block heterochirality as a complementary strategy for the design of self-assembling peptides with alternating polar and nonpolar residues. While the use of chirality in peptide-based biomaterials has centered primarily around controlling *in vivo* degradation, there is an emerging interest in its utility as a means to alter assembly mechanics and modulate bulk material properties. The Nilsson and Schneider groups have used racemic mixtures of the peptides KFE8 and MAX1 to demonstrate the role of stereocomplexation, or energetic favorability of interactions between enantiomers, in rippled β-sheet formation and subsequent enhancement of hydrogel rigidity (Nagy et al., 2011; Swanekamp et al., 2012). This work finds that incorporating both L- and D-chiral repeat motifs into a single peptide facilitates unique intermolecular interactions that direct the assembly of novel fibril morphologies. Based on a proposed assembly model that agrees with experimental data, rotation at the L-D interface allows H-bond networks to be maintained and both hydrophobic (Phe) and charged (Lys, Glu) groups to be presented on each face of a β-sheet monolayer. One can envision extending this design pattern to amphipathic peptides of various lengths and amino acid compositions to develop materials with unique morphological, physicochemical, and biological properties.

Chapter 3: Modulating Peptide Self-Assembly via Triblock Chiral Patterning

Partially adapted from: Conor L. O'Neill, Jonathan L. Fascetti, Zoe Clapacs, Lauren K. Kaplita, Chih-Yun Liu, Darren Kim, Mark A. White, and Jai S. Rudra (2023). Modulating Peptide Self-Assembly via Triblock Chiral Patterning. Under review at the Journal of the American Chemical Society.

3.1 Abstract

The suprastructural integrity of peptide self-assemblies is driven by an intricate array of cohesive interactions that guide and maintain hierarchical order. Seemingly minor alterations to atomic arrangement, such as substitution with D-amino acids, can dramatically affect assembly potential and resultant architecture. When a primary sequence is comprised of consecutive identical motifs, 'block heterochiral' peptides can be generated by partitioning chiral inversions according to these underlying elementary units. In this work, we present a combinatorial exploration of all triblock chiral patterns for the model β-sheet-forming peptide KFE12 (Ac-(FKFE)$_3$-NH$_2$). Analysis of the four resulting enantiomer pairs reveals that each produces a unique morphology, ranging from minimal 4-nm-wide twisted ribbons to micron-scale semi-structured aggregates. Our investigation of these variants illustrates a combination of conserved and divergent hierarchical features, reflecting complex interplay between persistent fundamental forces and the unique spatial implications of blockwise intramolecular chiral interfaces.

3.2 Introduction

For the purposes of structural exploration, the intrinsic modularity of self-assembling peptides facilitates and greatly simplifies intentional design and iterative variation (Huo et al., 2023; Lau et al., 2020). This tractability enables researchers to refine and amplify particularly influential domains from natural proteins. This is exemplified by a yeast-derived β-sheet-bilayer ('cross-β') peptide with alternating polar and nonpolar residues (S. Zhang, 2020). When phenylalanine is selected as the nonpolar component, aromatic π-stacking within the hydrophobic core improves fibril cohesion; similarly, solubility and electrostatic interactions can be enhanced by selecting a charge-complementary pair of solvent-exposed residues (Marini et al., 2002). These alterations produce virtually optimized cross-β peptides such as those of the KFE family, Ac-$(FKFE)_n$-NH_2 (Bowerman & Nilsson, 2012).

The collective strength of these integral forces permits substantial primary sequence modification without precluding self-assembly, affording the production of expansive variant arrays (S. Yang et al., 2023). While amino acid composition and patterning are inherently ubiquitous in the field of peptide self-assembly, *de novo* design has largely been confined to the use of L-amino acids (Melchionna et al., 2016). In recent years, several research groups have begun utilizing 'non-natural' D-amino acids in self-assembling peptide sequences (Zheng et al., 2021). Full substitution predictably yields mirror-image structures; however, partial substitution has proven to be a diversely potent supplement to traditional means of modification (Marchesan et al., 2014; Schneider et al., 2002; Taraban et al., 2012). Inclusion of both L- and D-residues produces unique spatial arrangements and side-chain interactions due to the internal strain imposed on the peptide backbone by atypical H-bond networks and steric interactions. In tandem with conventional design elements, this powerful strategy redefines the limits of biomolecular customization.

The dramatic influence of partial D-substitution on secondary structure, morphology, gel mechanics, and bioactivity has been demonstrated for numerous peptide classes (Marchesan, Waddington, et al., 2012; Schneider et al., 2002; Xie et al., 2022). Further, racemic mixtures of all-L and all-D self-assembling isomers stereocomplex into a singular coassembled architecture (Guo et al., 2021; Nagy-Smith et al., 2017; Swanekamp et al., 2012). At the intersection of these two concepts, 'block heterochirality' exploits repetitive sequences (e.g., $(FKFE)_n$) to produce mixed-chiral species that preserve the stereoselective potential of each individual block. We previously reported on the striking structural departure of the diblock heterochiral KFE8 analogs LD (FKFEfkfe) and DL (fkfeFKFE) from their homochiral counterparts, LL and DD (Clover et al., 2020). As opposed to bilayers, LD and DL form monolayers with width and helical pitch an order of magnitude larger than those of the narrow, tightly wound LL and DD cross-β fibrils.

Motivated by these results, the current work aims to expand the scope of block chirality to KFE12, Ac-$(FKFE)_3$-NH_2. As triblock systems, the eight KFE12 analogs reported in this study (*Figure 3.1*) introduce a third variably chiral domain whose non-terminal position isolates its impact from edge-interactions with laterally associated β-sheets.

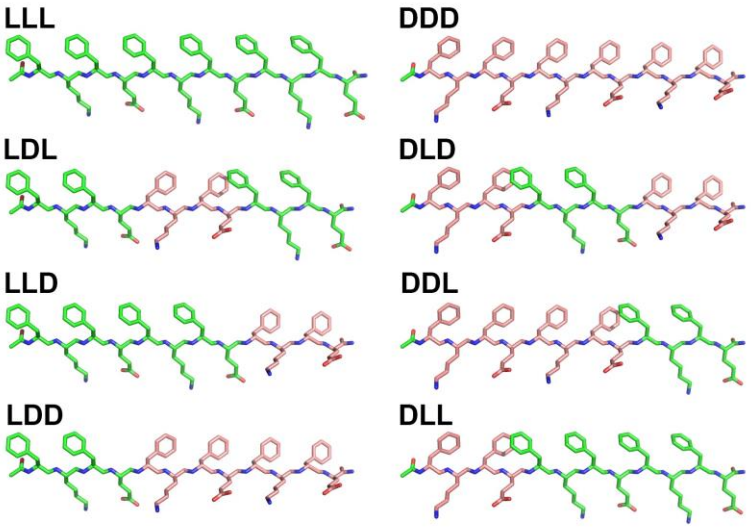

Figure 3.1. Structures of the triblock chiral KFE12 isomers. Carbons shown in green for L- and in pink for D-residues.

3.3 Methods

Peptide Synthesis. Peptides were purchased from P3 BioSystems (Louisville, KY) for molecular and spectroscopy studies. Peptides for rheological analysis were synthesized using Fmoc chemistry on a CEM Liberty Blue automated synthesizer. After swelling Novabiochem (Burlington, MA) rink amide MBHA (4-methylbenzhydrylamine) resin for one hour, double coupling of residues was performed using Oxyma (ethyl cyano(hydroxyimino)acetate) and DIC (*N*,*N*'-diisopropylcarbodiimide). Peptide cleavage was achieved in a cocktail (95:2.5:2.5) of TFA (trifluoroacetic acid), TIS (triisopropylsilane), and water. Crude products were pelleted via centrifugation, washed in cold diethyl ether, freeze-dried, and stored as powders at -20°C.

Peptide Purification and Identification. Crude peptide was dissolved in 1:1 acetonitrile (ACN):TFA and injected onto an Agilent (Santa Clara, CA) semi-preparative UltiMate 3000 high-performance liquid chromatography (HPLC) system employing a reverse-phase Zorbax column (SB-C18, 21.2 x 150 mm, 5 μm). A gradient of ACN/water (0.1% TFA) was flowed at 18 mL/min, with UV absorbance monitored at 214 and 254 nm. After fraction collection and freeze-drying, purity confirmation was obtained on an analytical UltiMate 3000 system employing a reverse-phase Poroshell 120 column (SB-C18, 4.6 x 150 mm, 2.7 μm), followed by matrix-assisted laser desorption/ionization-time-of-flight mass spectrometry (MALDI-TOF-MS) using a α-cyano-4-hydroxycinnamic acid matrix from Bruker (Billerica, MA) to confirm final purified product identity.

Peptide Self-Assembly. Purified peptide products were massed on a Sartorius (Göttingen, Germany) Quintex 65-1S semi-micro analytical balance. Stocks were solubilized at 0.10 mM in a solution of 1:1 ACN/water, separated into aliquots, lyophilized for 48 hours, and stored as powders

at -20°C. Non-gelated experimental samples (STEM, CD, FTIR) were solubilized at 0.10 mM in water and gently pulsed on a Fisherbrand (Hampton, NH) Fixed-Speed Vortex Mixer.

Scanning Transmission Electron Microscopy (STEM). KFE12 peptide solutions (0.10 mM in water) were negative stained with 7.5% uranyl formate (UF). To prepare staining solutions, 37.5 mg UF was added to 5 mL boiled and cooled MilliQ water, vortexed for five minutes, pH-balanced with 2 M NaOH (20 µL), vortexed for an additional five minutes, filtered through a 4-mm PTFE syringe filter (0.2 µm), and aliquoted into individual 0.5 mL conical tubes. UF aliquots were flash-frozen and stored at -80°C. Before use, UF aliquots were fully thawed and placed in an Eppendorf (Hamburg, Germany) 5417C Centrifuge at 25,000 RCF for five minutes, followed by re-filtering the supernatant and storing under foil at room temperature. Ted Pella (Redding, CA) 200-mesh, pure-carbon-coated grids were glow discharged, inverted onto a 10-µL sample droplet for 60 seconds, briefly washed in three consecutive 10-µL MilliQ water wash droplets, then stained for 60 seconds in a 10-µL 7.5% UF droplet. Grids were desiccated for 60 seconds and allowed to air-dry for 15 minutes before storage in a foil-covered grid box. Micrographs were acquired on a JEOL (Akishima, Japan) JEM-2100F Field-Emission STEM using Gatan 805 bright-field/dark-field (BF/DF) and Gatan high-angle annular dark-field (HAADF) detectors with an accelerating voltage of 200 keV, spot size of 0.5 nm, and camera length of 10 cm.

Width and Pitch Measurements. A Fiji image processing package was utilized for STEM image analysis and assembly dimension measurements. Length scales were assigned using JEOL software-generated scale bars. Width measurements ($n \geq 150$) were obtained from high-magnification micrographs, on which line segments perpendicular to peptide suprastructure edges were superimposed and measured. The pitch of twisted ribbons, when observed, was quantified in an analogous manner, with segments drawn between the alternating 180° twists at the point of

minimal width. Pitch measurements were supplemented by TEM micrographs acquired on a JEOL (Akishima, Japan) JEM-1400 transmission electron microscope with an accelerating voltage of 120 kV.

Circular Dichroism (CD). CD spectra of 0.10 mM KFE12 isomer solutions were acquired using a Jasco (Hachioji-shi, Japan) J-815 CD spectrometer. Samples were loaded into a Hellma (Plainview, NY) reduced-volume quartz cuvette (110-1-40) with a path length of 1 mm. Three accumulations for each sample were obtained between 300 and 190 nm at 50 nm/min with 0.1 nm data pitch, 1.00 nm bandwidth, and 100 mdeg sensitivity. High-tension voltage (HT[V]) and absorbance were also collected to ensure data quality.

Fourier-Transform Infrared Spectroscopy. Attenuated total reflectance-Fourier transform infrared (ATR-FTIR) spectra were measured with a Bruker (Billerica, MA) Alpha II FTIR outfitted with a zinc selenide crystal. For each analog, lyophilized peptide was gelated and subsequently diluted to 15 mM in ultrapure DI water. Standardized background and solvent spectra were acquired prior to collecting each absorbance spectrum. Spectra were generated from 264 readings (4 cm^{-1} step). Data processing was performed in GRAMS/AI software from Thermo Scientific (Waltham, MA). After background subtraction, a Savitzky-Golay filter (third order, nine-point window) was used to calculate second-derivative spectra. The resulting trace was inverted and truncated to 1710–1610 cm^{-1}. Baseline correction was performed assuming flat baseline segments between minima. Component peak identification and fitting in the 1710–1640 cm^{-1} domain was performed using Gaussian curves with a full width at half maximum (FWHM) height of eight cm^{-1} and medium sensitivity level, as informed by Akaike Information Criterion (AIC). The peaks of the fitted curves were then compared to published secondary structure ranges (Barth, 2007; Dong et al., 1990; Jackson & Mantsch, 1995).

Small- & Wide-Angle X-ray Scattering (SAXS & WAXS). SAXS data of the KFE12 solutions were collected using a Rigaku (Woodlands, TX) BioSAXS-1000 camera on an FRE^{++} X-ray generator with an ASC-96 Automated Sample Changer held at 10°C. A matching buffer was collected for each sample. The detector was calibrated using a silver behenate powder sample, following the manufacturer's recommended procedure. The KFE12 SAXS samples were prepared by dissolving the lyophilized powders in double-distilled water. LLL was prepared at 1.6 mM; DDD and LLD at 3.3 mM; and LDL, DLD, DDL, LDD, and DLL at 5.0 mM. Samples were centrifuged and vortexed to ensure proper mixing and to resuspend larger particles. Although the samples formed gels, these remained fluid under hydrostatic pressure, permitting pipetting. The samples did not display concentration dependence, and analysis used the highest-concentration SAXS data collected. Processing was performed in SAXSLab (Rigaku) and SAXNS-ES (https://xray.utmb.edu/SAXNS). All analyses were performed in Primus/GNOM (Manalastas-Cantos et al., 2021), BIFT (Hansen, 2000; Larsen & Pedersen, 2021), and gnuplot (http://www.gnuplot.info). Comparisons of the Molecular Dynamics-based filament models with the SAXS data were performed using Crysol (Svergun et al., 1995) and EOM (Tria et al., 2015).

WAXS data were collected at room temperature using 10-mM KFE12 solutions and matching buffers. Solutions were pipetted into a 2-mm MiTeGen (Ithaca, NY) MicroRT polyester capillary on a Rigaku R-AXISIV^{++} and processed using Fit2D, SAXNS-ES, and Primus. WAXS was performed with a nominal detector distance of 150 mm and 250 mm. The sample-to-detector distances were calibrated using a MicroRT capillary filled with powdered sucrose. Sucrose cell dimensions were determined using a Bruker D8/TXS diffractometer with a Cu X-ray source. Diffraction data were collected to d=0.84 Å from a single crystal of sucrose (0.2 x 0.2 x 0.2 mm) with the same X-ray source and the structure was solved using ShelXT, giving dimensions of

a=7.943(3) Å, b=8.718(4) Å, c=10.861(4) Å, β=103.05(1)°. These cell dimensions are within the range observed in previous publications (An et al., 2017; Beevers et al., 1952; Brown & Levy, 1963, 1973). WAXS curve fitting was performed in Primus and gnuplot, and WAXS local background subtraction used second-degree polynomials. Peak fitting used a common Gaussian peak width with geometric correction. Theoretical WAXS curves were generated from models using FoXS (Schneidman-Duhovny et al., 2010) and WAXSiS (Knight & Hub, 2015).

Molecular Dynamics Modeling. KFE12 filament models were created using COOT and PyMOL and were based upon a published KFE8 model (Hwang et al., 2003). Standard antiparallel β-sheet stereochemistry for the KFE12 peptide was imposed in COOT, along with standard interstrand hydrogen bonding for both sheets. A flat, 12-strand-long, 2-start sheet was created by translation of the COOT model. The PSF and PDB files for NAMD were created using the VMD (Humphrey et al., 1996) psfgen, solvate, and autoionize plugins. Each model was then minimized and annealed in NAMD (Phillips et al., 2020) before performing a 10-ns molecular dynamics simulation with implicit solvent and 2-fs time steps. These initial models were extended to 44-chain filaments and then fully solvated in 150 mM NaCl. These extended models were energy minimized and annealed prior to 10-ns molecular dynamics runs performed with the CHARMM36 forcefield and the TIP3P water model. Analysis of the NAMD simulations was performed using the VMD interface and TCL scripts, including the NAMDEnergy plugin. For SAXS/WAXS analysis, the filament models were extended in PyMOL to create multi-turn filaments of increasing length up to 400 nm. This procedure was followed for the two possible interstrand hydrogen bonding patterns, with either acetylated N-termini or amidated C-termini more solvent-exposed.

Rheology. For rheological testing, hydrogels were formed by dissolving each KFE12 analog at 10 mM in DI water. The sample was then extruded through a needle onto a TA Instruments (New

Castle, DE) Discovery HR-20 rheometer fitted with a 20-mm-diameter flat geometry, which was then lowered to a gap height of 500 μm. Each gel was centered and sheared to failure by rotation at 1 radian/second for a minimum of 10 seconds. The rotation was then stopped and the test sequence was initiated, consisting of a 5-minute time sweep with a frequency of 0.1 Hz and an oscillatory strain of 1%. The gel was then rested for 30 seconds before a frequency sweep ranging from 100 to 0.1 Hz with oscillatory strain held constant at 1%. After conclusion of the frequency sweep, a strain sweep was performed with oscillatory strain ranging from 0.1% to 100% and frequency held constant at 0.1 Hz. This process was repeated three times for each gel formulation, with each repeat corresponding to an independently prepared gel. During rheological testing, the storage modulus (G′) and loss modulus (G″) were recorded, as well as the phase angle (δ) and raw phase (°) as indicators of data quality. Complex viscosity was computed from storage and loss moduli and frequency.

3.4 Scanning Transmission Electron Microscopy

As observed by electron microscopy, the eight triblock chiral analogs adopt four remarkably distinct morphologies (*Figure 3.2*), with each pair producing visually indistinguishable suprastructures aside from twist handedness, if present (*Figures 3.2–3.5*). The homochiral analogs, LLL and DDD, adopt minimal cross-β fibrillar structures just one peptide in width (4.4 ± 0.4 nm, *Figure 3.4*). Though well-spaced regions were located and imaged, as shown in *Figure 3.2,* this morphology often presented as the densely entangled mats pictured in *Figure 3.3.* As homochiral KFE12 fibrils have comparable diameter (4.4 nm, *Figure 3.4*) and plate thickness (3.0 nm, *Table 3.1*), the twist predicted by energy-minimization modeling (*Figure 3.14C*) is visible only at high magnifications as slight oscillations in width (*Figure 3.2, inset*). By contrast, LDL and DLD twists

were made readily apparent by their increased diameter (12.5 ± 3.0 nm, *Figure 3.4*) and pitch (259 ± 45 nm, *Figure 3.5*). Reminiscent of heterochiral KFE8, the extent of edge stitching between β-sheets is variable, with twisted LDL and DLD ribbons ranging from two to five peptides in width (*Figure 3.4*). When compared to LDL and DLD, fibrils formed by LLD and DDL are entirely flat and approximately half as wide (6.3 ± 0.7 nm). In a significant departure from the otherwise fibrillar tendencies of their isomers, LDD and DLL instead form irregular, 2-D cross-β sheets with diameters ranging from 5–200 nm. Beyond individual sheets, multilaminar 3-D aggregates with diameters as large as 4 μm were observed in numerous independently prepared samples. This indicates that the smaller structures commonly observed alongside larger sheets (*Figure 3.2, inset*) may be fragments of assemblies fractured during solubilization and grid adsorption.

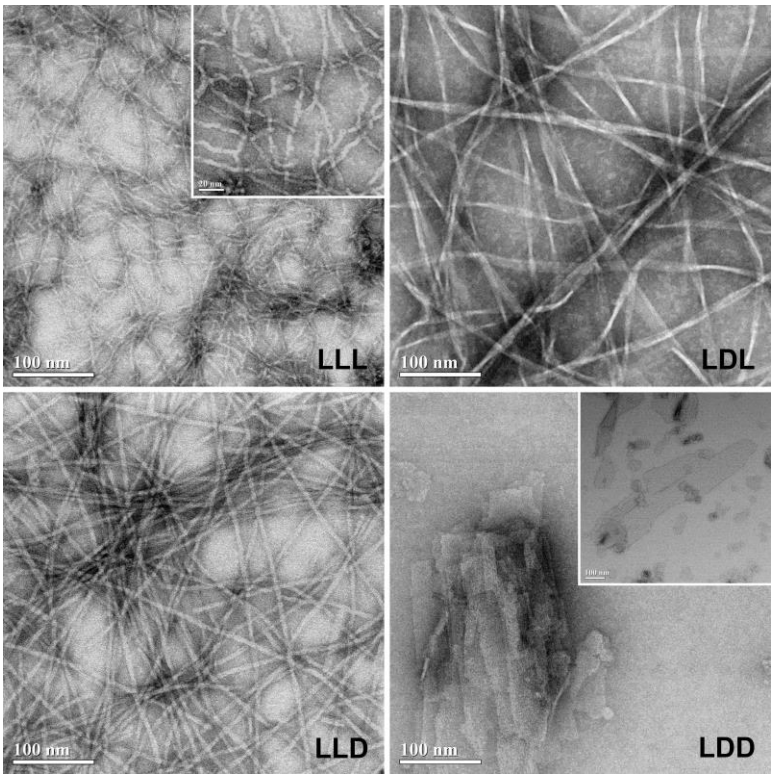

Figure 3.2. Representative scanning transmission electron microscopy images (800k) for LLL, LDL, LLD, and LDD at 0.10 mM in DI water (enantiomers in *Figure 3.3*). LLL inset: high-magnification image (1200k, 20-nm scale bar) with MD-predicted twists visible as slight oscillations in width. LDD inset: alternate, fragmented morphology (400k, 100-nm scale bar).

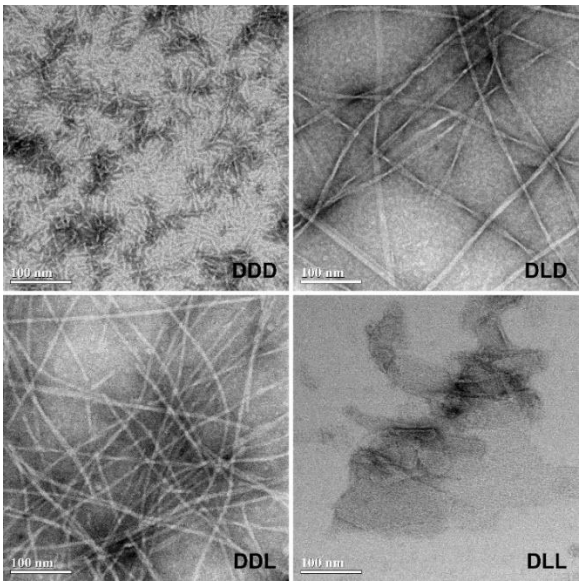

Figure 3.3. Representative STEM images for DDD, DLD, DDL, and DLL KFE12 at 0.10 mM in DI water.

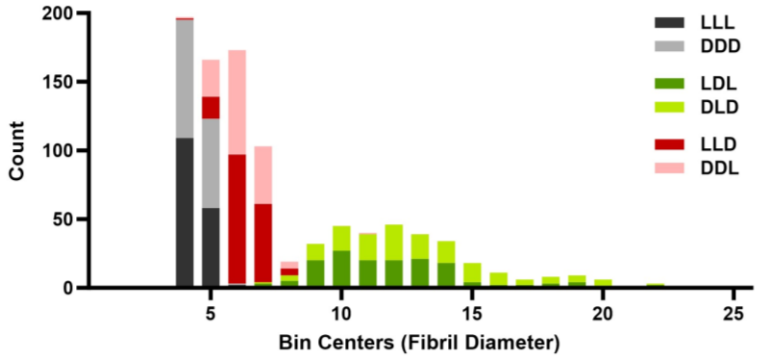

Figure 3.4. Histogram of KFE12 fibril width measurements. Data shown for LLL (4.4 ± 0.4 nm), DDD (4.5 ± 0.4 nm), LDL (11.9 ± 2.8 nm), DLD (13.0 ± 3.1 nm), LLD (6.3 ± 0.6 nm), and DDL (6.2 ± 0.8 nm). Minimum of n=150.

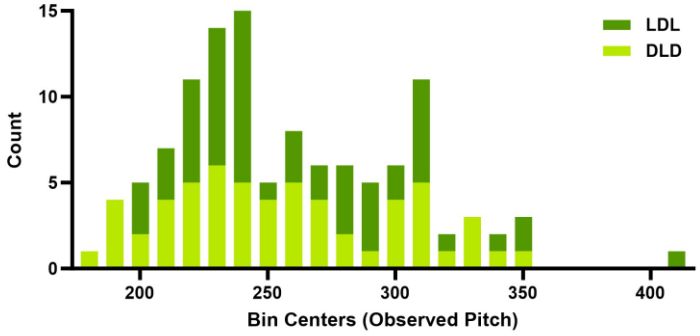

Figure 3.5. Histogram of LDL and DLD KFE12 twisted ribbon pitch. Data shown for LDL (261 ± 45 nm) and DLD (257 ± 44 nm). Minimum of n=50 for each analog.

3.5 Spectroscopic Analysis

Despite these substantial morphological differences, CD (*Figure 3.6*) and FTIR (*Figure 3.7*) confirm that all analogs share antiparallel cross-β secondary structure. In agreement with STEM data, enantiomer pairs produce mirror-image CD spectra, confirming that they differ only in handedness. In general, L- and D-homochiral β-sheets produce negative and positive Cotton effects, respectively, between 240 and 200 nm. The inherent imbalance of three-component binary systems grants all KFE12 isomers either majority-L or majority-D chiral composition. As a fundamental, relatively independent structural feature, interstrand H-bond networks and their associated n → π* transitions (~222 nm) (J. Miles & A. Wallace, 2016) are almost entirely defined by backbone chirality, with sign and magnitude at this wavelength dictated by the overall proportion of L- and D- amino acids within each analog. Interestingly, this rule only appears to hold true for the n → π* region for KFE systems. For instance, LLD is majority-L and, as expected, has negative sign at ~222 nm; at lower wavelengths, however, LLD is strongly positive with a prominent phenyl π-stacking peak at ~203 nm (π → π*) (J. Miles & A. Wallace, 2016). Along with its enantiomer DDL, LLD is the only block chiral KFE8 or KFE12 analog whose CD spectrum crosses zero in the β-relevant 260–200 nm range. Irrespective of this unique feature, the principal CD sign of all diblock and triblock and KFE isomers directly corresponds to the chirality of their C-terminal block. The dependence of both these trends on chiral composition and patterning illustrates the complexity of heterochiral interactions, as they hold true for all block chiral isomers of both KFE8 and KFE12.

LLL and DDD appear as classical cross-β CD signatures with a particularly pronounced trough (~208 nm) separating their two major peaks (*Figure 3.6*), reflecting a more narrowly defined π-stacking contribution due to their single-peptide width and thus lack of phenyl zippers and their

constitutive aromatic interactions that enable the multi-peptide width of all other KFE systems. LDL and DLD retain cross-β character, though their spectra are far more reminiscent of KFE8, with LDL (or DLD) appearing as a near-perfect superposition of LL and DL (or DD and LD) (*Figures 2.5, 3.6*) (Clover et al., 2020). This is particularly intriguing given that the width and pitch of LDL and DLD are intermediate to those of homochiral and heterochiral KFE8. The spectrum of LLD (or DDL) can be analogously described as a superposition of LL and LD (or DD and DL). Given that LLD contains overlapping LL and LD domains (and that DDL contains overlapping DD and DL domains), the opposite handedness of each pair of domains may serve to reduce or effectively eliminate any natural twist from LLD and DDL. The broad, largely featureless β-sheet signatures produced by LDD and DLL may reflect a multitude of less restrictive packing modes that enable their apparent multidimensional propagation (*Figure 3.2*).

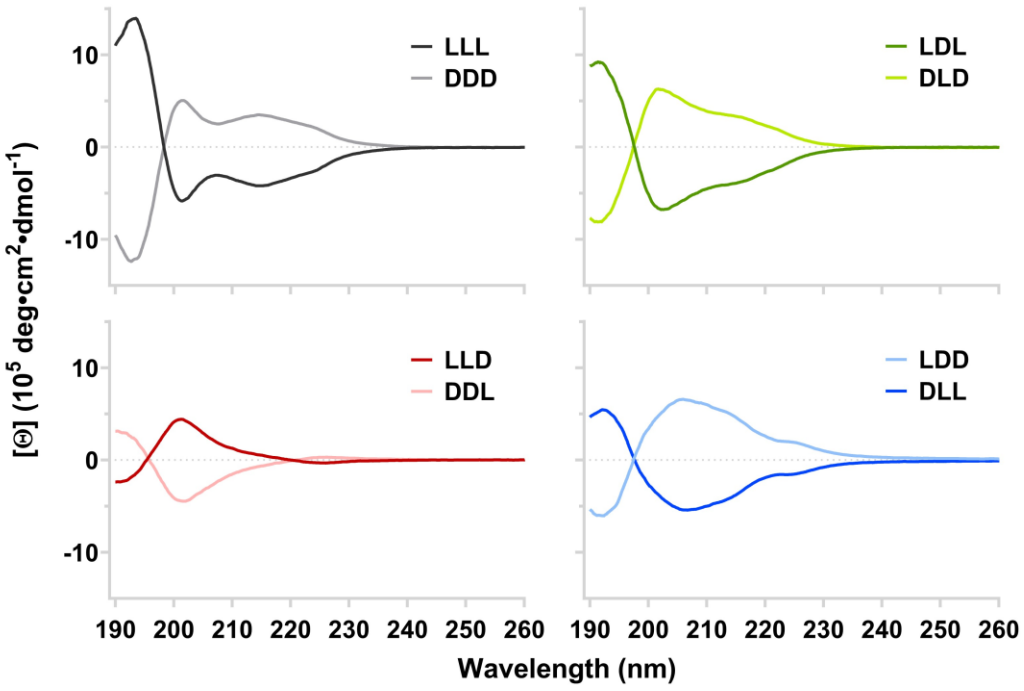

Figure 3.6. Circular dichroism spectra for the KFE12 analogs (0.10 mM) in water at room temperature, with β-sheet character is evident in all samples. Principal CD sign follows the chirality of the C-terminal blocks, apart from a narrow region at ~222 nm (n → π*) where sign corresponds to overall chiral composition.

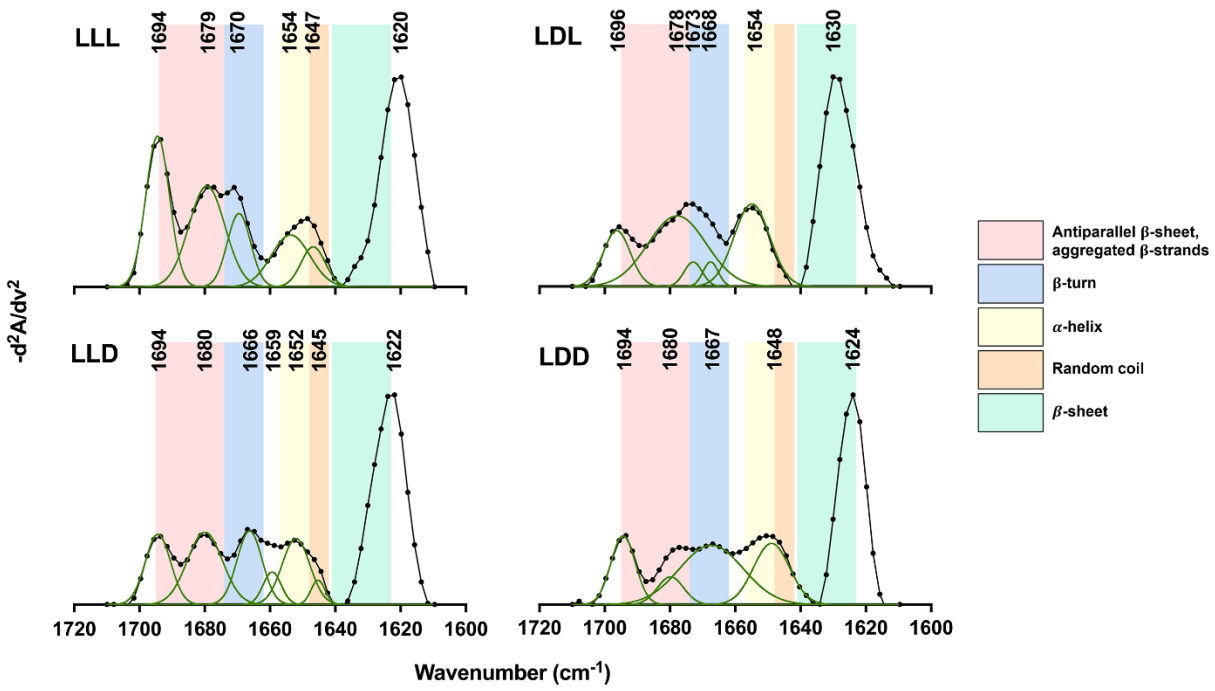

Figure 3.7. Second-derivative FTIR spectra and deconvolutions for LLL, LDL, LLD, and LDD. Experimental data shown in black, Gaussian deconvolution components shown in green.

3.6 Small- and Wide-Angle X-Ray Scattering

Small-angle X-ray scattering (SAXS) data for each KFE12 isomer and its enantiomer are similar, with only minor discernable differences emerging at low-q (*Figures 3.8, 3.9*). Due to their expansive multimodal assemblies and subsequently reduced solubility, LDD and DLL readily precipitate out of the high-concentration solutions required for X-ray diffraction studies. Holtzer plot analysis reveal interfilament scattering contributions for all heterochiral isomers, as supported by deviations from linearity at low-s values in their Guinier Plate plots (*Figure 3.10*), though no such scattering contributions are observed for the homochiral isomers LLL and DDD. While these factors affected Guinier radius of gyration (R_g) and cross-sectional radius (R_{cs}) calculations (*Table 3.1*), they did not fully obscure the region relevant to Guinier plate analysis.

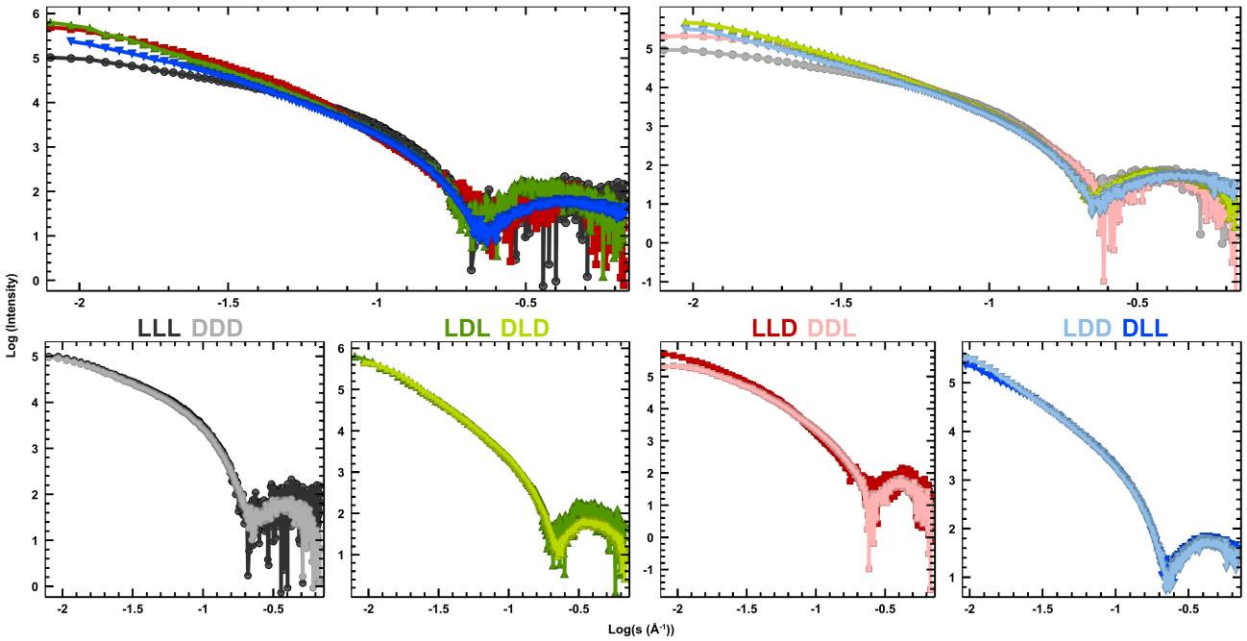

Figure 3.8. KFE12 SAXS Log-Log plots. The L- and D-dominant analogs are shown in the top-left and top-right, respectively. Individual enantiomer pairs are also shown in the bottom row for clarity.

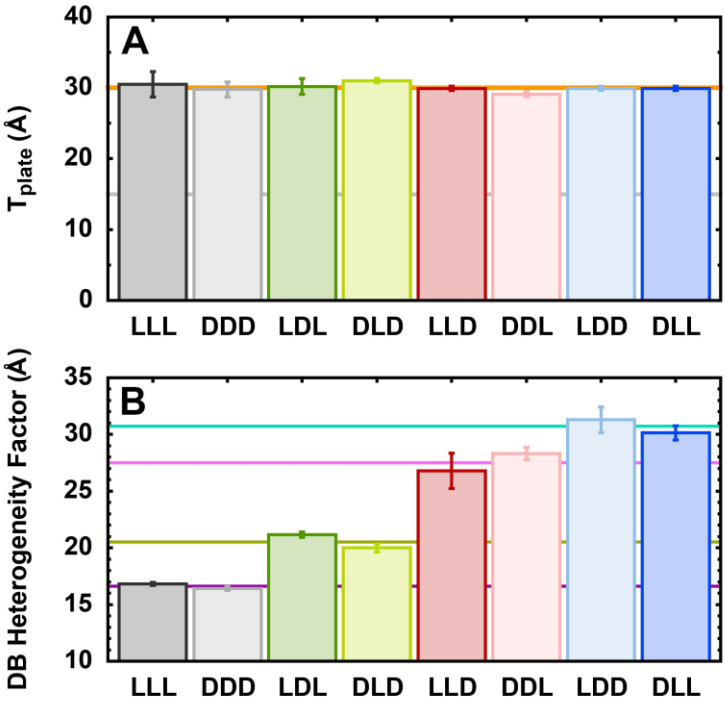

Figure 3.9. Notable SAXS parameter values. (A) The plate thickness for each peptide (*Figure 3.10*, *Table 3.1*). Orange line marks average thickness (30 Å) across all KFE12 peptides. Gray line marks single-sheet thickness. (B) Debye-Bueche heterogeneity values for each analog. Colored lines mark averages for each pair of enantiomers.

Despite their substantial morphological and spectroscopic differences, SAXS analysis found that the block chiral isomers of KFE12 have relatively similar underlying structural and assembly profiles. Fibril thicknesses, as measured by Guinier R_t analysis, were found to be virtually identical for all analogs, with T_{plate} ($\sqrt{12} \bullet R_t$) values ranging from 29.2 to 31.0 Å (*Figure 3.10*). Unlike heterochiral KFE8 (LD and DL), which were previously observed to form monolayer tapes, all block heterochiral KFE12 analogs retain the two-molecule thickness of their homochiral counterparts (*Figure 3.9A*).

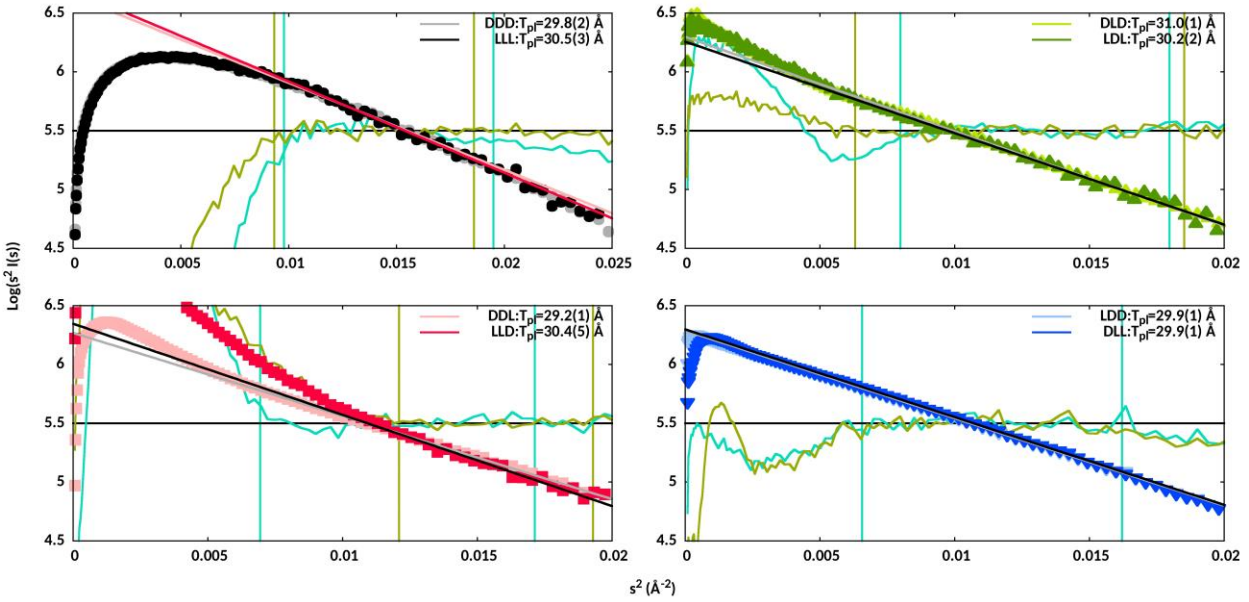

Figure 3.10. Guinier fitting of the SAXS data to a thin plate of thickness T_{plate}. Enantiomer pairs are shown together with their Guinier fits. Residuals are shown in green for the L-dominant analogs and in teal for the D-dominant analogs. The fitting range (vertical lines) was ~$0.8/R_t$ to ~$1.2/R_t$, as determined by best fit. Thickness values range from 29.2 to 31.0 Å.

Though SAXS showed that the samples lack the regular intermolecular spacings of cross-linked networks, high-concentration solutions produce porous self-supporting hydrogels consisting of physically entangled fibrils and interacting regions. The Debye-Bueche (DB) model produces a characteristic length (ξ) for each component that describes the spatial arrangement of fibrils and interacting regions (*Figures 3.9B, 3.11*) (Debye & Bueche, 1949). While the similarity between

$\xi_{LDL,DLD}$ (33, 30 Å) and $\xi_{LLD,DDL}$ (36, 28 Å) is unsurprising given their comparable morphologies, LDD and DLL produce nearly identical ξ-values (39, 32 Å) despite their atypical, nonfibrillar architecture. However, the homochiral KFE12 analogs LLL and DDD have far shorter characteristic lengths (16, 16 Å) that correspond to smaller contiguous regions with their gels.

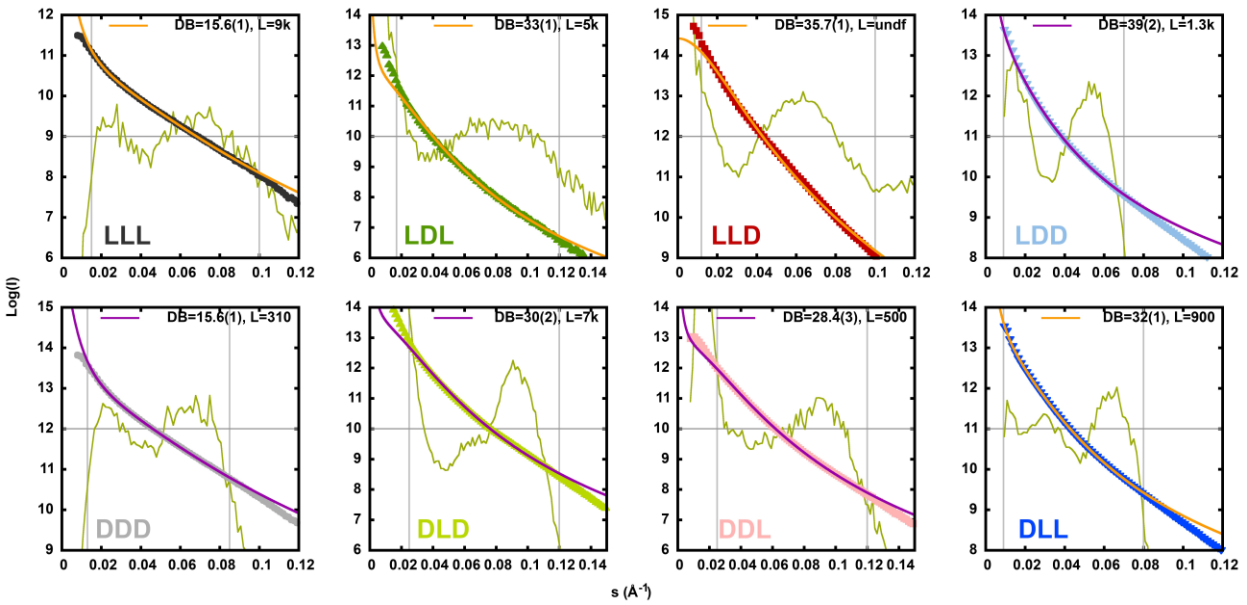

Figure 3.11. Debye-Bueche fitting of KFE12 SAXS data. The fitting range (vertical lines) was determined by best fit (±3σ). The Lorentzian contribution was ill-defined for L>1000 Å. Debye-Bueche heterogeneity factors range from 16 to 39 Å (*Figure 3.9*, *Table 3.1*).

Table 3.1. SAXS characteristics of the peptide filaments and gels.

Peptide	Rg (Å)	Filament R_{cs} (Å)	Thickness T_{plate} (Å)	Chain Length (Å)	Debye-Bueche (Å)
LLL	83*	15*	30.5(3)	9000*	15.6(1)
DDD	83*	15*	29.8(2)	300*	15.6(1)
LDL	141*	48*	30.2(2)	4000*	33(1)
DLD	108*	44*	31.0(1)	7000*	30(2)
LLD	121*	43*	30.4(5)	1000*	35.7(1)
DDL	83*	28*	29.2(1)	1000*	28.4(3)
LDD	128*	33*	29.9(1)	1000*	39(2)
DLL	123*	32*	29.9(1)	1000*	32(1)

*Curves not linear/value not well-defined

Table lists the Guinier radius of gyration (R_g), filament Guinier cross-sectional radius (R_{cs}), Guinier sheet thickness (R_t, $T_{plate}=\sqrt{12}\bullet R_t$), Gaussian chain correlation length, and Debye-Bueche heterogeneity parameter for each peptide.

Rather than the network-scale differences in density depicted by SAXS, wide-angle X-ray scattering (WAXS) describes regular atomic arrangements (d-spacings) within the individual suprastructures that compose these networks. KFE12 analogs demonstrate amorphous scattering from the random mixture of filaments in the gel that obscure some particularly fine details. All diffraction curves have broad minima at 2θ-values of 12° and 29° (*Figure 3.12A*), along with a broad maximum in the Cα-Cα region (23.6°, d-spacing=3.8 Å) (*Figure 3.12A,B*). Each KFE12 curve is dominated by a major antiparallel β-sheet peak at 2θ=18.8° (4.72 Å) that is asymmetrically widened by several β-mismatch peaks at slightly higher angles. The closely related 2×β-sheet spacing at 2θ=9.5° (9.31 Å) is observed for the heterochiral KFE12 isomers, as expected, but is curiously absent in LLL and DDD, though these do have a nearby d-spacing at ~9.5 Å. Another common feature in cross-β fibrils, the $A\beta_{42}$-repeat peak (15.6°, 5.6 Å), is present in all isomers except those with two internal chiral interfaces (LDL and DLD). Apart from these peaks, most KFE12 WAXS curves are otherwise effectively featureless. Unlike other isomers, LDD and DLL display numerous minor peaks with significant intensity (*Figure 3.12B*), indicating that their visually amorphous morphology is the product of multiple coexisting intermolecular selectivities.

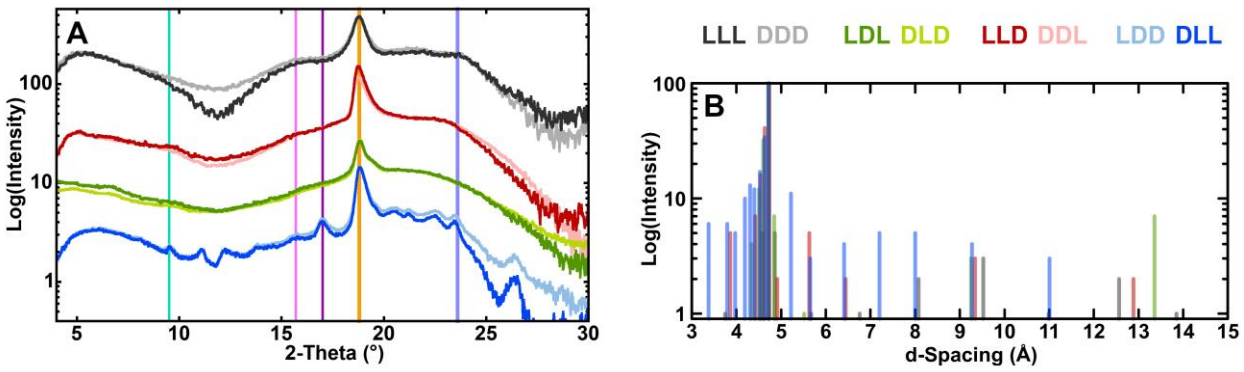

Figure 3.12. WAXS diffraction peaks for 10-mM gels of the block chiral KFE12 analogs. (A) WAXS curves (offset for clarity). Common features highlighted by colored vertical lines: 2×β-sheet at d=9.31 Å, Aβ(42) at d=5.68 Å, a peak unique to LDD and DLL at d=5.28 Å, β-sheet at d=4.72 Å, and Cα-Cα at d=3.77 Å. (B) d-spacing plot.

Table 3.2. Summary of the WAXS data collection and results.

Peptide	LLL	DDD	LDL	DLD	LLD	DDL	LDD	DLL
mg/mL	17	17	17	17	17	17	17	17
s_{min} (Å^{-1})	0.7[b]	0.7[b]	0.7[b]	0.7[b]	0.7[b]	0.7[b]	0.7[b]	0.7[b]
s_{max} (Å^{-1})	5.36/6.72	5.36/6.72	5.36/6.72	5.36/6.72	5.36/6.72	5.36/6.72	5.36/6.72	5.36/6.72
Peak (Å)	4.720	4.725	4.714	4.713	4.733	4.734	4.712	4.714
Peak (Å)	-	-	-	-	4.636	4.634	4.620	4.623
Peak (Å)	4.588	4.586	4.598	4.599	-	-	-	-
Peak (Å)	-	-	4.502	4.512	4.535	4.532	4.520	4.523
Peak (Å)	-	-	-	-	-	-	5.626	5.651
Peak (Å)	-	-	9.253	9.368	9.337	9.171	9.300	9.274
Peak (Å)	-	-	4.339	4.240	-	-	4.345	4.307

[b]The Beamstop shadow is diffuse and the start of unaffected data is uncertain. Peaks are sorted by relative intensity (high to low).

3.7 Molecular Dynamics Modeling

To further elucidate differences between the packing modes of KFE8 and KFE12, LLL KFE12 modeling was performed based on X-ray scattering data and a published model for KFE8 (Hwang et al., 2003). These two-peptide-thick, one-peptide-wide antiparallel β-sheets could form in two possible configurations with an equal number of backbone H-bonds: one in which the acetylated N-termini are more solvent-exposed ('ACE'), and one in which the amidated C-termini are more solvent-exposed ('CT2'). Molecular dynamics simulations of these two initial models found a rapid stabilization of their helical twists at slightly different characteristic values. After 10 ns of fully solvated MD, the ACE and CT2 models settle at -9.8° and -5.6°, respectively (*Figure 3.13A*). Though the non-bonded interaction energies of both models are relatively similar, it was found to be 77 kcal/mol/strand lower for the ACE model, indicated that like LL KFE8, LLL KFE12 exhibits a one-residue register shift toward the N-terminus (*Figure 3.13B*).

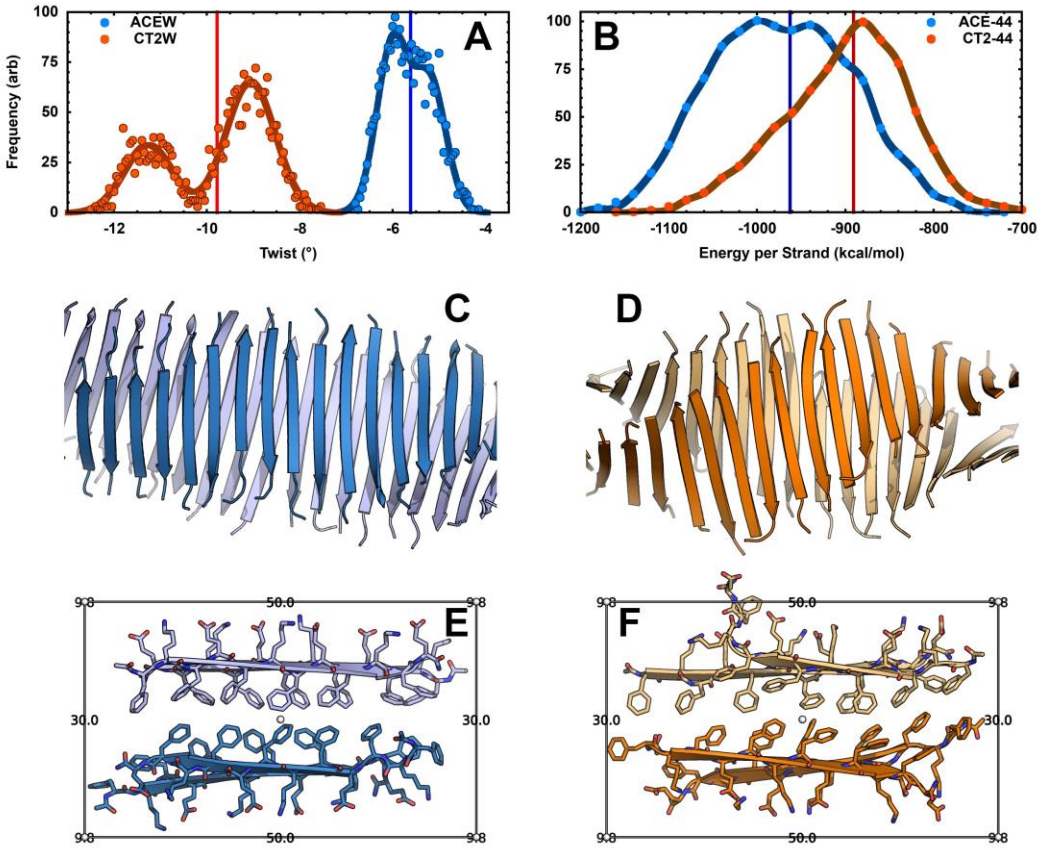

Figure 3.13. (A) Filament twist distribution of the LLL models (final 5 ns). Mean twist was calculated as -5.6° for the ACE model and -9.8° for the CT2 model. (B) NAMD free energy distributions of the two LLL models (ACE ● and CT2 ●), ΔE = -77 kcal/mol/strand. (C) The ACE model after 10 ns of MD. (D) The CT2 LLL model after 10 ns of MD. (E,F) The filament a.u. for each model. The filament thickness of 30 Å (SAXS, *Figure 3.10*), is represented by the box height. The u.c. bounding box is 30 x 50 x 9.48 Å. The ACE filament is represented by a bounding box translated along the z-axis and rotated -11.2°.

The resulting filament model matches the SAXS data in multiple analyses, including its 30-Å thickness and 16-Å cross-sectional radius (*Table 3.1*), with χ^2 values of 3.3 for ACE and 3.7 for CT2. While ensemble modeling with filaments up to 250 nm in length improves χ^2 to 2.1 (*Figure 3.14*), including filaments up to 400 nm long further improves the fit, reducing χ^2 to 1.7. The ensembles included filaments covering a wide range of lengths, from short protofilaments to filaments up to 400 nm long (*Figure 3.15*).

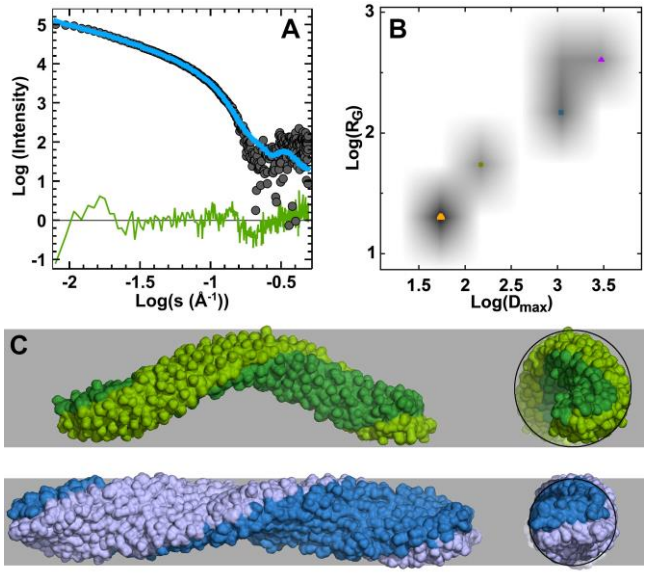

Figure 3.14. Energy-minimization modeling of LLL KFE12. (A) Fitting of the LLL SAXS data (χ^2=2.1) with (B) an ensemble of model filaments, from small to moderately large (D_{max} up to 2500 Å). (C) Model filaments of LL KFE8 (green) and LLL KFE12 (blue). SAXS-derived fibril diameters are illustrated by the gray rectangles (background) and circles (right). The KFE8 model represents approximately a half-turn, while the KFE12 model is one full turn.

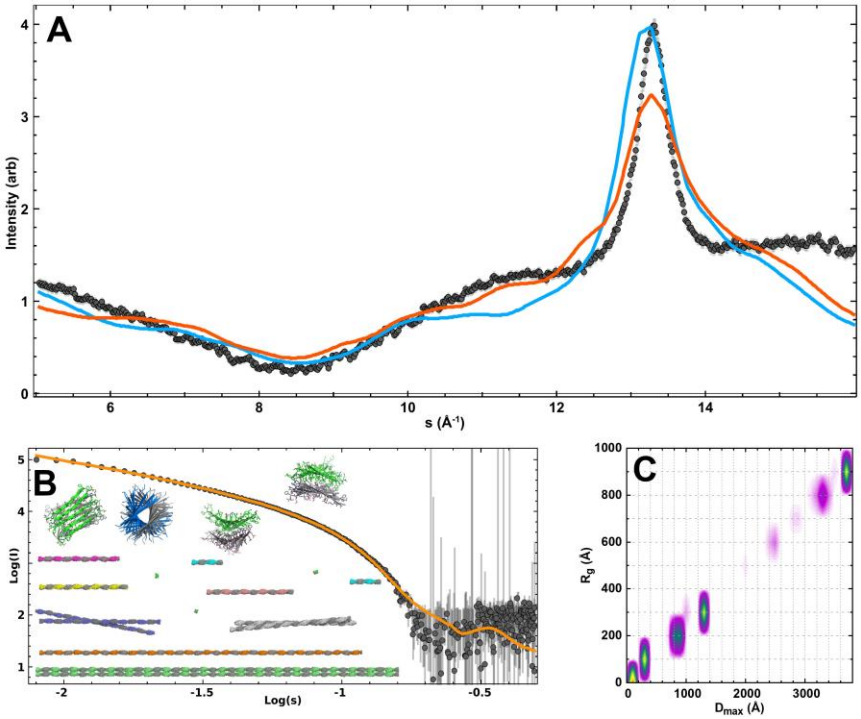

Figure 3.15. SAXS and WAXS ensemble fitting to the LLL filament MD models. (A) The WAXS data fit with two short (2x22 strand) MD filament models ACE — and CT2 —. The major features of the near-WAXS curve, the dip at s~8.4 Å^{-1} and the β-sheet peak at s~13.3 Å^{-1}, are replicated in the scattering from both filament models. (B) The EOM ensemble fitting of filament models to LLL (χ^2=1.7). The filament models selected by EOM are shown. (C) EOM distribution 2-D plot. The color scale indicates relative frequency of selection from none (white), to infrequent (purple), to more frequent (blue, green, yellow), to most frequent (red).

3.8 Rheology

As fibrillar assemblies entangle into hydrogels at high concentration, 10-mM hydrogels of the triblock chiral KFE12 isomers were analyzed using an HR-20 rheometer fitted with a 20-mm smooth parallel-plate geometry. Three independently prepared replicates of each sample were evaluated with constant parameters set to 0.1 Hz (strain sweeps), 1% oscillatory strain (frequency sweeps), or both (time sweeps). As in previous experiments, in particular X-ray scattering sample preparation, LDD and DLL largely precipitated and were excluded from subsequent analysis. Time sweeps demonstrated shear recovery for all gels, reaching stable dynamic moduli within 10 minutes of extrusion through a 22-gague needle.

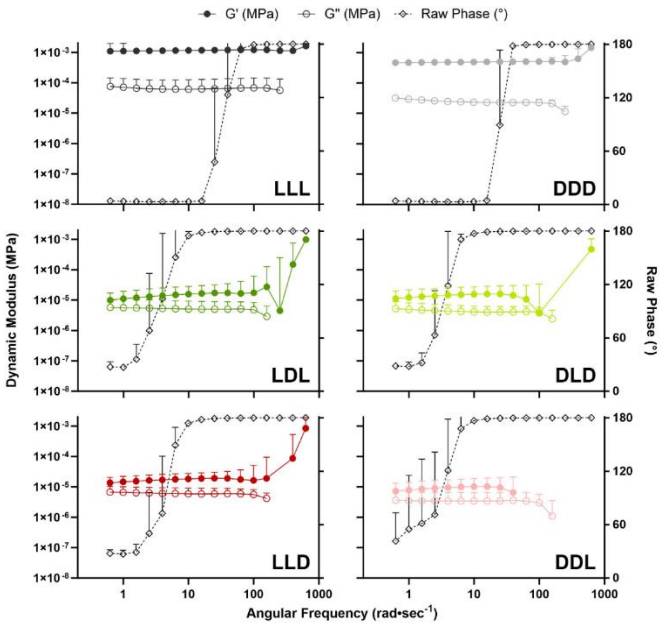

Figure 3.16. Frequency sweeps for LLL, DDD, LDL, DLD, LLD and DDL hydrogels (10 mM). Dynamic modulus is shown on left y-axis and raw phase on the right y-axis. Data is clearly valid for datapoints corresponding to raw phases lower than ~180°, while data corresponding to high raw phases may include measurement artifacts.

Frequency sweeps from 100 to 0.1 Hz had low raw phase (well below 180°), verifying measurement validity below ~4 Hz for LLL and DDD and below ~0.6 Hz for LDL, DLD, LLD,

and DDL (*Figure 3.16*). All formulations remain viscoelastically solid (G′ > G″) for all low-raw-phase frequencies. The hydrogels also exhibit shear-thinning behavior in this range (*Figure 3.17*), demonstrating suitability as injectable biomaterials (Guvendiren et al., 2012).

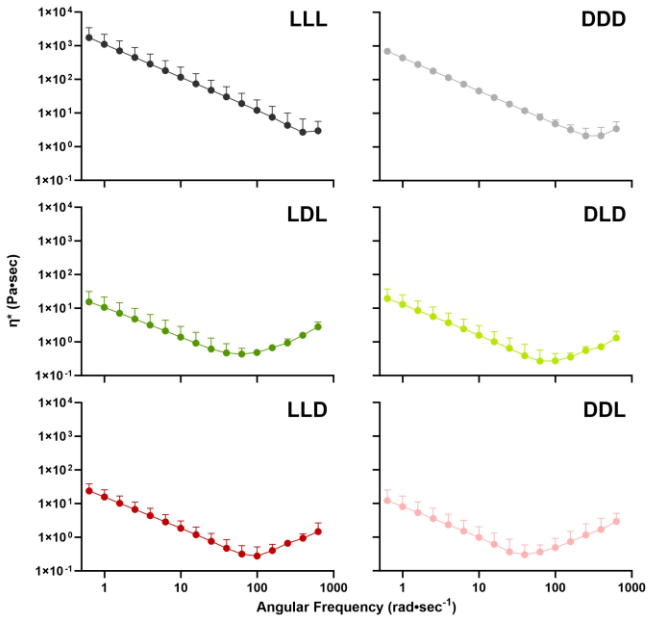

Figure 3.17. Complex viscosity as calculated based on frequencies and dynamic moduli from frequency sweeps for LLL, DDD, LDL, DLD, LLD and DDL hydrogels (10 mM). The downward trend indicates shear-thinning behavior.

During strain sweeps, raw phase remained low for oscillatory strain levels between 0.1% and 100% (*Figure 3.18*). Crossover points, where gels transition from primarily elastic to viscous behavior, were measured as approximately 31% and 55% for LLL and DDD, 6% for LDL and DLD, and 6% and 10% for LLD and DDL. The linear region, or the strain regime in which phase angle remains effectively constant, was determined to be below 2.5% and 10.5% for LLL and DDD, below 1.0% and 6.3% for LDL and DLD, and below 0.6% and 1.0% for LLD and DDL (*Figure 3.19*).

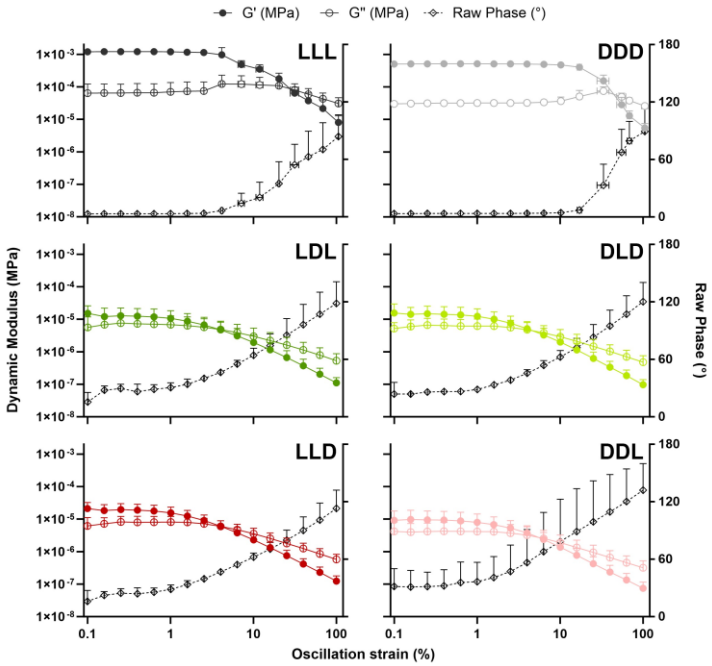

Figure 3.18. Strain sweeps for the hydrogels, with dynamic modulus (MPa) on the left y-axis and raw phase (°) on the right y-axis. Raw phase is well below 180° at all points shown, indicating the data is valid and not dominated by momentum of the measurement instrument. The homochiral gels (LLL and DDD) have much higher dynamic moduli ($G' \sim 10^{-3}$ MPa) than the heterochiral gels ($G' \sim 10^{-5}$ MPa). Crossover points are also at greater strains for the homochiral gels. All gels have $G' > G''$ for low oscillatory strain, indicating that they are viscoelastic solids up to a certain strain, after which they become viscoelastic liquids ($G'' > G'$).

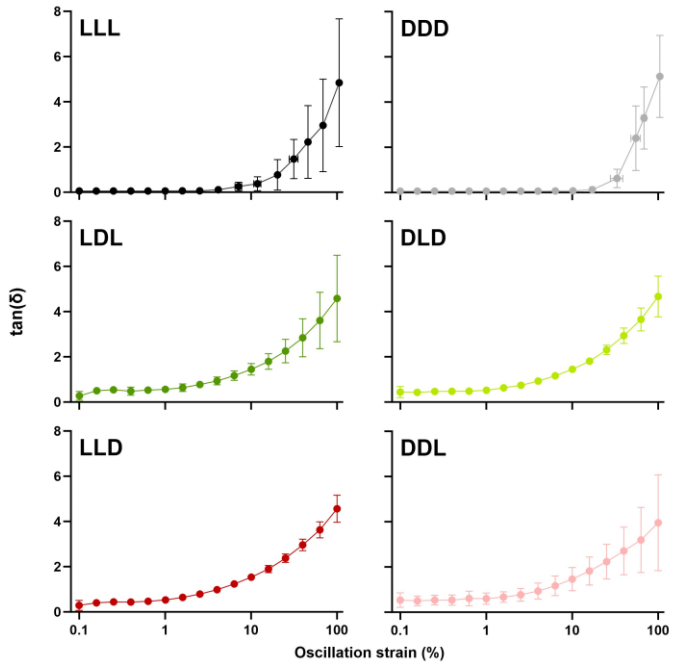

Figure 3.19. Phase angle determined during strain sweeps for LLL, DDD, LDL, DLD, LLD and DDL hydrogels (10 mM). Gels are within their linear range where tan(δ) remains approximately constant. The homochiral peptides tend to have linear ranges that extend to substantially higher oscillatory strains than the heterochiral peptides.

3.9 Conclusions

Early studies into the effects of chirality on peptide assembly primarily focused on single-residue or full-molecule D-substitution. The recent emergence of patterned chiral inversion as a complementary design tool gives rise to unique intermolecular selectivity that fundamentally alters the behavior of well-established model systems. By applying this concept to a simple, repetitive sequence such as KFE12, we illustrate the widely diverse influence of chiral blocking on material properties ranging from packing mode and supramolecular morphology to hydrogel mechanics. Through a combination of microscopic, spectroscopic, and computational techniques, we describe the complex interplay between enantiomeric repeat units in self-assembling triblock heterochiral peptides and the dramatic differences induced by simple reordering of these units. This work has further developed our understanding of block chiral patterning and confirmed that this strategy can be extended beyond two-component systems, supporting the potential for generalization to other self-assembling peptide classes. In concert with existing design elements, ordered chiral patterning provides an exponentially broader set of building blocks from which to construct synthetic molecular assemblies, representing a simple yet incredibly powerful tool for the creation and tailoring of custom biomaterials.

Chapter 4: Stereoselective Coassembly of Diblock Chiral Isomer Pairs

4.1 Abstract

Peptide coassembly can be described as the formation of nanostructured materials through precise interactions between molecules with differing atomic connectivity or arrangement. Much like single-species self-assembly, coassembly is primarily driven by hydrogen bonding, electrostatic interactions, and hydrophobic packing. As dictated by the proportions and arrangement of these non-covalent forces, highly specific association preferences give rise to an assortment of supramolecular architectures including fibrils, nanotubes, or sheets with distinct structural and macroscale properties. In contrast to coassembly, self-sorting occurs when orthogonal interactions drive each of its components to selectively associate with 'self' monomers, resulting in coexisting populations of distinct single-analog assemblies. Peptide coassembly and self-sorting are sophisticated processes that allow for the creation of complex nanoscale structures, enabling fabrication of novel functional biomaterials. In this work, we apply the principles of stereocomplexation-driven enantiomeric coassembly in the context of the remarkable structural uniquities presented by 'block heterochiral' peptides, or oligopeptides composed of repeat units with opposite chirality. By utilizing homochiral and diblock heterochiral analogs of the model cross-β peptide KFE8, we explore the intricate pairwise assembly behaviors of chemically identical self-assembling peptides differentiated only by segmented stereoisomerization.

4.2 Introduction

Spontaneous or triggered hierarchical organization of molecules via self-recognition is an essential and ubiquitous process in nature. This phenomenon has been exploited to fabricate functional nanomaterials with diverse biomedical applications ranging from regenerative medicine to bioelectronics depending on the imbued physicochemical properties (Huo et al., 2023; S. Zhang, 2020). Peptide-based systems have garnered particular interest in part due to their inherent tractability, multivalency, and biocompatibility. To further expand the latent space in terms of structural diversity and functional scope, multicomponent peptide 'coassembly' into supramolecular fibrils has recently evolved as an intriguing approach to expand the array of possible systems and exploit the intrinsic modulable nature of multi-species formulations (Makam & Gazit, 2018). Much like copolymer chemistry paradigms, the coassembly process can be cooperative (referred to in this work simply as 'coassembling'), orthogonal ('self-sorting'), random, or destructive (Adler-Abramovich et al., 2016).

In its simplest form, peptidic coassembly typically involves preferential association of a given self-assembling peptide with a modified form that is often designed with charge- or shape-complementarity that promotes complexation between the two species (Raymond & Nilsson, 2018; Seroski et al., 2020). Chirality is a simple geometric property that describes mirror-image, nonsuperimposable molecules (*Figure 1.2*). As interactions between molecules of the same or opposite chirality are characterized by different association strengths and kinetics, chiral self-recognition has been widely used for creating functional materials from racemic components capable of autonomous organization into separate entities (Tateishi et al., 2018). While polymer and organic chemists have exploited chirality to induce self-sorting, it was predicted by Pauling and Corey that equimolar mixtures of enantiomeric peptides would pack into rippled β-sheets

composed of alternating L- and D-isomers (Pauling & Corey, 1953). This prediction has been proven true for a number of systems, including L- and D-KFE8 and the β-hairpin peptides L- and D-MAX1 (Nagy et al., 2011; Swanekamp et al., 2012). Beyond homochiral enantiomer coassembly, our lab has demonstrated (*Chapter 2*) that 'block heterochiral' analogs of KFE8, containing two 'FKFE' repeat motifs of opposite chirality, assemble into helical tapes with dimensions greatly exceeding those of their fibrillar homochiral counterparts (Clover et al., 2020). Though this is a single-species system, self-assembly of heterochiral peptides relies on this same concept, stereocomplexation, to guide self-assembly of the block heterochiral analog LD (FKFEfkfe) or its enantiomer DL (fkfeFKFE).

Given the racemic coassembly of homochiral KFE8 and the ability of block heterochiral KFE8 to self-assemble, this study aims to determine the extent of and prerequisites for coassembly of KFE8 analog pairs with differing block chiral patterns, as depicted in *Figure 4.1*. To this end, we explore the nano-, micro-, and macroscale properties of LL/LD, LL/DL, DD/LD, and DD/DL, each of which represents two equimolar stereoisomers mixed before solubilization ('pre-mixed') to permit prospective coassembly within a single, well-mixed monomer phase. In this work, we use a related notation (e.g., LL+LD) to refer to 'post-mixed' systems, which were allowed to assemble independently and were only mixed and gently vortexed 30 seconds prior to data collection for each technique. This simple procedure prohibits substantive coassembly, as the monomer phase of each is depleted within nanoseconds of initial solubilization, and thus enables standard analyses to be complemented by direct comparison of pre- and post-mixed samples with identical monomer identities and proportions. While the racemic pair LD/DL is also included in this study, we refer the reader to a previous publication on LL/DD by the Nilsson group (Swanekamp et al., 2012).

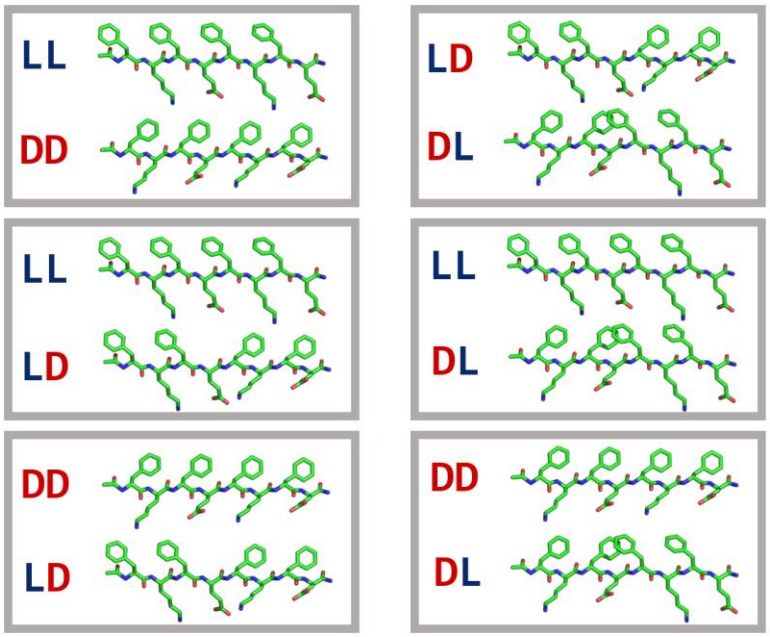

Figure 4.1. PyMOL representations of the diblock chiral KFE8 isomer pairs. Red letters indicate D-chirality. Enantiomeric pairs are shown in the top row, homochiral/heterochiral pairs are shown in rows two and three.

4.3 Methods

Peptide Synthesis. Peptides were purchased from P3 BioSystems (Louisville, KY) for microscopic and spectroscopic studies. Isotope-edited peptides were purchased from GenScript Biotech (Piscataway, NJ). Peptides for rheology studies were synthesized on a CEM (Matthews, NC) Liberty Blue automated synthesizer using Fmoc chemistry. Rink amide MBHA (4-methylbenzhydrylamine) resin from Novabiochem (Burlington, MA) was first swelled for one hour, followed by double coupling of residues using DIC (*N*,*N*'-diisopropylcarbodiimide) and Oxyma (ethyl cyano(hydroxyimino)acetate). Synthesized products were cleaved in a solution containing TFA (trifluoroacetic acid), TIS (triisopropylsilane), and water (95:2.5:2.5). After pelleting crude products via centrifugation, five cold diethyl ether washes were performed, followed by freezing at -80°C, lyophilization, and storage of resulting powders at -20°C.

Peptide Purification and Identification. Crude peptide products were solubilized in 1:1 acetonitrile (ACN)/TFA and purified to >90% purity via reverse-phase HPLC on an Agilent (Santa Clara, CA) RP-C18 column (Zorbax SB-C18, 21.2 x 150 mm, 5 μm) on a Variant Pro-Star system with ACN/H_2O gradients with 0.1% TFA. For semi-preparative purification, an identical gradient at a flow rate of 18 mL/min was used and was monitored by absorbance at 214 and 254 nm, during which fractions were collected, frozen, and lyophilized. Purity was confirmed by analytical HPLC using an Agilent RP-C18 column (Poroshell 120 SB-C18, 4.6 x 150 mm, 2.7 μm). Peptide identities were confirmed by MALDI-TOF-MS with a Bruker Daltonics (Billerica, MA) α-cyano-4-hydroxycinnamic acid matrix.

Peptide Self-Assembly. To prepare peptide pair aliquots, each peptide was massed using a Sartorius (Göttingen, Germany) Quintex 65-1S semi-micro analytical balance and solubilized in 1:1 acetonitrile (ACN)/DI water to preclude assembly. These solutions were then mixed in appropriate proportions to produce 'pre-mixed' aliquots with 1:1, 3:1, or 1:3 isomer ratios, after which they were thoroughly vortexed, frozen overnight at -80°C, and lyophilized for 48 hours to ensure complete dehydration and monomerization. Isomerically pure stocks for 'post-mix' samples were prepared in parallel. 24 hours prior to performing analytical techniques, pre-mixed aliquots and single-analog stocks were thawed, solubilized in DI water, briefly vortexed, and kept at 4°C overnight. To preclude coassembly, post-mixed stocks were assembled independently of each other and were only mixed 30 seconds prior to data collection.

Transmission Electron Microscopy. Solutions of KFE8 isomer pairs were applied directly to a 200-mesh carbon-coated copper grid for 30 seconds. Grids were stained with 2% uranyl acetate (UA) for 1 minute. Grid preparation otherwise followed the protocol described in *Section 3.3*. TEM micrographs were captured on a JEOL JEM-2100 TEM with 200-kV accelerating voltage.

Width and Pitch Measurements. TEM images were processed in ImageJ. Length scales were set using scale bars generated by native JEOL software. Width measurements were performed by measuring the length of lines constructed perpendicular to nanofiber or tape edges. Pitch measurements were analogously performed with lines spanning two helical half-turns.

Circular Dichroism. CD spectra of the KFE8 pair solutions (0.25 mM in water) were collected using a Jasco (Hachioji-shi, Japan) J-815 circular dichroism spectrometer for wavelengths between 260 and 190 nm. Data acquisition was performed at 20°C in a Hellma (Plainview, NY) quartz cuvette (110-1-40) with 1-mm path length. Parameters were set to 1.00 nm-bandwidth, two-second D.I.T., and 0.5-nm step. A graphing software was used to subtract background and convert to molar ellipticity.

Fourier-Transform Infrared Spectroscopy. Attenuated total reflectance-Fourier transform infrared (ATR-FTIR) spectra were obtained on a Bruker (Billerica, MA) Alpha II FTIR employing a zinc selenide crystal. Peptide aliquots were gelated in ultrapure DI water and diluted to a final concentration of 15 mM. Background and solvent spectra were acquired prior to collecting each absorbance spectrum. Spectra were generated from 264 scans (4 cm^{-1} step) and data processing was performed in Thermo Scientific (Waltham, MA) GRAMS/AI software. After subtracting background, a third-order, nine-point-window Savitzky-Golay filter was applied before calculating second-derivative curves. This was then inverted, truncated (1710–1610 cm^{-1}), and baseline-corrected assuming flat baseline segments between local minima. Within this range, Gaussian deconvolution peak identification and fitting was performed with medium sensitivity level and a full width at half maximum (FWHM) height of eight cm^{-1}, as informed by Akaike Information Criterion (AIC), and these Gaussian components were then compared to published secondary structure ranges (Barth, 2007; Dong et al., 1990; Jackson & Mantsch, 1995).

Small-Angle X-ray Scattering. SAXS data for the KFE8 isomer pairs was collected using a Rigaku (Woodlands, TX) BioSAXS-1000 camera on an FRE++ X-ray generator, outfitted with an ASC-96 Automated Sample Changer (held at 10°C). Detector calibration was performed per the manufacturer's recommended procedure using a silver behenate powder sample. Samples were prepared by dissolving purified and pre-massed aliquots in double-distilled water at 1 mg/mL, with the exception of DD/DL (1.7 mg/mL). Centrifugation and vortexing were performed to ensure proper mixing and resuspend any larger particles. Although the samples gelated, the hydrogels retained fluidity under hydrostatic pressure and could be pipetted. Data processing was performed in SAXSLab (Rigaku) and SAXNS-ES (https://xray.utmb.edu/SAXNS). Analysis was performed in Primus/GNOM (Manalastas-Cantos et al., 2021), BIFT (Hansen, 2000; Larsen & Pedersen, 2021) and gnuplot (http://www.gnuplot.info).

Rheology. For rheology studies, KFE8 isomer pair hydrogels were prepared at 10 mM in DI water. The gels were then extruded via needle onto the stage of a TA Instruments (New Castle, DE) Discovery HR-20 rheometer. After extrusion, the 20-mm-diameter flat geometry was lowered to a 500-μm gap height. Gels were centered and sheared to failure by rotation at 1 radian/second (10-second minimum), after which rotation was stopped and the experimental sequence was initiated. This consisted of a 5-minute time sweep while fixed at 0.1-Hz frequency and 1% oscillatory strain. Following this, each gel was rested (30 seconds) before beginning a frequency sweep from 100 to 0.1 Hz while fixed at 1% oscillatory strain. After concluding this sweep, a subsequent oscillatory strain sweep was performed, ranging from 0.1% to 100%, with frequency fixed at 0.1 Hz. Three independently prepared gels were assessed for each KFE8 isomer pair. Storage modulus (G′) and loss modulus (G″) were recorded for all runs, along with phase angle (δ) and raw phase (°) to verify data quality.

4.4 Transmission Electron Microscopy

Pairwise assembly behaviors were initially assessed via negative-stain transmission electron microscopy (TEM), revealing a fascinating dichotomy between relative chiral patterns. For homochiral/heterochiral pairs with matching C-terminal block chirality (LL/DL and DD/LD), micrographs present both homochiral fibrils (~7-nm width, ~20-nm pitch) and heterochiral tapes (~50–150-nm width, ~1-μm pitch) in parallel with no apparent tertiary population (*Figure 4.2*). In stark contrast, neither LL fibrils nor LD tapes are observed in their pre-mixed formulation, instead appearing exclusively as a previously unseen suprastructure whose morphological properties appear to implicate features from both of its constituents, as both the width and helical geometry of the coassembled fibrils are intermediate to those of its pure components. Both LL/LD and its pre-mixed enantiomer set (DD/DL) coassemble into reliably three-peptide-wide (12.7 ± 1.5 nm, 12.3 ± 1.2 nm) architectures with exceptionally regular helical pitch (155.4 ± 11.4 nm, 155.9 ± 11.0 nm). Though a number of solutions appear truly equimolar, as shown for LL/LD in *Figure 4.2*, others appear with the minor molar excesses expected for microgram-scale materials preparation. One such instance is seen in *Figure 4.2* for DD/DL, with a small proportion of DD fibrils present alongside, and interestingly often branching from, DD/DL coassemblies.

As opposed to the variable lateral aggregation seen in other KFE systems, such as LD and DL (*Chapter 2*) or LDL and DLD (*Chapter 3*), the remarkably reliable three-peptide width of LL/LD indicates that this characteristic is likely a prerequisite for its stability in solution. As lateral aggregation depends on long-range π-stacking within phenyl zippers formed by overhanging N-terminal phenylalanines, the matched N-terminal chirality of the LL/LD and DD/DL coassembling pairs presumably preserves the precise sterics at the N-terminus required for long-range edge stitching. This concept is supported by the single-peptide width of coassembled LL/DD ripped β-

sheets reported by the Nilsson group, whose lack of lateral aggregation contrasts the two-peptide width of both LL and DD and implies that N-terminal chirality plays a significant role in the cohesive edge-to-edge interactions between adjacent β-sheets in multicolumnar suprastructures (Marchesan, Waddington, et al., 2012; Swanekamp et al., 2012).

Though narrower on average than LD or DL alone, pre-mixed LD/DL assemblies remain considerably wider (38.2 ± 9.1 nm) than all other fibrillar KFE morphologies (*Figure 4.2*). While no definitive conclusions can be drawn from this data alone, these tapes also lacked any form of consistent helicity. This departs from the micron-length pitch of enantiomerically pure LD or DL tapes, potentially indicative of twist-cancelling within their prospective coassemblies, though complementary spectroscopic studies are necessary to confirm this observation.

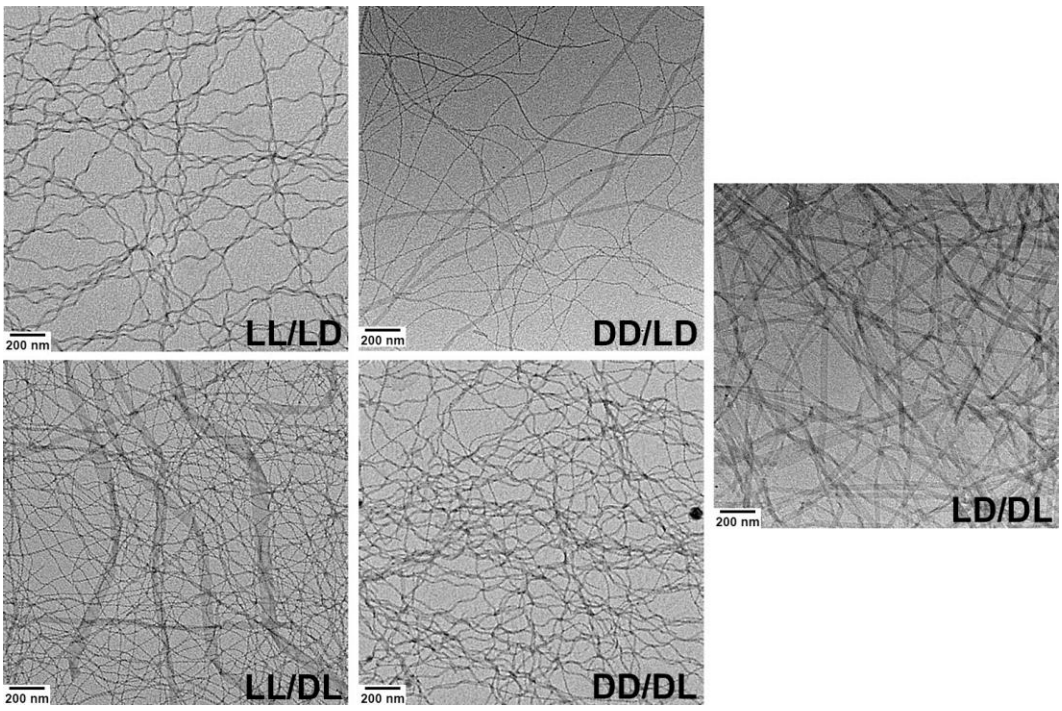

Figure 4.2. TEM micrographs of LL/LD, LL/DL, DD/LD, DD/DL, and LD/DL KFE8 analog pairs at 0.25 mM in DI water. Coassembly is visually evident for LL/LD and DD/DL, while LL/DL and DD/LD self-sort. The reduced tape diameter and loss of apparent helicity in LD/DL relative to its parent morphologies is sufficient to motivate complementary evaluations.

4.5 Spectroscopic Analysis

Additional support for these interpretations is provided by comparing pre- and post-mix CD data. By overlaying spectra from matching pre- and post-mixed pairs, along with their individual components, we can compare samples that were given the opportunity to coassemble (pre-mixed) to independently assembled samples with no such coassembly window (post-mixed). As expected, this approach did not yield any insight into LL/DD and LD/DL, as their spectra are identical in shape but inverted in sign, causing their mixtures to produce near-zero molar ellipticity (Θ) regardless of whether they reflect multiple populations. The coassembling pairs, LL/LD and DD/DL, generate disparate spectra between their pre- and post-mixed samples (*Figure 4.3A,D*). In contrast, the self-sorting pairs (LL/DL and DD/LD) have nearly identical spectra whether mixed pre- or post-assembly (*Figure 4.3B,C*). Further, spectra from self-sorting pairs all have local maximum Θ-values of roughly $\pm 4\text{-}5\times10^5$ in the random-coil range near ~195 nm. It would be reasonable to expect that self-sorting systems, whose component peptides generate spectra of opposite sign, would undergo destructive interference in this region. While this is the case for post-mixed LL+LD and DD+DL, which only reach molar ellipticities of $\pm 2\times10^5$, pre-mixing the same pairs to permit coassembly produces maximum Θ-values of over $\pm 7\times10^5$ in this same range. The deviation of the post-mixed pairs LL+LD and DD+DL from their pre-mixed solutions (LL/LD, DD/DL) serves as preliminary spectroscopic evidence of their coassembly. This support is bolstered by the virtually indistinguishable spectra generated by post-mixed (LL+DL, DD+LD) and pre-mixed (LL/DL, DD/LD) self-sorting pairs, which additionally confirms that the post-mixing process performed 30 seconds prior to experimentation has no deleterious effects on block chiral KFE8 suprastructures. FTIR data verifies antiparallel β-sheet secondary structure, with all samples producing major amide I stretches near 1625 cm^{-1} and 1695 cm^{-1} (*Figure 4.4*).

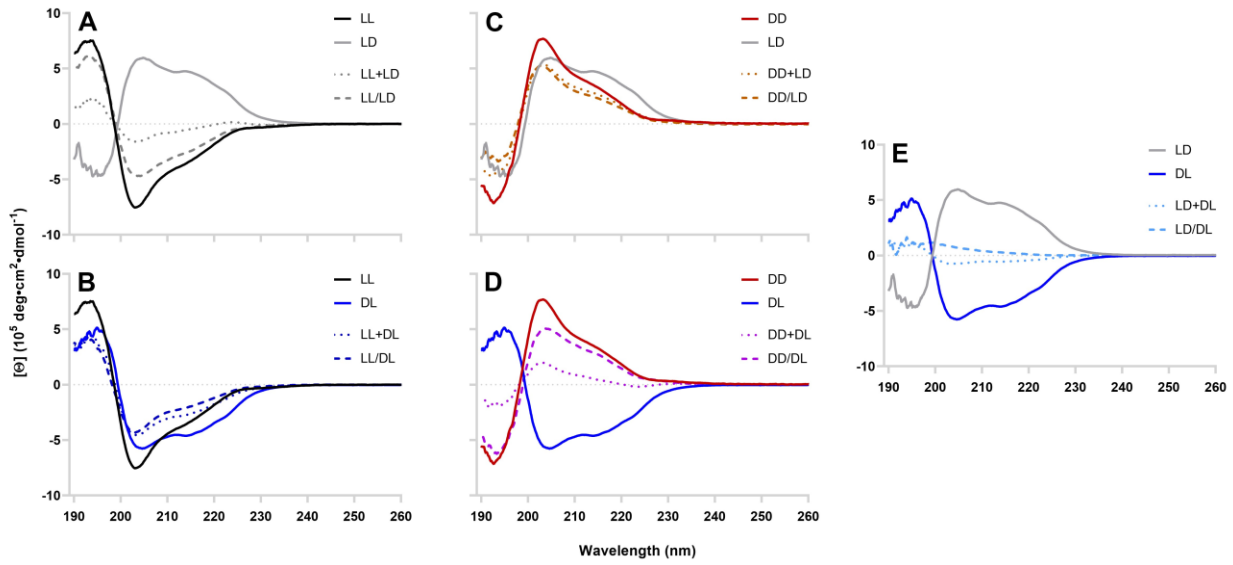

Figure 4.3. Circular dichroism (CD) spectra for the pre-mixed (dashed) KFE8 analog pairs (A) LL/LD, (B) LL/DL, (C) DD/LD, (D) DD/DL, and (E) LD/DL, alongside with their respective post-mixed formulations (dotted, no coassembly window). All spectra were obtained at 0.25 mM in DI water. Pure analog spectra (solid) are also provided for reference (*Chapter 2*). The pairs shown in panels (A) and (D) coassemble, as supported by pre-/post-mixed spectral discrepancies, as well as the lack of such discrepancies in the self-sorting samples in (B) and (C).

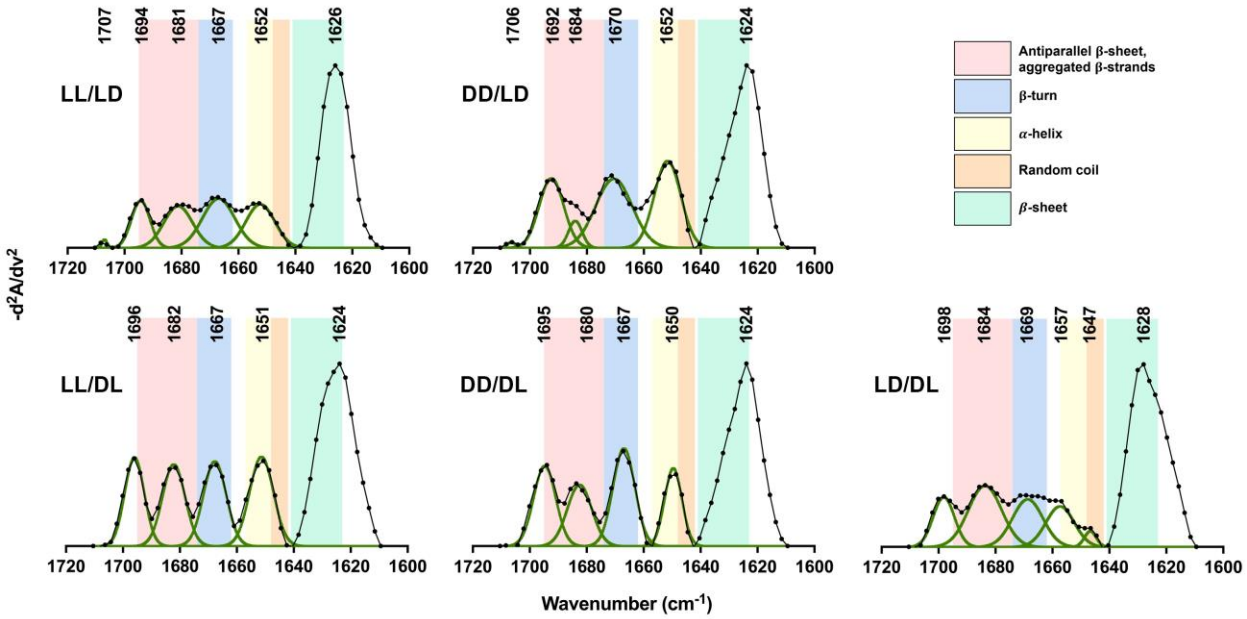

Figure 4.4. Second-derivative FTIR spectra and deconvolutions for the pre-mixed diblock chiral KFE8 pairs. Collected and processed data shown in black, Gaussian components shown in green.

TEM and CD data strongly support the diverging pairwise behaviors of coassembling pairs (LL/LD, DD/DL) and self-sorting pairs (LL/DL, DD/LD). This evidence led us to perform confirmatory studies, one of which implicated heavy-isotope tagging of phenylalanines for use in isotope-edited IR (IE-IR). Specifically, ^{13}C- and ^{15}N-labeled phenylalanine (L-Phe-$^{13}C_9$,$^{15}N_1$) was substituted for F5 (FKFE[F*]KFE) to exploit the linear alignment of F5 residues in the one-residue-shifted cross-β morphology of LL. This alteration shifts the amide I stretches produced by heavy atoms to lower vibrational frequencies as seen in *Figure 4.5A*, where the amide I stretch of unlabeled LL (black) shifts from ~1620 cm^{-1} to ~1608 cm^{-1} when fully F5-labeled (LL*, red). As LL and LL* are identical in terms of assembly mode, they fully and randomly coassemble. This increases the average distance between LL* strands and thus reduces the coupling of their heavy isotopes, leading to a lesser shift to ~1614 cm^{-1} (LL*/LL, *Figure 4.5B*).

Unlike the cross-β peak in unlabeled LL, the amide I stretch of LD appears at ~1630 cm^{-1}, aligning with reported values for typical monolayer β-sheets (Sarroukh et al., 2013). By normalizing all spectra in *Figure 4.5A* according to their magnitude at 1608 cm^{-1}, corresponding to maximal LL* F5 coupling, we see that the heterochiral tape contribution at 1630 cm^{-1} appears to dominate in the self-sorting LL*/DL system, nearly to the point of obscuring the shifted LL* peak, which now appears as a shoulder centered at 1608 cm^{-1}. In contrast, the coassembling pair LL*/LD has a visible but less prominent heterochiral tape contribution relative to that of LL*, indicating that isomerically pure tapes are far less abundant in LL*/LD than in LL*/DL. As these samples were prepared with high mass (1 mg), an order of magnitude higher than for CD and TEM, it is highly likely that these samples were at or very near 1:1 and that these data accurately reflect the systems.

A convoluting factor in this analysis is the observation that the labeled-F5 peak shifts back to 1614 cm^{-1} in LL*/LL, but the same stretch in LL*/LD unexpectedly remains fully shifted to 1608 cm^{-1}

(*Figure 4.5B*). This initially appears contradictory given the clear difference between the IE-IR spectra of LL*/LD and LL*/DL, as well as the ample complementary evidence provided by TEM, CD, X-ray scattering (*Section 4.6*), and ratiometric rheology (*Section 4.7*). Taken together, these data raise the intriguing possibility that LL/LD coassembles into segregated bilayers, with each layer composed entirely of either LL or LD. In LL*/LD, this would result in the labeled F5 residues of LL* remaining aligned within their all-LL half of the bilayer, with the strong heterochiral tape contribution (as seen for LL*/DL) being muted as the conformation of LD strands accommodates their incorporation into an LL-like bilayer (SAXS, *Section 4.6*). Unlike the inherently random arrangement of LL* β-strands within LL*/LL fibrils, a segregated bilayer would not reduce the magnitude of this peak shift. Though this remains simply a proposed mode of assembly, both TEM and CD data support an LL-leaning coassembled architecture, as both techniques show minor resemblance of LL/LD to LD but skew heavily toward LL in terms of visual morphology, CD signature, and CD sign, along with the LL-like bilayered LL/LD structure observed by X-ray scattering (*Figure 4.7*).

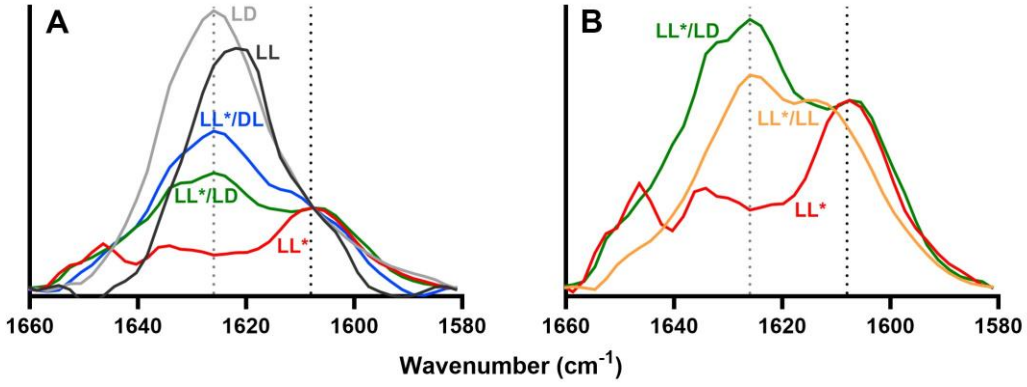

Figure 4.5. Isotope-edited infrared (IE-IR) spectroscopy. LL* refers to LL KFE8 labeled with the heavy isotopes ^{13}C and ^{15}N at its F5 residue. Pure LL* (red) results in a shift of its amide I stretch at 1630 cm^{-1} to 1608 cm^{-1}. All spectra are normalized by their magnitude at 1608 cm^{-1} for ease of comparison, with the exception of LL*/LL, which is scaled to its corresponding local maximum at 1614 cm^{-1}.

4.6 Small-Angle X-Ray Scattering

The small-angle X-ray scattering (SAXS) data for the six diblock chiral KFE8 pairs are grossly similar, with minor deviations at low s-values that may reflect slight differences in concentration or gelation conditions (*Figure 4.6A*). Fibril thickness (T_{plate}) of ~27 Å is consistent across all mixtures, ranging from 26 to 30 Å (*Table 4.1*). This attribute can also be examined using the cosine inverse Fourier transform, as shown in *Figure 4.6B*, with these alternative calculations supporting those from *Figure 4.6A* (Hansen, 2012; Larsen & Pedersen, 2021). Due to high-molarity gel formation, the standard R_g and D_{max} values, which are characteristics of single particles in a dilute non-interacting solution, are not well defined. R_{rod} values roughly match the radius of the KFE8 model (Hwang et al., 2003).

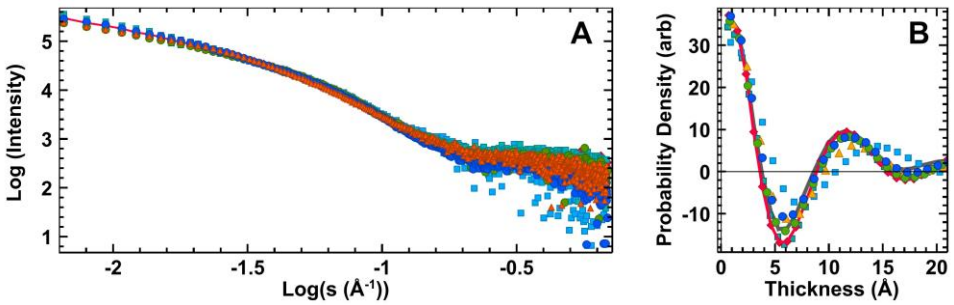

Figure 4.6. (A) SAXS Log-Log plots of the six diblock chiral KFE8 pairs LL/DD ◆, LL/LD ●, LL/DL ●, DD/LD ■, DD/DL ■, and LD/DL ▲. (B) Plate probability distribution (thickness 30 Å). The peak at ~12 Å corresponds to inter-β-sheet distances across the bilayer. Probability density for LL KFE8 (—) shown for comparison.

The Guinier plate thickness ($T_{plate}=\sqrt{12}\bullet R_{plate}$) is largely consistent across all isomer pairs, with their average of ~27 Å (*Table 4.1*, *Figure 4.7A*) in agreement with the β-sheet bilayer thickness of 2-start KFE8 helical fibril models. Deviations in Debye-Bueche heterogeneity factors are observed between groups but generally remain near the overall average of ~23 Å (*Figure 4.7B*), suggesting that the mixtures all have relatively similar network characteristics. That said, R_{rod} values for the coassembling pairs LL/LD and DD/DL are identical (20.*, 20.0 Å) and lower than all other pairs,

while their heterogeneity factors (21.3, 20.4 Å) are similarly analogous and significantly lower than the average for all groups (*Table 4.1*). These observations indicate that while all KFE8 pairs share a general atomic-level structure, coassembling and self-sorting pairs show slight but significant differences in several key metrics.

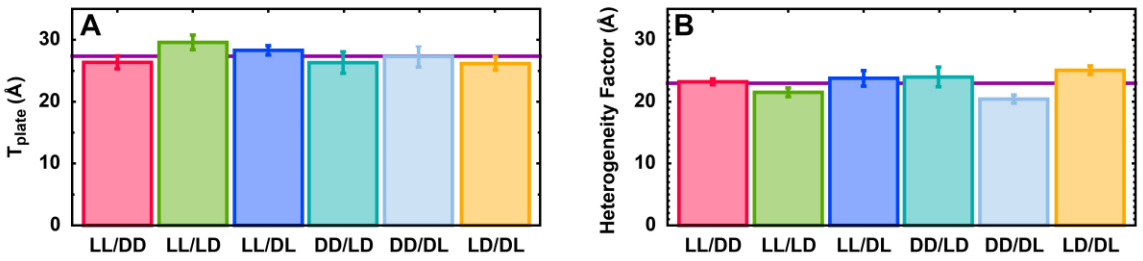

Figure 4.7. (A) The Guinier plate thickness (Å) for the six diblock chiral KFE8 pairs, with an average of 27.4 Å (purple line). (B) The Debye-Bueche heterogeneity factors (Å) for the pairs, with an average of 23 Å (purple line).

Table 4.1. SAXS characteristics of the diblock chiral KFE8 pairs.

Sample	R_g (Å)	D_{max} (Å)	Filament R_{rod} (Å)	Thickness T_{plate} (Å)	Debye-Bueche (Å)
LL/DD	146+	316+	23.*	26	23.2(1)
LL/LD	136+	287+	20.*	30	21.3(2)
LL/DL	138+	292+	23.*	28	23.8(3)
DD/LD	141+	317+	21.*	26	24.0(3)
DD/DL	130+	317+	20.0	27	20.4(1)
LD/DL	132+	256+	27.*	26	25.1(1)

*Curves not linear/value not well-defined

Table lists the Guinier radius of gyration (R_g), maximum dimension D_{max}, filament Guinier cross-sectional radius (R_{rod}), Guinier plate thickness ($T_{plate}=\sqrt{12}\bullet R_t$), and Debye-Bueche heterogeneity factor for each KFE8 pair.

4.7 Rheology

As fibrillar assemblies entangle into hydrogels at high concentrations, 10 mM formulations of the block chiral KFE8 isomer pairs were analyzed using an HR-20 rheometer fitted with a 20-mm smooth parallel-plate geometry. Two independently prepared replicates of each sample were

evaluated and, unless specified otherwise, analog ratios are 1:1 and all sweeps were performed at 0.1 Hz, 1% oscillatory strain with a gap height of 500 μm.

During strain sweeps, raw phase remain low for oscillatory strain levels between 0.1% and 100% (*Figure 4.8*). Crossover points, where gels transition from primarily elastic to viscous behavior, were found to be between 1.6%–2.6% for LL/DD, 1.0%–1.6% for LD/DL, 1.0%–1.6% for LL/LD, 1.0%–1.6% for LL/DL, 2.6%–4.0% for DD/LD, and 1.0%–1.6% for DD/DL. The linear region, or the strain regime in which phase angle remains approximately constant, was determined for all gels and is reflected by the tangent of the phase angle, tan(δ). This region consists of strains below ~0.64% for LL/DD, ~0.64% for LD/DL, ~1.03% for LL/LD, ~0.40% for LL/DL, ~0.64% for DD/LD and ~0.40% for DD/DL.

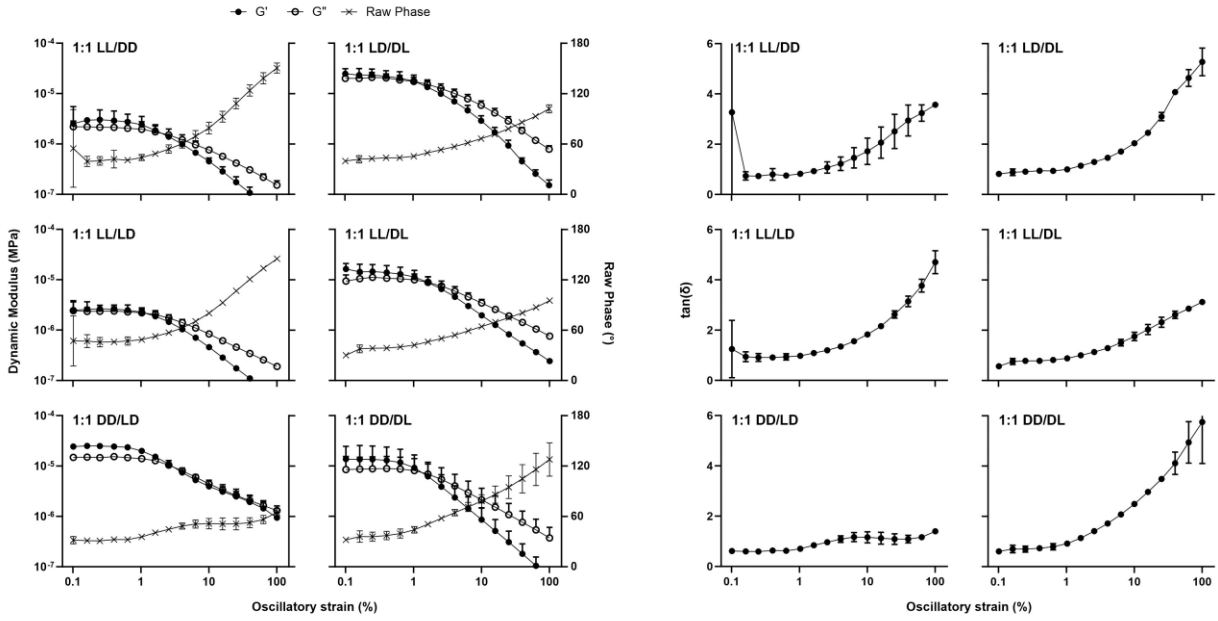

Figure 4.8. Strain sweeps for hydrogels formed by 1:1 mixtures of block chiral KFE8 isomer pairs. In the figure on the left, the left y-axis depicts dynamic modulus (MPa) and the right y-axis depicts raw phase (°). Raw phase is well below 180° at all strains shown, indicating instrument momentum is not a dominant factor and thus that data is valid in this range. All gels have G′>G″ at low oscillatory strains, indicating that they are viscoelastically solid before transitioning to viscoelastic liquids (G″>G′) at their respective crossover points. The figure on the right illustrates the linear regime during strain sweeps in terms of the tangent of the phase angle δ.

The storage and loss moduli at low strain are similar for the two self-sorting mixtures (DD/LD and LL/DL); however, moduli differences are observed between the coassembling mixtures LL/LD and DD/DL (*Figure 4.8*). This result motivated the study of asymmetric molar ratios to elucidate the collective impact of morphological heterogeneity on KFE hydrogel properties. Strain sweeps for 3:1 and 1:3 homochiral/heterochiral mixtures were performed using the procedure for 1:1 mixtures, as described above (*Figure 4.9*). Crossover points are observed at ~2.6% strain for 3:1 LL/LD, 1.0%–1.6% for 1:3 LL/LD, ~2.6% for 3:1 LL/DL, and 0.6%–1.0% for 1:3 LL/DL. Linear phases were found to be below ~1.0% strain for 3:1 LL/LD, ~0.6% for 1:3 LL/LD, ~1.6% for 3:1 LL/DL, and ~1.6% for 1:3 LL/DL.

3:1 and 1:3 mixtures inherently contain multiple morphologies regardless of the coassembly or self-sorting preferences of a given pair. 3:1 and 1:3 self-sorting mixtures segregate their homochiral and heterochiral monomers into isomerically pure fibrils and tapes at the same ratios. While this is true in terms of monomers, it is worth noting that due to the massive dimensions of LD or DL tapes, these structures are greatly outnumbered by the narrower LL or DD fibrils even in equimolar solutions. In principle, 3:1 coassembly-competent mixtures result in 50% coassemblies and 50% homochiral fibrils, whereas 1:3 mixtures produce 50% coassemblies and 50% heterochiral tapes.

Compared to 3:1 mixtures, the increased proportion of heterochiral peptide in 1:3 mixtures significantly affects low-strain dynamic moduli in both the coassembling LL/LD and the self-sorting LL/DL formulations. However, this has inverse effects on hydrogels formed by self-sorting versus coassembling isomer pairs (*Figure 4.9*). For the self-sorting pair LL/DL, increasing the fraction of DL tapes (1:3 mixtures) leads to a loss of dynamic modulus, as expected given the lower stiffness observed for pure heterochiral tapes relative to pure homochiral fibrils (*Figure*

2.13). As these analogs self-sort, the rule of mixing may be applied and broadly tracks with the observed trend that low-strain dynamic moduli decrease as the fraction of heterochiral peptide increases. By contrast, increasing the proportion of LD monomers in the coassembling LL/LD system from 25% to 75% (in 3:1 to 1:3 mixtures, respectively) instead enhances hydrogel stiffness by nearly an order of magnitude. Without the implications of coassembly, this result would directly contradict that for LL/DL. If coassembly is maximally efficient, then both 3:1 and 1:3 LL/LD mixtures will contain 50% coassembled peptide, with the remaining 50% of peptide adopting the morphology of the dominant analog. As 3:1 and 1:3 LL/LD hydrogels would thus differ only in the rheological strength of its isomerically pure suprastructure population, and it should naturally follow that the homochiral fibrils in 3:1 samples enhance hydrogel stiffness relative to the weaker mechanical contribution from LD tapes in 1:3 LL/LD samples. However, unlike LL/DL, the rule of mixing does not appear to apply to LL/LD samples, indicating that coassembly-tape interactions enhance gel mechanics in a way that cannot be described as simply cumulative influence from its coassembled structures and pure-LD tapes.

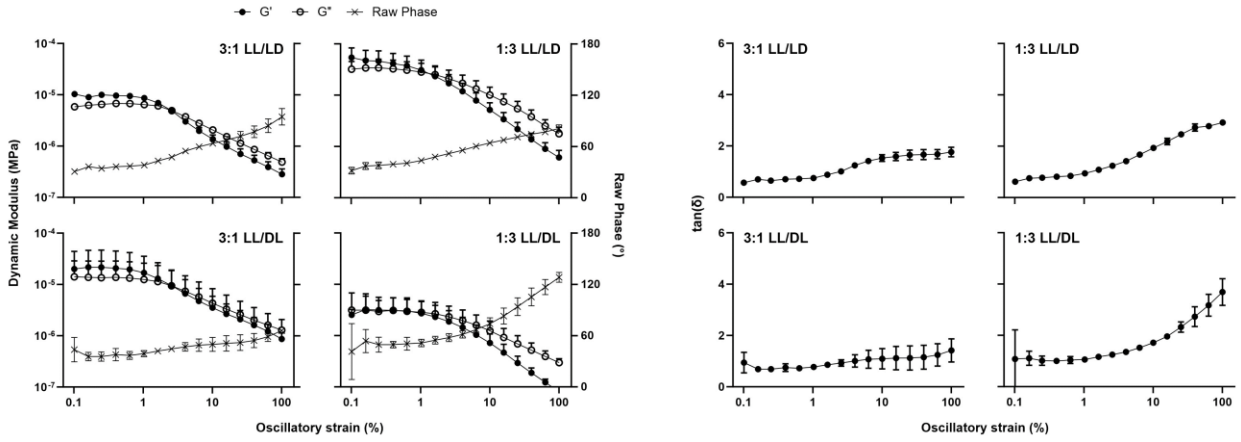

Figure 4.9. Strain sweeps for hydrogels formed by 3:1 or 1:3 ratios of the coassembling KFE8 pair LL/LD or the self-sorting pair LL/DL. In the figure on the left, dynamic modulus (MPa) is shown on the left y-axis and raw phase (°) on the right y-axis. The raw phase is well below 180° at all displayed points, indicating the data is valid. Coassembled LL/LD gels appears to be strengthened by replacement of its LL fibril population with LD tapes, despite the weaker rheological strength of the latter. In contrast, self-sorted LL/DL hydrogels are substantially weakened by the same alteration. In the figure on the right, linear regimes are described by the tangent of their phase angle δ.

4.8 Conclusions

Chirality has proven to be a versatile instrument for the creation of biomaterials with unconventional structure at the molecular and supramolecular scales. As illustrated by enantiomeric coassembly and the unique packing modes of di- and triblock heterochiral peptides (*Chapters 2,3*), the steric complexities introduced by interacting L- and D-domains are evidenced by the range of structural properties achievable through chiral modulation of a singular chemistry. In this work, we have shown that this range can be exponentially expanded by concerted application of these two concepts. Exploration of all possible combinations of homochiral or block heterochiral KFE8 has revealed that, like the racemic pairs LL/DD and LD/DL, coassembly is also achieved by the analog pairs LL/LD and DD/DL despite their nonenantiomeric status. Rather than evidencing unconditional assembly, the mutual incompatibility exhibited by the self-sorting pairs LL/DL and DD/LD signifies highly selective interactions contingent on the relative chiral patterns of a given isomer set. The fundamental differences between these seemingly closely related systems are supported by simple microscopic observation, deviation or agreement of pre- and post-mixed spectral signatures, varying component-wise IR contributions in an isotope-edited investigatory system, incongruous X-ray scattering, and inverted gel stiffness effects with increasing heterochiral component proportions. Taken together, these data serve as support for this intriguing instance of coassembly while also demonstrating the sweeping impact of block heterochirality from angstrom-scale packing mode deviations to macroscale materials properties.

Chapter 5: Immunomodulatory Effects of Block Chiral Peptidic Systems

5.1 Abstract

Relative to live-attenuated or inactivated vaccines currently approved for human use, which are often limited by their deleterious side effects, subunit vaccines exhibit improved safety profiles but require exogenous adjuvants to elicit the level of immune response necessary for anamnestic memory. Supramolecular peptide-based biomaterials possess intrinsic self-adjuvancy, eliminating the need for co-administration of reactogenic compounds such as alum. Reminiscent of viral surfaces, the repetitive nature of self-assembling systems facilitates rapid recognition of conjugated epitopes by antigen-presenting cells (APCs) and amplifies adaptive immune responses. In homochiral self-assembling systems, complete substitution with D-chiral residues inhibits proteolytic degradation while enhancing immunogenicity. This work investigates the effects of partial substitution, in particular segmented or 'block' heterochirality, on antibody and cellular immune responses using the model antigen $OVA_{323-339}$ in a C57BL/6 mouse model.

5.2 Introduction

In the last decade, vaccine design based on natural and synthetic biomaterials has rapidly grown into a promising advancement in the field of immunoengineering (O'Neill et al., 2021). The rich chemistries available for modification of peptide-, peptidomimetic-, and protein-based scaffolds enables vaccine systems to be engineered with control over antigen loading, degradability,

spatiotemporal release of immune signals, and targeted delivery to APCs (Green, 2021). This approach continues to generate new avenues for the development of subunit vaccines against infectious diseases, cancer, and autoimmune disorders. Notably, strategies based on PLGA micro- or nanoparticles, multi-lamellar vesicles, hydrogels, pluronic micelles, multilayer thin films, and self-assembling peptides have shown considerable success in preclinical disease models (Yousefpour et al., 2023).

This investigation focuses on the development of vaccines based on self-assembling peptides that form β-sheet-rich nanofibers and hydrogels in physiological buffers. Rudra et al. first reported that such nanofibers are immunologically inert but possess unique self-adjuvanting properties (Rudra et al., 2010). When fibrils comprised of antigen-conjugated peptides are injected into mice, a robust antibody response is induced against the antigen while the peptidic structural components remain immunologically inert. This potent adjuvancy is not limited by the primary sequence of the peptide but is dependent on its ability to produce fibrils with high aspect ratios (Rudra, Sun, et al., 2012). Further, high concentrations of self-assembling peptides form self-supporting hydrogels that can serve as depots for immunogenic excipients such as toll-like receptor (TLR) agonists, antibodies, cytokines, and other small molecules for applications in vaccine and immunotherapy (Grenfell et al., 2015). The chemical versatility of peptides permits sequence modifications that can be used to tune scaffold degradation and thus spatiotemporal release of immunomodulators (Appavu et al., 2015). The synthetic nature of self-assembling peptides additionally allows for high purity yields, minimal contamination, and biophysical and biochemical validation of the final construct, all of which represent significant advantages over emulsion adjuvants in terms of evaluation and approval by regulatory agencies.

Natural amino acids serve as a diverse biochemical toolbox for generating peptides that fold into secondary structures, such as β-sheets, that propagate into higher-order nanomaterials. Further, multiple studies have demonstrated enhanced proteolytic resistivity of fibrils composed of D-chiral peptides relative to their 'natural' all-L forms (Giano et al., 2011; Swanekamp et al., 2014). We have previously reported that fully substituting L-amino acids in the self-assembling peptide KFE8 (FKFEFKFE) with their protease-resistant D-enantiomers (fkfefkfe) significantly enhances the antibody response to conjugated antigens without altering nanofiber formation aside from supramolecular handedness (Appavu et al., 2015). This effect has also been confirmed using entirely different peptide classes, indicating that chirality can be used as a design tool to modulate the immunogenicity of self-assembling peptide biomaterials (C. Yang et al., 2018).

Beyond full D-substitution, racemic mixtures of L- and D-peptides yield a single 'coassembled' architecture with altered form and function (Nagy et al., 2011; Pauling & Corey, 1953; Swanekamp et al., 2012). Independent of primary sequence, such coassemblies have been found to possess unique thermodynamic and viscoelastic properties compared to their single-enantiomer counterparts (Nagy et al., 2011). When a peptide contains consecutive repeat motifs, such as KFE8 or KFE12 (two or three FKFE repeat units, respectively), we have shown that blocked chirality patterns significantly impact peptide self-assembly, morphology, and hydrogel mechanics (*Chapters 2,3*). In addition to pure enantiomers, we have demonstrated that 'pre-mixed' solutions containing both a homochiral and a block heterochiral analog conditionally coassemble or self-sort depending on their relative chiral patterns (*Chapter 4*). While these studies explored structural and rheological effects, the present work evaluates the immunological impact of patterned chirality in a C57BL/6 mouse model utilizing KFE8- and KFE12-based construct arrays with 10% of monomers conjugated to the model antigenic peptide $OVA_{323-339}$ (ISQAVHAAHAEINEAGR).

5.3 Methods

Peptide Synthesis. All peptides were purchased from P3 BioSystems (Louisville, KY) or GenScript Biotech (Piscataway, NJ) for molecular, spectroscopy, *in vivo*, and *in vitro* studies. Antigen-tagged peptides were conjugated at the N-terminus. Aliquots were prepared at molar ratios of 9:1 unconjugated:conjugated peptide, frozen at -80°C, lyophilized, and stored at -20°C.

Scanning Transmission Electron Microscopy (STEM). Peptide solutions were solubilized at either 0.10 mM (KFE12) or 0.25 mM (KFE8 and KFE8 pairs) in DI water. Ted Pella (Redding, CA) 200-mesh, formvar-free, pure-carbon-coated grids were glow-discharged and negative stained with 7.5% uranyl formate (UF) prepared as described in *Section 3.3*.

Circular Dichroism (CD). Circular dichroism spectra of the 10%-$OVA_{323-339}$-conjugated KFE systems were obtained on a Jasco (Hachioji-shi, Japan) J-815 CD spectrometer using a Hellma (Plainview, NY) quartz cuvette (110-1-40) with 1-mm path length at a scanning speed of 50 nm/min, a 0.1-nm data pitch, 1.00-nm bandwidth, and 100-mdeg sensitivity. Spectra are averages of three accumulations acquired from 300 to 190 nm for each sample. To verify data quality, absorbance and high-tension voltage (HT[V]) were also collected.

Dose Preparation. Vaccination and cell treatment aliquots were prepared by massing $OVA_{323-339}$-conjugated and unconjugated analogs on a Sartorius (Göttingen, Germany) Quintex 65-1S semi-micro analytical balance, solubilizing in 1:1 acetonitrile (ACN)/ultrapure water (UPW), and mixing at a 9:1 ratio of unconjugated:conjugated peptide. Aliquots were frozen at -80°C for 24 hours, lyophilized for 48 hours, and stored as dry powders at -20°C. The two individual components of 'post-mixed' samples (*Chapter 4*) were each prepared at the same 9:1 unconjugated:conjugated ratio and lyophilized independently.

Cytotoxicity Assays. Unlike KFE8, KFE12 has not previously been evaluated *in vitro* or *in vivo*. To this end, all 10%-$OVA_{323-339}$-conjugated KFE12 formulations were evaluated in cultures of the mouse dendritic cell line JAWS II. Briefly, cells were plated at a density of 3.7×10^4 per well (n=4) in a 96-well plate and treated with the conjugated KFE12 constructs (100 μL, 1 mg/mL) for 24 hours before adding MTS reagent (3-(4,5-dimethylthiazol-2-yl)-5-(3-carboxymethoxyphenyl)-2-(4-sulfophenyl)-2H-tetrazolium). Cytotoxicity was evaluated via absorbance at 450 nm on a BioTek (Winooski, VT) Synergy HT microplate reader. Cell viability was normalized to untreated cells, with an additional control group treated by free OVA at the same molarity as test groups.

Immunizations. 24 hours prior to each immunization, the appropriate aliquots were thawed, solubilized and vortexed at 0.56 mM in UPW, and allowed to mature overnight at 4°C. One hour before injections, aliquots were diluted to 0.50 mM with 10× sterile, endotoxin-free phosphate-buffered saline (PBS, 1× final concentration). 'Post-mixed' samples were mixed 30 seconds before injection. Subcutaneous dorsal flank injections were performed on 4-to-6-week-old female C57BL/6 mice from Jackson Labs (Bar Harbor, ME), with the 100 μL applied to each of the two sites containing 10 nmol of $OVA_{323-339}$ either conjugated to KFE12 or free in 5 mg/mL alum. The PBS control group received injections of pure saline prepared in parallel with test group doses. All mice were boosted on day 21 with identical injections.

Sample collection. Mice were euthanized at day 56 via isoflurane overdose followed by cervical dislocation, according to AVMA guidelines. Sera were collected via cardiac puncture and spleens were harvested for cellular analysis. In all animal work, institutional guidelines for the care and use of laboratory animals were strictly followed under a protocol approved by the Institutional Animal Care and Use Committee at Washington University in St. Louis.

Determination of antibody titers and isotypes. High-binding ELISA plates from eBioscience (San Diego, CA) were coated with 10 μg/mL $OVA_{323-339}$ in PBS overnight at 4 °C. After 24 hours, wells were washed (300 μL PBST, 3x) and blocked with 1% BSA in PBST for one hour. Sera were centrifuged in microcapillaries at 10,000g for 10 minutes to remove hematocrit. Each serum sample was initially diluted 1:10 in PBST/BSA. The serum solutions were added to isotyping ELISA plates at 1:100, while total ELISA plates consisted of eight 1:5 serial dilutions beginning from 1:100. On all plates, sera-treated columns alternated with non-sera-treated control columns to facilitate direct comparison. After a 7-minute incubation and three washes, HRP-conjugated total ELISA secondary antibody solution (100 μL, 1:4000) were applied for one hour, while isotyping plates received either IgG1, IgG2b, IgG2c, IgG3, IgM, or IgE HRP-conjugated secondary antibodies (100 μL, 1:4000) for one hour. Following five washes, 100 μL TMB substrate was applied to wells for two minutes before stopping the reaction with 1 M phosphoric acid (50 μL). Absorbance values were read at 450 nm, with neighboring blank wells subtracted from raw values. For total ELISA, net absorbances were compared to cutoff values (mean + 3σ), above which wells were considered positive. The titer was considered as the highest positive dilution for which all lower dilutions were also positive. If no positive dilutions were present, the titer was considered as 10^1. Isotyping ELISA data were reported as net absorbance values.

Splenocyte isolation and challenge. Following euthanasia, spleens were harvested and splenocyte cultures were prepared according to published protocols (Rudra et al., 2010). Briefly, minced spleens of the immunized mice were passed through 70-μm cell strainers to obtain a single-cell suspension, after which isolated splenocytes were washed in complete RPMI medium containing 10% FBS (RPMI 1640 supplemented with 10% fetal bovine serum and 1× Pen/Strep). Red blood cells were lysed using ACK buffer (150 mM NH_4Cl, 10 mM $KHCO_3$, 0.1 mM EDTA) and washed

twice. Splenocytes (10^6/well) were stimulated *in vitro* with free $OVA_{323-339}$ (2 μg/ml) for five days in 96-well round-bottom plates. Supernatant was collected for cytokine analysis. Cells were stained with MBL Bio (Sunnyvale, CA) Zombie-NIR dye, followed by T-select I-A^b $OVA_{323-339}$ tetramer-PE (TS-M710-1), BioLegend (San Diego, CA) CD3-Pacific Blue (clone 17A2), and BioLegend CD4-FITC (clone RM4-5).

5.4 Electron Microscopy and Structural Analysis

The reliable self-assembly behaviors of block chiral KFE systems has been previously demonstrated for various diblock, triblock, and diblock pair systems (*Chapters 2–4*). The wide variety of morphologies adopted by these closely related peptides necessitates confirmation of their characteristic packing modes and supramolecular architecture when conjugated to the $OVA_{323-339}$ epitope. In this study, 10% of KFE monomers were tagged at their N-termini with the 17-amino acid model peptide antigen $OVA_{323-339}$. Despite the phenyl-zipper edge stitching between adjacent N-termini in all systems apart from LLL and DDD, no disruptions are apparent regardless of the highly variable width, laminarity, and helicity or twist between systems. Scanning transmission electron microscopy (STEM) was performed for one member of each enantiomer pair to verify that their mirrored but otherwise identical packing mode is preserved (*Figures 5.1, 5.2*). This validation includes LL and LD KFE8 (*Chapter 2*); pre-mixed LL/LD (coassembled) and post-mixed LL+LD (independently assembled) KFE8 pairs (*Chapter 4*); and LLL, LDL, LLD, and LDD KFE12 (*Chapter 3*). STEM data for pre-mixed LL/LD additionally confirms that the N-terminal tags did not impede coassembly, with post-mixed (independently assembled) LL+LD acting as a direct comparator with identical monomeric composition (*Figure 5.1*).

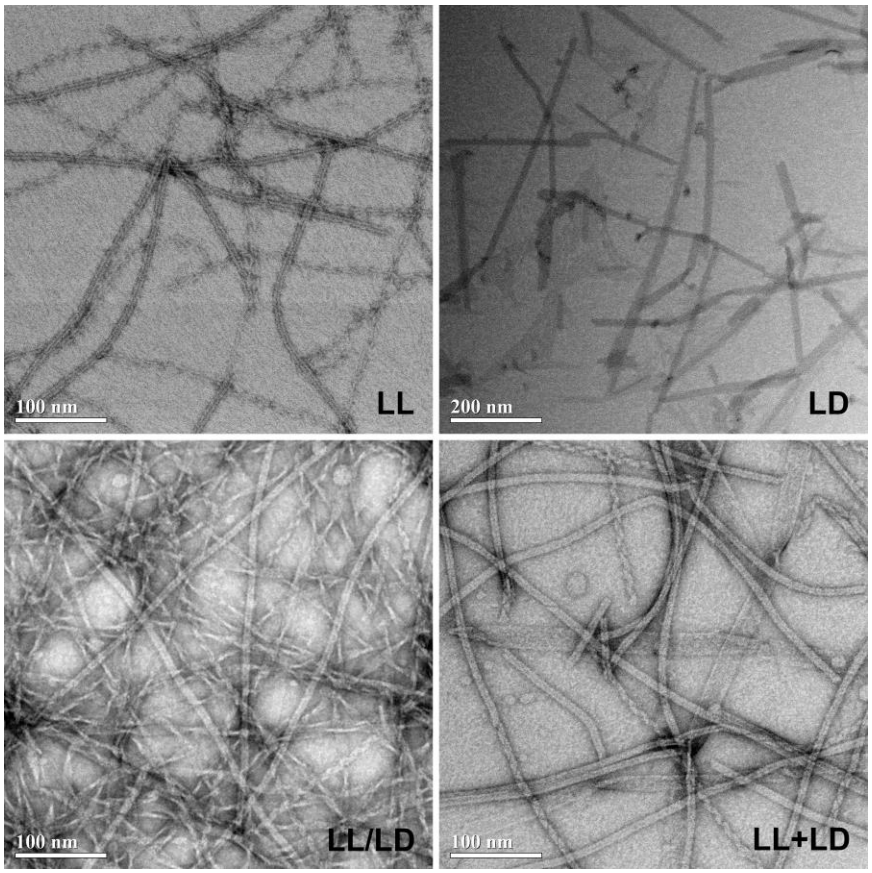

Figure 5.1. Scanning transmission electron microscopy (STEM) for the 10%-$OVA_{323-339}$-conjugated block chiral KFE8 systems evaluated as vaccine scaffolds *in vivo*. One member of each enantiomer pair is shown at 800k magnification. Due to the exceptionally large dimensions of diblock heterochiral KFE8, LD is shown at half-magnification (400k). Structure is maintained for all samples and coassembly (LL/LD) is not substantially affected despite a minor LL molar excess.

Interestingly, the strong scattering effect of disordered $OVA_{323-339}$ groups is visible as dark striations between adjacent β-sheet columns, with these N-terminal groups extending out into solvent above the long-range phenyl π-stacks serving as zippers between sheets. This effect is especially apparent in 10%-$OVA_{323-339}$-tagged LDL (*Figure 5.2*), illustrating the 3-to-5-peptide-width reported previously (*Section 3.4*). Additionally, the atypical assemblies of LDD roughly retain their gross morphology as non-fibrillar 2-D β-sheets, often found in massive, highly multilaminar 3-D structures. Like other $OVA_{323-339}$-tagged KFE systems, dark striations support that LDD has underlying columnar β-sheet nanoscale morphology despite its microscale

irregularity. Upon close inspection of well-resolved FOVs, bands of parallel striations that correspond to regular local structure seemingly flow into each other between and across multiple domains displaying orthogonal striations, potentially provided a visual representation of the complex LDD and DLL packing modes discussed in *Chapter 3*.

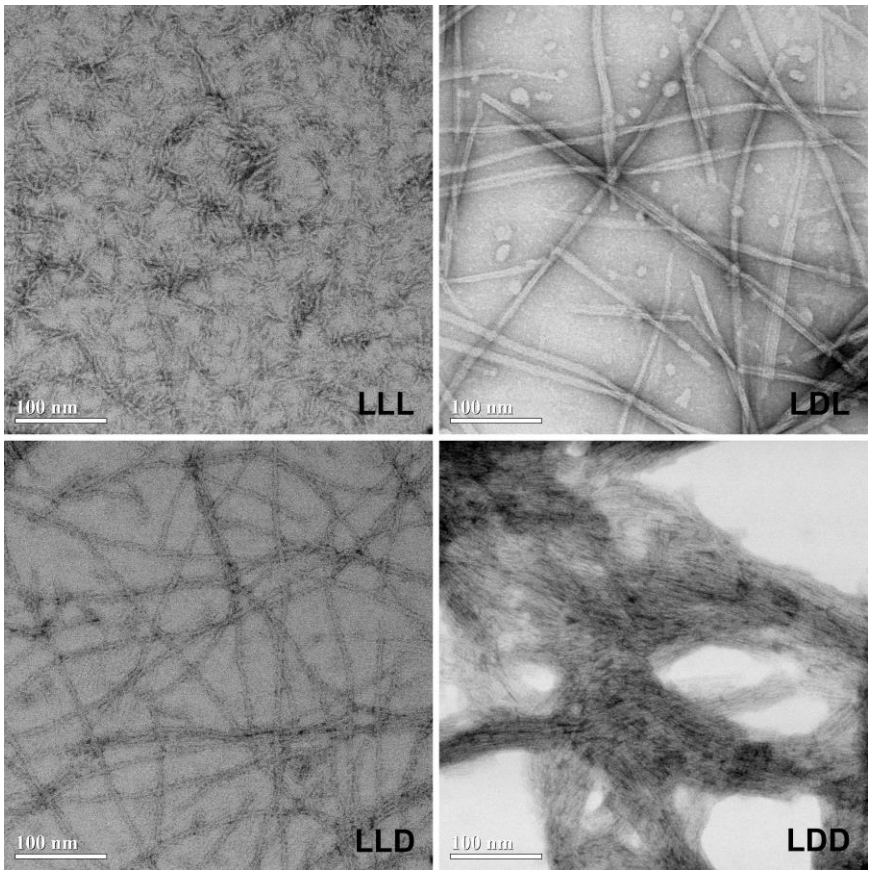

Figure 5.2. STEM micrographs for one member of each 10%-$OVA_{323-339}$-conjugated triblock chiral KFE12 enantiomer pair (800k magnification). No impact of epitope conjugation on structure is apparent apart from minor visual distortion due to electron scattering by epitopes across the multilaminar structure of LDD.

Circular dichroism (CD) was performed as additional verification that secondary structure is not substantially affected by N-terminally conjugating 10% of monomers with $OVA_{323-339}$. CD curves for the four KFE8 analogs (homochiral LL and DD; diblock heterochiral LD and DL) closely resemble those of their unconjugated forms, as did the pre-mixed coassembling KFE8 pairs (LL/LD and DD/DL) (*Figure 5.3*). Homochiral KFE12 (LLL and DDD) also retained the spectral

characteristics of their unconjugated forms, along with LDL and DLD (*Figure 5.4*). Though 10%-conjugated LLD and DDL appear slightly blue-shifted, their overall shape and unique zero-crossover at ~222 nm (n → π*) are both maintained. Due to their tendency to precipitate, material intended for circular dichroism was required to obtain sufficiently solubilized 10%-OVA$_{323-339}$-conjugated LDD and DLL vaccination doses.

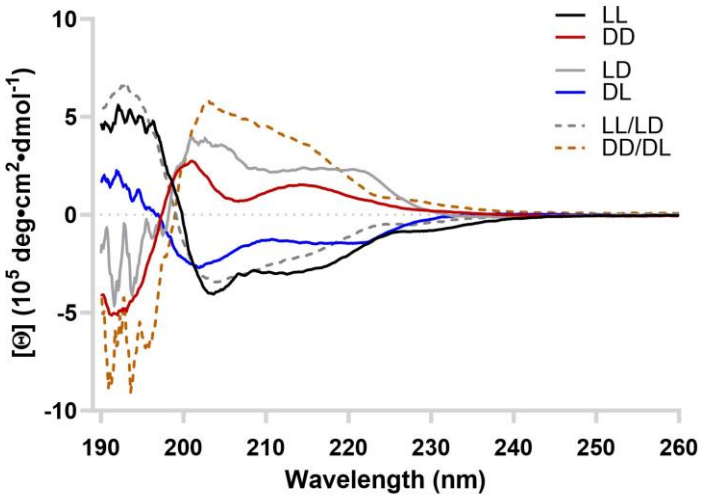

Figure 5.3. Circular dichroism (CD) spectra for 10%-OVA$_{323-339}$-conjugated homochiral (LL, DD), block heterochiral (LD, DL) KFE8 (*Chapter 2*), and their pre-mixed coassembling pairs LL/LD and DD/DL (*Chapter 4*). β-sheet character is evident for each system, all of which retain their sign and overall spectral shape.

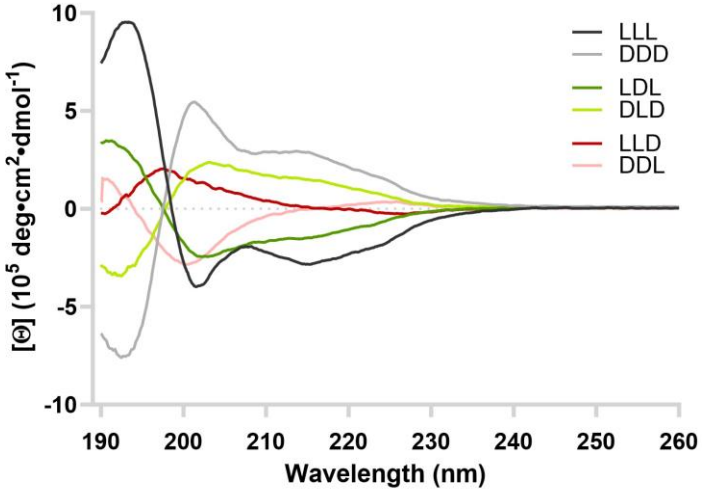

Figure 5.4. CD spectra for 10%-OVA$_{323-339}$-conjugated triblock chiral KFE12 analogs LLL, DDD, LDL, DLD, LLD, and DDL. All analogs exhibit β-sheet character and bear close resemblance to their unconjugated variants, with identical signs and minimal change to spectral shapes (*Chapter 3*).

5.5 Cytotoxicity Studies

MTS data indicated that the triblock KFE12 analogs were non-cytotoxic to primary murine dendritic cells. By eliminating this possibility, *in vivo* vaccination data (*Sections 5.6–5.7*) can be interpreted solely in terms of the ability of these scaffolds to adjuvant immune responses against conjugated antigen. *In vitro* data indicated robust cell growth over 24 hours following treatment with the KFE12 formulations when compared to untreated cells, confirming that their amphipathicity and heterochirality do not compromise cell membrane integrity and is not otherwise cytotoxic (*Figure 5.5*). As heterochiral self-assembling systems are a relatively new development with prospective applications as cell-culture matrices or implantable scaffolds for regenerative medicine, it is imperative to evaluate and understand any potential toxicity at the early stages of their design. Collectively, our data indicate that the strong cross-β character, stability, and non-cytotoxicity of block chiral KFE12 isomers support their status as excellent candidates not only as self-adjuvanting vaccines, but also as synthetic hydrogel biomaterials for cell culture.

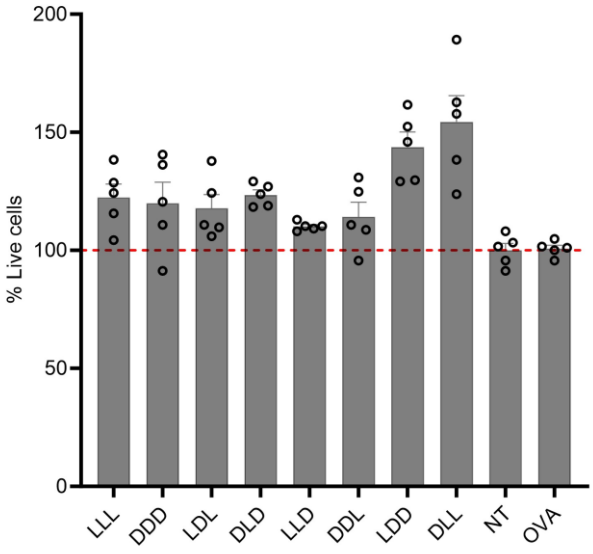

Figure 5.5. MTS analysis data showing non-toxicity of block heterochiral 10%-$OVA_{323-339}$-conjugated KFE12 assemblies. 'NT' refers to non-treated (PBS sham) cells, 'OVA' refers to cells treated with free $OVA_{323-339}$. Data shown as mean ± SEM.

5.6 Serum Antibody Titers and Isotyping

To assess the role of block heterochiral patterning on humoral immune responses, antibody titers collected eight weeks (d56) after initial immunizations were evaluated by ELISA as described previously (Appavu et al., 2015; Rudra et al., 2010). Sera from mice immunized with 10%-$OVA_{323-339}$-conjugated KFE8, KFE12, or pre- or post-mixed coassembling KFE8 pairs were applied to plates coated with free $OVA_{323-339}$ peptide to ensure specificity of the antibodies bound. Control wells did not receive serum dilutions but were otherwise identically prepared. Antibody profiles in mice vaccinated with individual or paired KFE8 analogs show that the adjuvancy of their parent peptide is preserved (*Figure 5.6*). While variation is observed between formulations, all titer means exceed those for groups treated with either PBS or $OVA_{323-339}$ co-administered with alum, the gold-standard clinical adjuvant. In contrast to a previous study in which mice were immunized three times with 100%-conjugated scaffolds (Appavu et al., 2015), LL and DD KFE8-adjuvanted groups produce nearly identical antibody titer means. $OVA_{323-339}$-bearing heterochiral KFE8 tapes (LD and DL) and pre-mixed coassembling KFE8 pairs (LL/LD and DD/DL) generate mean antibody titers that were roughly equivalent to the homochiral LL fibrils. No discernable differences were detected between the pre-mixed coassembling KFE8 pairs (LL/LD, DD/DL), nor between the post-mixed (independently assembled) coassembling KFE8 pairs (LL+LD, DD+DL).

KFE12 data indicates that vaccines scaffolded by each of the eight triblock chiral isomers are all self-adjuvanting, with most D-containing formulations eliciting mean titers higher than or roughly equal to those for mice treated with fibrils constructed from L-homochiral KFE12 (*Figure 5.6*). As expected, higher mean antibody titers were detected for groups receiving vaccines scaffolded by DDD compared to those scaffolded by LLL. Analogs with two chiral interfaces also induced antibody titers higher than (LDL) or approximately equivalent to (DLD) the homochiral LLL

construct. Titers collected from mice treated with $OVA_{323-339}$-LLD and $OVA_{323-339}$-DDL have nearly indistinguishable means from those elicited by $OVA_{323-339}$-LLL and $OVA_{323-339}$-DDD, respectively. Interestingly, heterochiral KFE12 analogs with an N-terminal opposing chiral domain (LDD and DLL), which form multilayered 2-D β-sheet aggregates (*Figure 5.2*), retain self-adjuvanting potential despite their highly unconventional morphology. Apart from analogs with dual chiral interfaces (LDL and DLD), all other KFE12 analogs with a D-chiral N-terminal block (DDD, DDL, DLL) generate substantially stronger antibody responses than their enantiomers (LLL, LLD, LDD). This observation, in combination with the demonstrated immunogenicity of both fibrillar and non-fibrillar KFE structures, suggests that morphology and chiral composition have a concerted impact on humoral immune responses, influencing uptake by APCs, trafficking to the lymph nodes, B-cell recognition, and *in vivo* modifications.

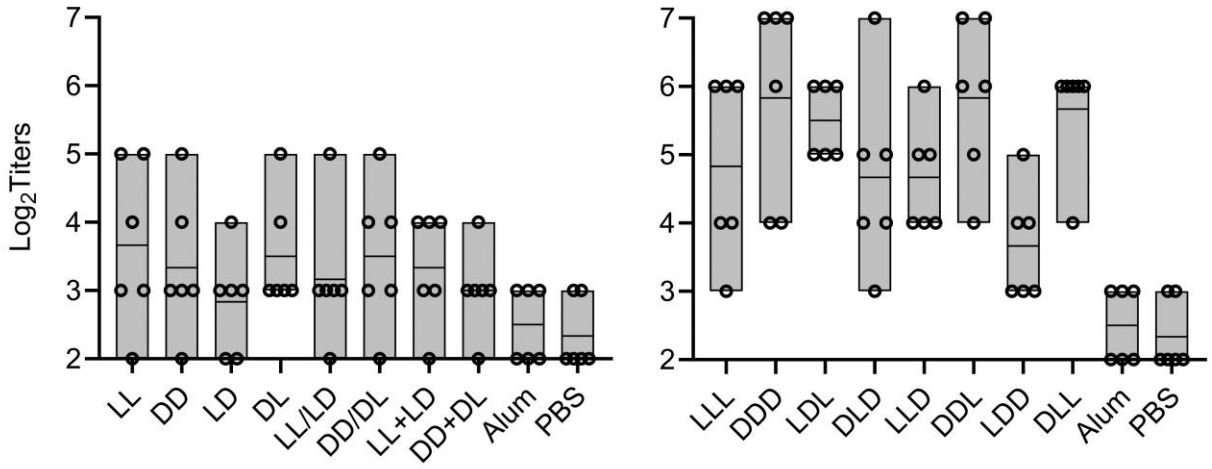

Figure 5.6. Total anti-$OVA_{323-339}$ titers detected in the serum of mice primed (d0) and boosted (d21) with 10%-$OVA_{323-339}$-conjugated block chiral KFE8, KFE12, or KFE8 isomer pairs; free $OVA_{323-339}$ emulsified with alum; or a PBS sham.

Collectively, these results offer preliminary guidance for the design of clinically relevant block chiral peptide biomaterials. In both diblock and triblock systems, homochiral D-peptides (DD and DDD) elicited higher antibody titers (IgG1 and TE, respectively) while homochiral L-peptides (LL

and LLL) elicited stronger T-cell responses. This trend agrees with our understanding of D-fibrils as mirrored but otherwise morphologically identical to their L-enantiomer, with the critical physiological difference lying in their susceptibility to degradation by inherently L-attuned proteases. Following vaccination, B cells recognize antigens directly via surface receptors, but cannot generate high-affinity antibodies without T-cell help. Unlike B cells, T cells respond only when dendritic cells present antigens in the context of major histocompatibility complex (MHC) molecules with costimulatory ligands and cytokines. Classically, internalized antigens are enzymatically processed in the endo-lysosomes of DCs and presented on MHC-II to $CD4^+$ T cells, whereas cytosolic antigens are degraded by the proteosome and presented on MHC-I to $CD8^+$ T cells. Thus, in models where protection is heavily antibody-dependent, inclusion of D-amino acids in vaccine scaffolds could benefit B-cell responses via antigen persistence. If robust $CD4^+$ or $CD8^+$ T-cell responses are desired, reducing D-amino acid composition would be conducive to facilitating proteolytic cleavage and presentation to T cells. These findings imply that, alongside chiral pattern-driven morphology, tuning L- and D-block proportions can be exploited to orchestrate B- and T-cell involvement and the subsequent adaptive immune response profile.

To determine the nature of the antibody response elicited by the KFE12 analogs, isotyping ELISA was performed to evaluate *in vivo* levels of IgG1, IgG2b, IgG2c, IgG3, IgM, and IgE eight weeks (d56) after primary immunization (*Figure 5.7*). All isotypes were evaluated by coating 96-well round-bottom plates with free $OVA_{323\text{-}339}$ peptide in parallel for all groups to enable direct comparison between groups and isotypes. The dominant isotype was IgG1 for all groups, as observed in prior studies using KFE systems and consistent with a T-helper type 2 (Th2)-type response. IgG2b and IgG2c were also detected in some cohorts, with chiral composition appearing weakly correlated to multiple individual isotypes. In all KFE groups, low levels of IgM were

present, as expected, while no appreciable levels of IgG3 or IgE were observed. These findings demonstrate that while heterochiral patterning significantly impacts molecular packing, morphology, and stability, the self-adjuvancy of supramolecular KFE scaffolds is preserved and can be exploited for the development of subunit vaccines with improved safety profiles.

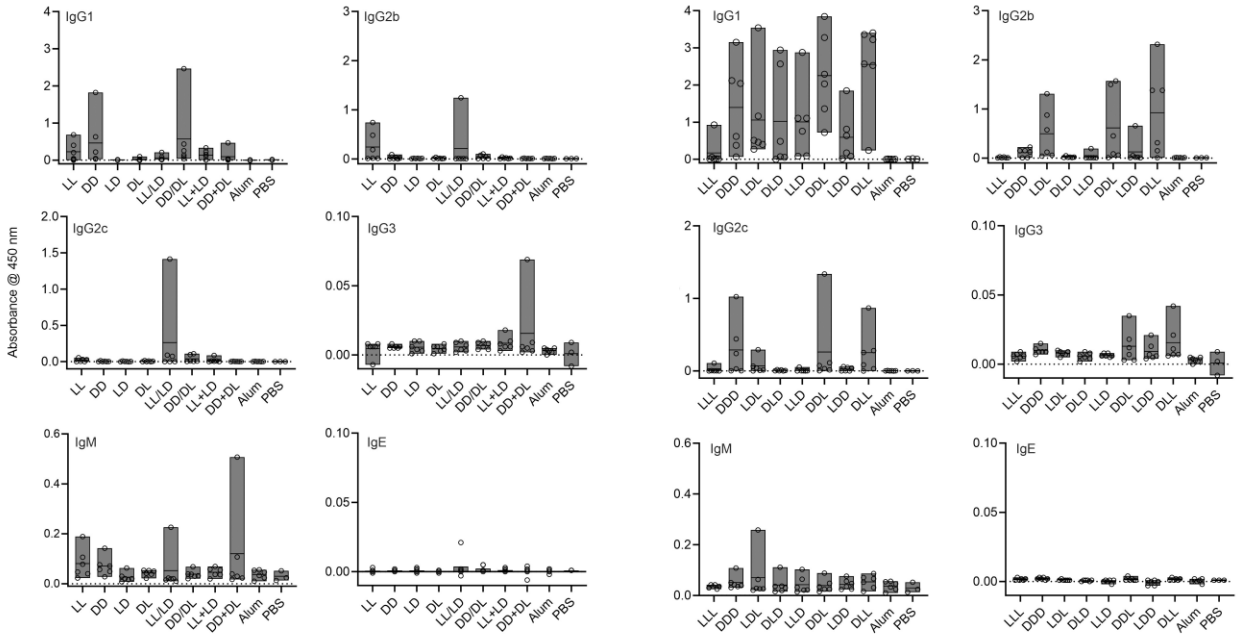

Figure 5.7. Serum antibody isotypes (IgG1, IgG2b, IgG2c, IgG3, IgM, IgE) raised against vaccine scaffolds composed of 10%-$OVA_{323-339}$-conjugated block chiral KFE8, KFE12, or KFE8 isomer pairs. Control groups included a PBS sham and free $OVA_{323-339}$ emulsified with alum.

5.7 Cellular Immune Responses

$OVA_{323-339}$ is a well-characterized $CD4^+$ T-helper epitope with an embedded B-cell determinant, with previous studies showing that antibody responses against $OVA_{323-339}$-bearing LL KFE8 fibrils are $CD4^+$ T cell-dependent (Rudra, Sun, et al., 2012). To assess the impact of diblock chirality patterns and isomer pair coassembly on cellular immune responses, mice were immunized with homochiral (LL or DD), diblock heterochiral (LD or DL), and coassembling (LL/LD or DD/DL)

formulations with 10% of monomers functionalized with $OVA_{323-339}$ at their N-termini. The coassembling formulations were administered as either 'pre-mixed' (LL/LD or DD/DL) or 'post-mixed' (LL+LD or DD+DL) forms to further delineate the effects of coassembly compared to simple mixing, with post-mixed samples being combined just 30 seconds before immunization to preserve both individual component morphologies. Collected data indicates that mice immunized with LL fibrils have the highest frequency of $OVA_{323-339}$-specific $CD4^+$ T cells compared to all other groups, including the cohort emulsified with the gold-standard clinical adjuvant alum. All mice treated with DD fibrils produced $OVA_{323-339}$-specific T-cell frequencies above the baseline established by sham (PBS) mice, but the average frequency was found to be lower than for groups adjuvanted by its enantiomer LL. This is in line with expected outcomes, as antigenic fibrils composed of natural L-amino acids are easily processed and presented via the MHC-II pathway compared to their proteolysis-resistant 'non-natural' D-chiral enantiomers. Immunizations implicating the heterochiral isomer LD or pre-mixed LL/LD coassemblies also resulted in generation of antigen-specific T cells, with a higher mean frequency than DD fibrils. Interestingly, heterochiral DL and pre-mixed DD/DL coassemblies induced lower levels of tetramer positive $CD4^+$ T cells compared to LD and pre-mixed LL/LD. Taken together, these data indicate that the proportion of D-amino acids in a given formulation influences the induced cellular immune responses, presumably due to significant differences in recognition, internalization, and enzymatic processing. It is feasible that while systems with higher D-amino acid proportions might produce lower levels of T cells, their intrinsic proteolytic resistivity may enable depot effects to persist for extended durations, prolonging T-cell responses. This could be reflected by the detection of $OVA_{323-339}$-specific T cells on day 56 for post-mixed DD+DL, at levels comparable to alum, but not for LL+LD.

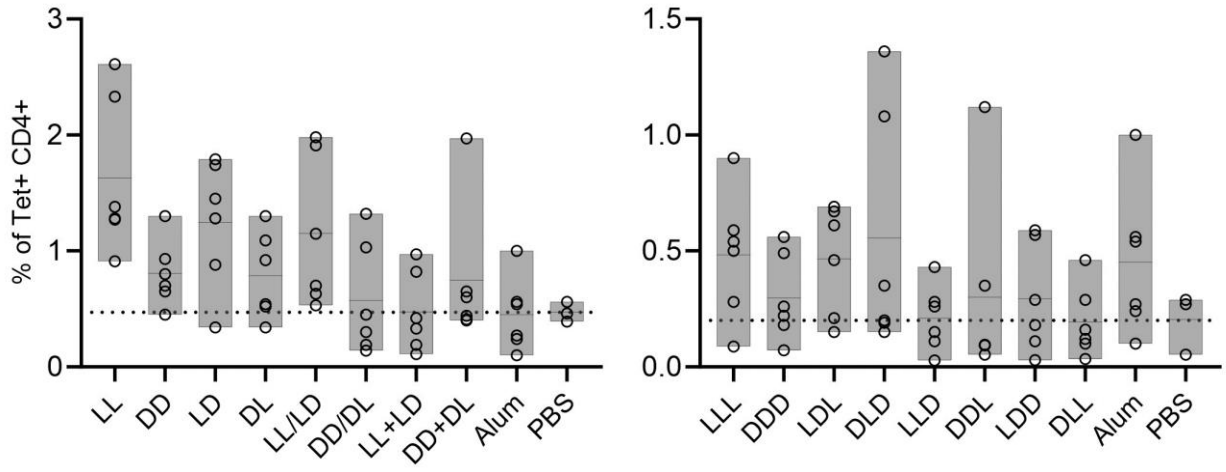

Figure 5.8. Cellular immune responses against (left) diblock chiral KFE8 isomers and their pre- or post-mixed pairs, and (right) triblock chiral KFE12 isomers. The percentage of $OVA_{323-339}$-specific T cells were measured following antigen recall using tetramer staining. 'Alum' refers to mice treated with free $OVA_{323-339}$ co-administered with the emulsifying adjuvant alum (5 mg/mL). 'PBS' refers to sham mice treated with 1× phosphate-buffered saline.

We next assessed the adjuvanting potential of heterochiral triblock KFE12 by measuring the frequency of $OVA_{323-339}$-specific $CD4^+$ T cells in vaccinated mice (*Figure 5.8*). Unlike the diblock homochiral systems, triblock homochiral KFE12 (LLL, DDD) adopt minimal cross-β fibrillar structures just one peptide in width. However, similar to LL and DD KFE8, $OVA_{323-339}$-bearing LLL assemblies (10% of monomers) induced higher levels of antigen-specific T cells compared to assemblies of its enantiomer DDD. The frequency of T cells in the LLL group was similar in magnitude to control mice vaccinated with free $OVA_{323-339}$ emulsified with alum. LDL and DLD fibrils also exhibited self-adjuvanting properties, with tetramer-positive T-cell frequencies comparable to LLL. As observed in the diblock systems, chiral composition of the analogs did not solely dictate cellular immune responses, but rather acted in tandem with morphology-driven effects. Despite containing a higher proportion of D-amino acids, DDL and LDD produced higher frequencies of $OVA_{323-339}$-specific T cells compared to their enantiomers. While future experiments will aim to delineate chiral and morphological contributions, this study represents the first report of self-adjuvanting vaccines scaffolded by block heterochiral supramolecular systems.

5.8 Conclusions

The biological implications of block heterochiral assemblies are inherently tied to their unique structural and morphological features; however, even the most divergent systems retain enhanced adjuvancy relative to alum, the 'gold-standard' FDA-approved adjuvant. To date, demonstrations of self-adjuvanting supramolecular immunomodulatory scaffolds have relied upon fibrillar architectures. Continuing conceptually along this line, this adjuvancy is retained across the full spectrum of fibrillar KFE assemblies, whether it be helical two-peptide-wide bilayers (LL, DD), tightly twisted one-peptide-wide bilayers (LLL, DDD), 20-to-50-peptide-wide monolayer tapes with micron-scale pitch (LD, DL), or intermediate-width twisted (LDL, DLD) or flat (LLD, DDL) bilayer morphologies. This remains true for multi-component systems, with both coassembled (LL/LD, DD/DL) and independently assembled (LL+LD, DD+DL) formulations producing antibody titers and T-cell responses comparable to those of their individual components. While the unique packing mode and highly atypical dimensions of LD and DL (*Figure 5.1*) place them near the end of the 'fibril' spectrum, LDD and DLL are decidedly non-fibrillar (*Figure 5.2*) yet their semi-ordered assemblies elicit analogous immune responses. As such, the array of KFE variants chosen as vaccine scaffolds comprehensively validates the adjuvanting potential of fibrillar cross-β scaffolds across a remarkable range of size and helicity or twist, while the LDD and DLL constructs serve as the first demonstration of self-adjuvanting behavior in non-fibrillar self-assembling scaffolds. The clear adjuvancy exhibited by the full array of discrepant KFE morphologies, along with the inherently unconventional recognition and processing of heterochiral suprastructures by APCs, illustrates that a surprisingly wide diversity of architectures can be exploited as efficacious immunogenic vaccine scaffolds.

Chapter 6: Summary and Future Directions

This dissertation represents a cohesive exploration of block heterochirality as a complementary means of generating novel supramolecular systems *de novo*. Using an array of variants derived from the model peptide KFE8, we have demonstrated the diverse effects of diblock and triblock heterochirality, as well as the selective stereocomplexation of block-isomeric but chemically identical species.

In *Chapter 2*, we describe the comprehensive departure of diblock heterochiral (LD, DL) KFE8 from its characteristic homochiral (LL, DD) bilayer. In the first application of this modification strategy, simply inverting the chirality of one repeat unit not only led to incredible increases in width (from ~7 nm to 50-to-150 nm) and helical pitch (from ~20 nm to ~1 μm), but also fundamentally altered the underlying structure from a two-start cross-β bilayer to a variably wide β-sheet monolayer. In *Chapter 3*, we aimed to further investigate the extensive implications of heterochirality seen in diblock systems by extending our array to include triblock analogs. Providing support for generalizability beyond diblock KFE8, the four block chiral enantiomer pairs of KFE12 each produced highly distinct morphologies ranging from minimal 4-nm-wide homochiral fibrils (LLL, DDD) to micron-scale, semi-ordered, multilaminar cross-β structures (LDD, DLL). In *Chapter 4*, we describe the coassembly or self-sorting behavior of diblock chiral KFE8 isomer pairs, illustrating the intricate yet robust influence of stereocomplexation when applied to non-enantiomeric multi-component systems. In *Chapter 5*, we utilized the model antigen $OVA_{323-339}$ in C57BL/6 mice to determine whether the dramatic structural diversity described above inhibits the previously demonstrated self-adjuvancy and non-cytotoxicity of LL and DD KFE8-based vaccine scaffolds. By conjugating $OVA_{323-339}$ to 10% of monomers in a given

formulation, we produced structures with intermittent antigen presentation that outperformed the emulsifying adjuvant alum regardless of the chiral composition and patterning of the KFE systems serving as vaccine scaffolds.

The complex interplay between conventional associative forces and atypical steric effects has successfully produced a wide range of fascinating secondary structures and morphologies; however, the novelty and sheer intricacy of these architectures both motivate and complicate determination of the finest levels of detail. While observational techniques have provided an exquisite portrayal of an approach with virtually unlimited complexity, it is likely that definitively resolving specific molecular arrangements will continue to challenge researchers within the field. The promise shown by block heterochiral design elements will continue to drive their investigation, with the next step in our understanding most likely to result from rigorous exploration through molecular dynamics (MD) modeling, potentially informed by sophisticated spectroscopic techniques such as 2-D NMR (NOESY, HOESY). While time- and resource-intensive, MD has proven capable of informing unusual packing modes (*Chapter 2*) when performed in tandem with experimentation. Beyond structural insights, the tractable bulk material properties, variable degradability, and biocompatibility of these systems makes them highly attractive as drug-delivery depots, structural biomaterials, and cell-culture matrices. These applications, among innumerable others, are viable endpoints meriting the continued study of materials classes implementing block heterochirality as a powerful modulatory design tool.

References

Adair, J. H., Suvaci, E., & Sindel, J. (2001). Surface and Colloid Chemistry. In *Encyclopedia of Saterials: Science and Technology* (pp. 8996–9006). Elsevier Science Ltd.

Adler-Abramovich, L., Marco, P., Arnon, Z. A., Creasey, R. C. G., Michaels, T. C. T., Levin, A., Scurr, D. J., Roberts, C. J., Knowles, T. P. J., Tendler, S. J. B., & Gazit, E. (2016). Controlling the Physical Dimensions of Peptide Nanotubes by Supramolecular Polymer Coassembly. *ACS Nano*, *10*(8), 7436–7442. https://doi.org/10.1021/acsnano.6b01587

Aggeli, A., Boden, N., Carrick, L. M., McLeish, T. C. B., Nyrkova, I. A., & Semenov, A. N. (2006). Self-Assembling Peptide Gels. In R. G. Weiss & P. Terech (Eds.), *Molecular Gels: Materials with Self-Assembled Fibrillar Networks* (pp. 99–130). Springer Netherlands. https://doi.org/10.1007/1-4020-3689-2_4

Aggeli, A., Nyrkova, I. A., Bell, M., Harding, R., Carrick, L., McLeish, T. C. B., Semenov, A. N., & Boden, N. (2001). Hierarchical self-assembly of chiral rod-like molecules as a model for peptide β-sheet tapes, ribbons, fibrils, and fibers. *Proceedings of the National Academy of Sciences*, *98*(21), 11857–11862. https://doi.org/10.1073/pnas.191250198

Alexander, J., Sidney, J., Southwood, S., Ruppert, J., Oseroff, C., Maewal, A., Snoke, K., Serra, H. M., Kubo, R. T., Sette, A., & Grey, H. M. (1994). Development of high potency universal DR-restricted helper epitopes by modification of high affinity DR-blocking peptides. *Immunity*, *1*(9), 751–761. https://doi.org/10.1016/S1074-7613(94)80017-0

Al-Halifa, S., Zottig, X., Babych, M., Côté-Cyr, M., Bourgault, S., & Archambault, D. (2020). Harnessing the activation of Toll-like receptor 2/6 by self-assembled cross-β fibrils to design adjuvanted nanovaccines. *Nanomaterials*, *10*(10), 1981. https://doi.org/10.3390/nano10101981

An, J.-H., Kiyonga, A. N., Yoon, W., Park, M., Lim, C., Yun, Y., Park, G.-H., & Jung, K. (2017). Effect of Ionic Liquids on the Separation of Sucrose Crystals from a Natural Product Using Crystallization Techniques. *Crystals*, *7*(10), Article 10. https://doi.org/10.3390/cryst7100284

Appavu, R., Chesson, C. B., Koyfman, A. Y., Snook, J. D., Kohlhapp, F. J., Zloza, A., & Rudra, J. S. (2015). Enhancing the Magnitude of Antibody Responses through Biomaterial Stereochemistry. *ACS Biomaterials Science & Engineering*, *1*(7), 601–609. https://doi.org/10.1021/acsbiomaterials.5b00139

Babych, M., Bertheau-Mailhot, G., Zottig, X., Dion, J., Gauthier, L., Archambault, D., & Bourgault, S. (2018). Engineering and evaluation of amyloid assemblies as a nanovaccine against the Chikungunya virus. *Nanoscale*, *10*(41), 19547–19556. https://doi.org/10.1039/c8nr05948a

Bachmann, M. F., & Jennings, G. T. (2010). Vaccine delivery: A matter of size, geometry, kinetics and molecular patterns. *Nature Reviews Immunology*, *10*(11), 787–796. https://doi.org/10.1038/nri2868

Barth, A. (2007). Infrared spectroscopy of proteins. *Biochimica et Biophysica Acta (BBA) - Bioenergetics*, *1767*(9), 1073–1101. https://doi.org/10.1016/j.bbabio.2007.06.004

Batista, F. D., & Harwood, N. E. (2009). The who, how and where of antigen presentation to B cells. *Nature Reviews Immunology*, *9*(1), 15–27. https://doi.org/10.1038/nri2454

Beesley, J. L., Baum, H. E., Hodgson, L. R., Verkade, P., Banting, G. S., & Woolfson, D. N. (2018). Modifying self-assembled peptide cages to control internalization into mammalian cells. *Nano Letters*, *18*(9), 5933–5937. https://doi.org/10.1021/acs.nanolett.8b02633

Beevers, C. A., McDonald, T. R. R., Robertson, J. H., & Stern, F. (1952). The crystal structure of sucrose. *Acta Crystallographica*, *5*(5), Article 5. https://doi.org/10.1107/S0365110X52001908

Berndt, P., Fields, G. B., & Tirrell, M. (1995). Synthetic lipidation of peptides and amino acids: Monolayer structure and properties. *Journal of the American Chemical Society*, *117*(37), 9515–9522. https://doi.org/10.1021/ja00142a019

Biancalana, M., Makabe, K., Koide, A., & Koide, S. (2008). Aromatic cross-strand ladders control the structure and stability of β-rich peptide self-assembly mimics. *Journal of Molecular Biology*, *383*(1), 205–213. https://doi.org/10.1016/j.jmb.2008.08.031

Bowerman, C. J., Liyanage, W., Federation, A. J., & Nilsson, B. L. (2011). Tuning β-sheet peptide self-assembly and hydrogelation behavior by modification of sequence hydrophobicity and aromaticity. *Biomacromolecules*, *12*(7), 2735–2745. https://doi.org/10.1021/bm200510k

Bowerman, C. J., & Nilsson, B. L. (2012). Self-assembly of amphipathic β-sheet peptides: Insights and applications. *Biopolymers*, *98*(3), 169–184. https://doi.org/10.1002/bip.22058

Bowerman, C. J., Ryan, D. M., Nissan, D. A., & Nilsson, B. L. (2009). The effect of increasing hydrophobicity on the self-assembly of amphipathic beta-sheet peptides. *Molecular bioSystems*, *5*(9), 1058–1069. https://doi.org/10.1039/b904439f

Brown, G. M., & Levy, H. A. (1963). Sucrose: Precise Determination of Crystal and Molecular Structure by Neutron Diffraction. *Science*, *141*(3584), 921–923. https://doi.org/10.1126/science.141.3584.921

Brown, G. M., & Levy, H. A. (1973). Further refinement of the structure of sucrose based on neutron-diffraction data. *Acta Crystallographica Section B: Structural Crystallography and Crystal Chemistry*, *29*(4), Article 4. https://doi.org/10.1107/S0567740873003353

Brünger, A. T., Adams, P. D., Clore, G. M., DeLano, W. L., Gros, P., Grosse-Kunstleve, R. W., Jiang, J.-S., Kuszewski, J., Nilges, M., & Pannu, N. S. (1998). Crystallography & NMR system: A new software suite for macromolecular structure determination. *Acta Crystallographica Section D: Biological Crystallography*, *54*(5), 905–921.

Burkhard, P., Kammerer, R. A., Steinmetz, M. O., Bourenkov, G. P., & Aebi, U. (2000). The coiled-coil trigger site of the rod domain of cortexillin I unveils a distinct network of interhelical and intrahelical salt bridges. *Structure*, *8*(3), 223–230. https://doi.org/10.1016/S0969-2126(00)00100-3

Cable, J., Srikantiah, P., Crowe, J. E., Pulendran, B., Hill, A., Ginsberg, A., Koff, W., Mathew, A., Ng, T., Jansen, K., Glenn, G., Permar, S., Wilson, I., Weiner, D. B., Weissman, D., & Rappuoli, R. (2020). Vaccine innovations for emerging infectious diseases—A symposium report. *Annals of the New York Academy of Sciences*, *1462*(1), 14–26. https://doi.org/10.1111/nyas.14235

Caplan, M. R., Moore, P. N., Zhang, S., Kamm, R. D., & Lauffenburger, D. A. (2000). Self-Assembly of a β-Sheet Protein Governed by Relief of Electrostatic Repulsion Relative to van der Waals Attraction. *Biomacromolecules*, *1*(4), 627–631. https://doi.org/10.1021/bm005586w

Caplan, M. R., Schwartzfarb, E. M., Zhang, S., Kamm, R. D., & Lauffenburger, D. A. (2002a). Control of self-assembling oligopeptide matrix formation through systematic variation of amino acid sequence. *Biomaterials*, *23*(1), 219–227. https://doi.org/10.1016/S0142-9612(01)00099-0

Caplan, M. R., Schwartzfarb, E. M., Zhang, S., Kamm, R. D., & Lauffenburger, D. A. (2002b). Effects of systematic variation of amino acid sequence on the mechanical properties of a self-assembling, oligopeptide biomaterial. *Journal of Biomaterials Science, Polymer Edition*, *13*(3), 225–236. https://doi.org/10.1163/156856202320176493

Carpenter, S. M., Nunes-Alves, C., Booty, M. G., Way, S. S., & Behar, S. M. (2016). A higher activation threshold of memory CD8+ T cells has a fitness cost that is modified by TCR affinity during tuberculosis. *PLoS Pathogens*, *12*(1), e1005380. https://doi.org/10.1371/journal.ppat.1005380

Castelletto, V., Ryumin, P., Cramer, R., Hamley, I. W., Taylor, M., Allsop, D., Reza, M., Ruokolainen, J., Arnold, T., Hermida-Merino, D., Garcia, C. I., Leal, M. C., & Castaño, E. (2017). Self-Assembly and Anti-Amyloid Cytotoxicity Activity of Amyloid beta Peptide Derivatives. *Scientific Reports*, *7*, 43637. https://doi.org/10.1038/srep43637 https://www.nature.com/articles/srep43637#supplementary-information

Cava, F., Lam, H., de Pedro, M. A., & Waldor, M. K. (2011). Emerging knowledge of regulatory roles of D-amino acids in bacteria. *Cellular and Molecular Life Sciences : CMLS*, *68*(5), 817–831. https://doi.org/10.1007/s00018-010-0571-8

Chamberlain, A. K., MacPhee, C. E., Zurdo, J., Morozova-Roche, L. A., Hill, H. A. O., Dobson, C. M., & Davis, J. J. (2000). Ultrastructural Organization of Amyloid Fibrils byAtomic

Force Microscopy. *Biophysical Journal*, *79*(6), 3282–3293. https://doi.org/10.1016/S0006-3495(00)76560-X

Chauhan, G., Verma, A., Das, A., & Ojha, K. (2018). Rheological studies and optimization of Herschel-Bulkley flow parameters of viscous karaya polymer suspensions using GA and PSO algorithms. *Rheologica Acta*, *57*(3), 267–285. https://doi.org/10.1007/s00397-017-1060-x

Chen, P., & Hub, J. S. (2014). Validating solution ensembles from molecular dynamics simulation by wide-angle X-ray scattering data. *Biophysical Journal*, *107*(2), 435–447.

Chesson, C. B., Huante, M., Nusbaum, R. J., Walker, A. G., Clover, T. M., Chinnaswamy, J., Endsley, J. J., & Rudra, J. S. (2018). Nanoscale peptide self-assemblies boost BCG-primed cellular immunity against Mycobacterium tuberculosis. *Scientific Reports*, *8*(1), 1–14. https://doi.org/10.1038/s41598-018-31089-y

Chesson, C. B., Huelsmann, E. J., Lacek, A. T., Kohlhapp, F. J., Webb, M. F., Nabatiyan, A., Zloza, A., & Rudra, J. S. (2014). Antigenic peptide nanofibers elicit adjuvant-free CD8+ T cell responses. *Vaccine*, *32*(10), 1174–1180. https://doi.org/10.1016/j.vaccine.2013.11.047

Chothia, C., Levitt, M., & Richardson, D. (1977). Structure of proteins: Packing of α-helices and pleated sheets. *Proceedings of the National Academy of Sciences of the United States of America*, *74*(10), 4130–4134. https://doi.org/10.1073/pnas.74.10.4130

Chou, K. C., Pottle, M., Némethy, G., Ueda, Y., & Scheraga, H. A. (1982). Structure of β-sheets: Origin of the right-handed twist and of the increased stability of antiparallel over parallel sheets. *Journal of Molecular Biology*, *162*(1), 89–112. https://doi.org/10.1016/0022-2836(82)90163-2

Chou, P. Y., & Fasman, G. D. (1974). Conformational parameters for amino acids in helical, β-sheet, and random coil regions calculated from proteins. *Biochemistry*, *13*(2), 211–222.

Clover, T., ONeill, C., Appavu, R., Lokhande, G., Gaharwar, A., Posey, A., White, M., & Rudra, J. (2020). Self-Assembly of Block Heterochiral Peptides into Helical Tapes. *Journal of the American Chemical Society*, *142*(47), 19809–19813. https://doi.org/10.1021/jacs.9b09755

Collier, J. H., & Messersmith, P. B. (2003). Enzymatic modification of self-assembled peptide structures with tissue transglutaminase. *Bioconjugate Chemistry*, *14*(4), 748–755. https://doi.org/10.1021/bc034017t

Cui, H., Cheetham, A. G., Pashuck, E. T., & Stupp, S. I. (2014). Amino acid sequence in constitutionally isomeric tetrapeptide amphiphiles dictates architecture of one-dimensional nanostructures. *Journal of the American Chemical Society*, *136*(35), 12461–12468. https://doi.org/10.1021/ja507051w

Cui, H., Webber, M. J., & Stupp, S. I. (2010). Self-assembly of peptide amphiphiles: From molecules to nanostructures to biomaterials. *Biopolymers*, *94*(1), 1–18. https://doi.org/10.1002/bip.21328

Davies, R. P. W., & Aggeli, A. (2011). Self-assembly of amphiphilic β-sheet peptide tapes based on aliphatic side chains. *Journal of Peptide Science*, *17*(2), 107–114. https://doi.org/10.1002/psc.1335

Debye, P., & Bueche, A. M. (1949). Scattering by an Inhomogeneous Solid. *Journal of Applied Physics*, *20*(6), 518–525. https://doi.org/10.1063/1.1698419

Dellacherie, M. O., Seo, B. R., & Mooney, D. J. (2019). Macroscale biomaterials strategies for local immunomodulation. *Nature Reviews Materials*, *4*(6), 379–397. https://doi.org/10.1038/s41578-019-0106-3

Ding, Y., Liu, J., Lu, S., Igweze, J., Xu, W., Kuang, D., Zealey, C., Liu, D., Gregor, A., Bozorgzad, A., Zhang, L., Yue, E., Mujib, S., Ostrowski, M., & Chen, P. (2016). Self-assembling peptide for co-delivery of HIV-1 CD8+ T cells epitope and Toll-like receptor 7/8 agonists R848 to induce maturation of monocyte derived dendritic cell and augment polyfunctional cytotoxic T lymphocyte (CTL) response. *Journal of Controlled Release*, *236*, 22–30. https://doi.org/10.1016/j.jconrel.2016.06.019

Dong, A., Huang, P., & Caughey, W. S. (1990). Protein secondary structures in water from second-derivative amide I infrared spectra. *Biochemistry*, *29*(13), 3303–3308. https://doi.org/10.1021/bi00465a022

Eppler, H. B., & Jewell, C. M. (2020). Biomaterials as tools to decode immunity. *Advanced Materials*, *32*(13), 1903367. https://doi.org/10.1002/adma.201903367

Fishwick, C. W. G., Beevers, A. J., Carrick, L. M., Whitehouse, C. D., Aggeli, A., & Boden, N. (2003). Structures of helical β-tapes and twisted ribbons: The role of side-chain interactions on twist and bend behavior. *Nano Letters*, *3*(11), 1475–1479. https://doi.org/10.1021/nl034095p

Fraiha, M., Biagi, J. D., & Ferraz, A. C. de O. (2011). Rheological behavior of corn and soy mix as feed ingredients. *Food Science and Technology*, *31*(1), 129–134.

Friedrich, B. M., Beasley, D. W. C., & Rudra, J. S. (2016). Supramolecular peptide hydrogel adjuvanted subunit vaccine elicits protective antibody responses against West Nile virus. *Vaccine*, *34*(46), 5479–5482. https://doi.org/10.1016/j.vaccine.2016.09.044

Fries, C. N., Wu, Y., Kelly, S. H., Wolf, M., Votaw, N. L., Zauscher, S., & Collier, J. H. (2020). Controlled Lengthwise Assembly of Helical Peptide Nanofibers to Modulate CD8+ T-Cell Responses. *Advanced Materials*, *32*(39), 2003310. https://doi.org/10.1002/adma.202003310

Gao, Y., Shi, J., Yuan, D., & Xu, B. (2012). Imaging enzyme-triggered self-assembly of small molecules inside live cells. *Nature Communications*, *3*(1), 1033. https://doi.org/10.1038/ncomms2040

Garcia, A. M., Iglesias, D., Parisi, E., Styan, K. E., Waddington, L. J., Deganutti, C., De Zorzi, R., Grassi, M., Melchionna, M., Vargiu, A. V., & Marchesan, S. (2018). Chirality Effects on Peptide Self-Assembly Unraveled from Molecules to Materials. *Chem*, *4*(8), 1862–1876. https://doi.org/10.1016/j.chempr.2018.05.016

Gazit, E. (2002). A possible role for π-stacking in the self-assembly of amyloid fibrils. *The FASEB Journal*, *16*(1), 77–83. https://doi.org/10.1096/fj.01-0442hyp

Genchi, G. (2017). An overview on D-amino acids. *Amino Acids*, *49*(9), 1521–1533. https://doi.org/10.1007/s00726-017-2459-5

Giano, M. C., Pochan, D. J., & Schneider, J. P. (2011). Controlled biodegradation of self-assembling β-hairpin peptide hydrogels by proteolysis with matrix metalloproteinase-13. *Biomaterials*, *32*(27), 6471–6477. https://doi.org/10.1016/j.biomaterials.2011.05.052

Ginzburg, V. V., Chatterjee, T., Nakatani, A. I., & Van Dyk, A. K. (2018). Oscillatory and Steady Shear Rheology of Model Hydrophobically Modified Ethoxylated Urethane-Thickened Waterborne Paints. *Langmuir*, *34*(37), 10993–11002. https://doi.org/10.1021/acs.langmuir.8b01711

Goldschmidt, L., Teng, P. K., Riek, R., & Eisenberg, D. (2010). Identifying the amylome, proteins capable of forming amyloid-like fibrils. *Proceedings of the National Academy of Sciences of the United States of America*, *107*(8), 3487–3492. https://doi.org/10.1073/pnas.0915166107

Green, J. J. (2021). Immunoengineering has arrived. *Journal of Biomedical Materials Research Part A*, *109*(4), 397–403. https://doi.org/10.1002/jbm.a.37041

Grenfell, R. F. Q., Shollenberger, L. M., Samli, E. F., & Harn, D. A. (2015). Vaccine self-assembling immune matrix is a new delivery platform that enhances immune responses to recombinant HBsAg in mice. *Clinical and Vaccine Immunology : CVI*, *22*(3), 336–343. https://doi.org/10.1128/CVI.00714-14

Guo, Z., Song, Y., Wang, Y., Tan, T., Ji, Y., Zhang, G., Hu, J., & Zhang, Y. (2021). Macrochirality of Self-Assembled and Co-assembled Supramolecular Structures of a Pair of Enantiomeric Peptides. *Frontiers in Molecular Biosciences*, *8*. https://www.frontiersin.org/articles/10.3389/fmolb.2021.700964

Guvendiren, M., Lu, H. D., & Burdick, J. A. (2012). Shear-thinning hydrogels for biomedical applications. *Soft Matter*, *8*(2), 260–272. https://doi.org/10.1039/C1SM06513K

Haines-Butterick, L., Rajagopal, K., Branco, M., Salick, D., Rughani, R., Pilarz, M., Lamm, M. S., Pochan, D. J., & Schneider, J. P. (2007). Controlling hydrogelation kinetics by peptide design for three-dimensional encapsulation and injectable delivery of cells. *Proceedings*

of the National Academy of Sciences of the United States of America, *104*(19), 7791–7796. https://doi.org/10.1073/pnas.0701980104

Hamley, I. W. (2007). Peptide fibrillization. *Angewandte Chemie International Edition*, *46*(43), 8128–8147. https://doi.org/10.1002/anie.200700861

Hamley, I. W. (2011). Self-assembly of amphiphilic peptides. *Soft Matter*, *7*(9), 4122. https://doi.org/10.1039/c0sm01218a

Hansen, S. (2000). Bayesian estimation of hyperparameters for indirect Fourier transformation in small-angle scattering. *Journal of Applied Crystallography*, *33*(6), Article 6. https://doi.org/10.1107/S0021889800012930

Hansen, S. (2012). BayesApp: A web site for indirect transformation of small-angle scattering data. *Journal of Applied Crystallography*, *45*(3), 566–567. https://doi.org/10.1107/S0021889812014318

Hartgerink, J. D., Beniash, E., & Stupp, S. I. (2001). Self-assembly and mineralization of peptide-amphiphile nanofibers. *Science*, *294*(November), 1684–1689.

Hernandez, A., Hartgerink, J. D., & Young, S. (2023). Self-assembling peptides as immunomodulatory biomaterials. *Frontiers in Bioengineering and Biotechnology*, *11*. https://www.frontiersin.org/articles/10.3389/fbioe.2023.1139782

Hicks, M. R., Holberton, D. V., Kowalczyk, C., & Woolfson, D. N. (1997). Coiled-coil assembly by peptides with non-heptad sequence motifs. *Folding and Design*, *2*(3), 149–158. https://doi.org/10.1016/S1359-0278(97)00021-7

Hong, Y., Legge, R. L., Zhang, S., & Chen, P. (2003). Effect of amino acid sequence and pH on nanofiber formation of self-assembling peptides EAK16-II and EAK16-IV. *Biomacromolecules*, *4*(5), 1433–1442. https://doi.org/10.1021/bm0341374

Hotaling, N. A., Tang, L., Irvine, D. J., & Babensee, J. E. (2015). Biomaterial strategies for immunomodulation. *Annual Review of Biomedical Engineering*, *17*, 317–349. https://doi.org/10.1146/annurev-bioeng-071813-104814

Huang, Z.-H., Shi, L., Ma, J.-W., Sun, Z.-Y., Cai, H., Chen, Y.-X., Zhao, Y.-F., & Li, Y.-M. (2012). A totally synthetic, self-assembling, adjuvant-free MUC1 glycopeptide vaccine for cancer therapy. *Journal of the American Chemical Society*, *134*(21), 8730–8733. https://doi.org/10.1021/ja211725s

Hubbell, J. A., Thomas, S. N., & Swartz, M. A. (2009). Materials engineering for immunomodulation. *Nature*, *462*(7272), 449–460. https://doi.org/10.1038/nature08604

Hudalla, G. A., Modica, J. A., Tian, Y. F., Rudra, J. S., Chong, A. S., Sun, T., Mrksich, M., & Collier, J. H. (2013). A self-adjuvanting supramolecular vaccine carrying a folded protein antigen. *Advanced Healthcare Materials*, *2*(8), 1114–1119. https://doi.org/10.1002/adhm.201200435

Hudalla, G. A., Sun, T., Gasiorowski, J. Z., Han, H., Tian, Y. F., Chong, A. S., & Collier, J. H. (2014). Gradated assembly of multiple proteins into supramolecular nanomaterials. *Nature Materials*, *13*(8), 829–836. https://doi.org/10.1038/nmat3998

Humphrey, W., Dalke, A., & Schulten, K. (1996). VMD: Visual molecular dynamics. *Journal of Molecular Graphics*, *14*(1), 33–38, 27–28. https://doi.org/10.1016/0263-7855(96)00018-5

Huo, Y., Hu, J., Yin, Y., Liu, P., Cai, K., & Ji, W. (2023). Self-Assembling Peptide-Based Functional Biomaterials. *ChemBioChem*, *24*(2), e202200582. https://doi.org/10.1002/cbic.202200582

Hwang, W., Marini, D. M., Kamm, R. D., & Zhang, S. (2003). Supramolecular structure of helical ribbons self-assembled from a β-sheet peptide. *The Journal of Chemical Physics*, *118*(1), 389–397. https://doi.org/10.1063/1.1524618

Jackson, M., & Mantsch, H. H. (1995). The Use and Misuse of FTIR Spectroscopy in the Determination of Protein Structure. *Critical Reviews in Biochemistry and Molecular Biology*, *30*(2), 95–120. https://doi.org/10.3109/10409239509085140

J. Miles, A., & A. Wallace, B. (2016). Circular dichroism spectroscopy of membrane proteins. *Chemical Society Reviews*, *45*(18), 4859–4872. https://doi.org/10.1039/C5CS00084J

Kim, C. A., & Berg, J. M. (1993). Thermodynamic β-sheet propensities measured using a zinc-finger host peptide. *Nature*, *362*(6417), 267–270. https://doi.org/10.1038/362267a0

King, I. C., Gleixner, J., Doyle, L., Kuzin, A., Hunt, J. F., Xiao, R., Montelione, G. T., Stoddard, B. L., DiMaio, F., & Baker, D. (2015). Precise assembly of complex beta sheet topologies from de novo designed building blocks. *eLife*, *4*(DECEMBER2015), e11012. https://doi.org/10.7554/eLife.11012.001

Knight, C. J., & Hub, J. S. (2015). WAXSiS: a web server for the calculation of SAXS/WAXS curves based on explicit-solvent molecular dynamics. *Nucleic Acids Research*, *43*(W1), W225–W230.

Koshimizu, N., Bessho, M., Suzuki, S., Yuguchi, Y., Kitamura, S., & Hara, M. (2009). Gamma-crosslinked collagen gel without fibrils: Analysis of structure and heat stability. *Bioscience, Biotechnology, and Biochemistry*, *73*(9), 1915–1921. https://doi.org/10.1271/bbb.80771

Kreitler, D. F., Yao, Z., Steinkruger, J. D., Mortenson, D. E., Huang, L., Mittal, R., Travis, B. R., Forest, K. T., & Gellman, S. H. (2019). A hendecad motif is preferred for heterochiral coiled-coil formation. *Journal of the American Chemical Society*, *141*(4), 1583–1592. https://doi.org/10.1021/jacs.8b11246

Kyle, S., Aggeli, A., Ingham, E., & McPherson, M. J. (2010). Recombinant self-assembling peptides as biomaterials for tissue engineering. *Biomaterials*, *31*(36), 9395–9405. https://doi.org/10.1016/j.biomaterials.2010.08.051

Lahariya, C. (2016). Vaccine epidemiology: A review. *Journal of Family Medicine and Primary Care*, *5*(1), 7–15. https://doi.org/10.4103/2249-4863.184616

Larsen, A. H., & Pedersen, M. C. (2021). Experimental noise in small-angle scattering can be assessed using the Bayesian indirect Fourier transformation. *Journal of Applied Crystallography*, *54*(5), Article 5. https://doi.org/10.1107/S1600576721006877

Lau, C. Y. J., Fontana, F., Mandemaker, L. D. B., Wezendonk, D., Vermeer, B., Bonvin, A. M. J. J., de Vries, R., Zhang, H., Remaut, K., van den Dikkenberg, J., Medeiros-Silva, J., Hassan, A., Perrone, B., Kuemmerle, R., Gelain, F., Hennink, W. E., Weingarth, M., & Mastrobattista, E. (2020). Control over the fibrillization yield by varying the oligomeric nucleation propensities of self-assembling peptides. *Communications Chemistry*, *3*(1), Article 1. https://doi.org/10.1038/s42004-020-00417-7

Lee, N. R., Bowerman, C. J., & Nilsson, B. L. (2013a). Effects of varied sequence pattern on the self-assembly of amphipathic peptides. *Biomacromolecules*, *14*(9), 3267–3277. https://doi.org/10.1021/bm400876s

Lee, N. R., Bowerman, C. J., & Nilsson, B. L. (2013b). Sequence length determinants for self-assembly of amphipathic β-sheet peptides. *Biopolymers*, *100*(6), 738–750. https://doi.org/10.1002/bip.22248

Leon, E. J., Verma, N., Zhang, S., Lauffenburger, D. A., & Kamm, R. D. (1998). Mechanical properties of a self-assembling oligopeptide matrix. *Journal of Biomaterials Science, Polymer Edition*, *9*(3), 297–312. https://doi.org/10.1163/156856298X00668

Li, S., Zhu, W., Ye, C., Sun, W., Xie, H., Yang, X., Zhang, Q., & Ma, Y. (2020). Local mucosal immunization of self-assembled nanofibers elicits robust antitumor effects in an orthotopic model of mouse genital tumors. *Nanoscale*, *12*(5), 3076–3089. https://doi.org/10.1039/c9nr10334a

Li, X., Wang, Y., Wang, S., Liang, C., Pu, G., Chen, Y., Wang, L., Xu, H., Shi, Y., & Yang, Z. (2020). A strong CD8+ T cell-stimulating supramolecular hydrogel. *Nanoscale*, *12*(3), 2111–2117. https://doi.org/10.1039/C9NR08916K

Luo, Z., Wu, Q., Yang, C., Wang, H., He, T., Wang, Y., Wang, Z., Chen, H., Li, X., Gong, C., & Yang, Z. (2017). A powerful CD8+ T-cell stimulating D-tetra-peptide hydrogel as a very promising vaccine adjuvant. *Advanced Materials*, *29*(5), 1601776. https://doi.org/10.1002/adma.201601776

Luo, Z., & Zhang, S. (2012). Designer nanomaterials using chiral self-assembling peptide systems and their emerging benefit for society. *Chemical Society Reviews*, *41*(13), 4736. https://doi.org/10.1039/c2cs15360b

Luo, Z., Zhao, X., & Zhang, S. (2008). Structural dynamic of a self-assembling peptide d-EAK16 made of only D-amino acids. *PLoS One*, *3*(5), e2364. https://doi.org/10.1371/journal.pone.0002364

Makam, P., & Gazit, E. (2018). Minimalistic peptide supramolecular co-assembly: Expanding the conformational space for nanotechnology. *Chemical Society Reviews*, *47*(10), 3406–3420. https://doi.org/10.1039/C7CS00827A

Manalastas-Cantos, K., Konarev, P. V., Hajizadeh, N. R., Kikhney, A. G., Petoukhov, M. V., Molodenskiy, D. S., Panjkovich, A., Mertens, H. D. T., Gruzinov, A., Borges, C., Jeffries, C. M., Svergun, D. I., & Franke, D. (2021). ATSAS 3.0: Expanded functionality and new tools for small-angle scattering data analysis. *Journal of Applied Crystallography*, *54*(1), Article 1. https://doi.org/10.1107/S1600576720013412

Mandal, D., Nasrolahi Shirazi, A., & Parang, K. (2014). Self-assembly of peptides to nanostructures. *Organic and Biomolecular Chemistry*, *12*(22), 3544–3561. https://doi.org/10.1039/c4ob00447g

Mandel-Gutfreund, Y., & Gregoret, L. M. (2002). On the significance of alternating patterns of polar and non-polar residues in beta-strands. *Journal of Molecular Biology*, *323*(3), 453–461. https://doi.org/10.1016/S0022-2836(02)00973-7

Marchesan, S., Easton, C. D., Kushkaki, F., Waddington, L., & Hartley, P. G. (2012). Tripeptide self-assembled hydrogels: Unexpected twists of chirality. *Chemical Communications*, *48*(16), 2195–2197. https://doi.org/10.1039/C2CC16609G

Marchesan, S., Easton, C. D., Styan, K. E., Waddington, L. J., Kushkaki, F., Goodall, L., McLean, K. M., Forsythe, J. S., & Hartley, P. G. (2014). Chirality effects at each amino acid position on tripeptide self-assembly into hydrogel biomaterials. *Nanoscale*, *6*(10), 5172–5180. https://doi.org/10.1039/c3nr06752a

Marchesan, S., Qu, Y., Waddington, L. J., Easton, C. D., Glattauer, V., Lithgow, T. J., McLean, K. M., Forsythe, J. S., & Hartley, P. G. (2013). Self-assembly of ciprofloxacin and a tripeptide into an antimicrobial nanostructured hydrogel. *Biomaterials*, *34*(14), 3678–3687. https://doi.org/10.1016/j.biomaterials.2013.01.096

Marchesan, S., Styan, K. E., Easton, C. D., Waddington, L., & Vargiu, A. V. (2015). Higher and lower supramolecular orders for the design of self-assembled heterochiral tripeptide hydrogel biomaterials. *Journal of Materials Chemistry B*, *3*(41), 8123–8132. https://doi.org/10.1039/C5TB00858A

Marchesan, S., Waddington, L., D Easton, C., Winkler, D., Goodall, L., Forsythe, J., & G Hartley, P. (2012). Unzipping the role of chirality in nanoscale self-assembly of tripeptide hydrogels. *Nanoscale*, *4*, 6752–6760. https://doi.org/10.1039/c2nr32006a

Marini, D. M., Hwang, W., Lauffenburger, D. A., Zhang, S., & Kamm, R. D. (2002). Left-Handed Helical Ribbon Intermediates in the Self-Assembly of a β-Sheet Peptide. *Nano Letters*, *2*(4), 295–299. https://doi.org/10.1021/nl015697g

Mart, R. J., Osborne, R. D., Stevens, M. M., & Ulijn, R. V. (2006). Peptide-based stimuli-responsive biomaterials. *Soft Matter*, *2*(10), 822–835. https://doi.org/10.1039/b607706d

Melchionna, M., Styan, K. E., & Marchesan, S. (2016). The Unexpected Advantages of Using D-Amino Acids for Peptide Self- Assembly into Nanostructured Hydrogels for Medicine. *Current Topics in Medicinal Chemistry*, *16*(18), 2009–2018. https://doi.org/10.2174/1568026616999160212120302

Mohammadi, M., Dehghani, P., Mohseninia, A., Roozbehani, M., Hemphill, A., & Hesamizadeh, K. (2021). Incorporation of the Tat cell-penetrating peptide into nanofibers improves the respective antitumor immune response. *Journal of Cellular Physiology*, *236*, 1401–1417. https://doi.org/10.1002/jcp.29946

Mohammed, A., Miller, A. F., & Saiani, A. (2007). 3D Networks from Self-Assembling Ionic-Complementary Octa-Peptides. *Macromolecular Symposia*, *251*(1), 88–95. https://doi.org/10.1002/masy.200750512

Moore, A. N., & Hartgerink, J. D. (2017). Self-assembling multidomain peptide nanofibers for delivery of bioactive molecules and tissue regeneration. *Accounts of Chemical Research*, *50*(4), 714–722. https://doi.org/10.1021/acs.accounts.6b00553

Mora-Solano, C., Wen, Y., Han, H., Chen, J., Chong, A. S., Miller, M. L., Pompano, R. R., & Collier, J. H. (2017). Active immunotherapy for TNF-mediated inflammation using self-assembled peptide nanofibers. *Biomaterials*, *149*, 1–11. https://doi.org/10.1016/j.biomaterials.2017.09.031

Nagy, K. J., Giano, M. C., Jin, A., Pochan, D. J., & Schneider, J. P. (2011). Enhanced Mechanical Rigidity of Hydrogels Formed from Enantiomeric Peptide Assemblies. *Journal of the American Chemical Society*, *133*(38), 14975–14977. https://doi.org/10.1021/ja206742m

Nagy-Smith, K., Beltramo, P. J., Moore, E., Tycko, R., Furst, E. M., & Schneider, J. P. (2017). Molecular, Local, and Network-Level Basis for the Enhanced Stiffness of Hydrogel Networks Formed from Coassembled Racemic Peptides: Predictions from Pauling and Corey. *ACS Central Science*, *3*(6), 586–597. https://doi.org/10.1021/acscentsci.7b00115

O'Neill, C. L., Shrimali, P. C., Clapacs, Z. P., Files, M. A., & Rudra, J. S. (2021). Peptide-based supramolecular vaccine systems. *Acta Biomaterialia*. https://doi.org/10.1016/J.ACTBIO.2021.05.003

Pantoja-Uceda, D., Santiveri, C. M., & Jiménez, M. A. (2006). De novo design of monomeric β-hairpin and β-sheet peptides. *Methods in Molecular Biology (Clifton, N.J.)*, *340*, 27–51.

Paramonov, S. E., Jun, H. W., & Hartgerink, J. D. (2006). Self-assembly of peptide-amphiphile nanofibers: The roles of hydrogen bonding and amphiphilic packing. *Journal of the American Chemical Society*, *128*(22), 7291–7298. https://doi.org/10.1021/ja060573x

Parry, D. A. D. (2006). Hendecad repeat in segment 2A and linker L2 of intermediate filament chains implies the possibility of a right-handed coiled-coil structure. *Journal of Structural Biology*, *155*(2), 370–374. https://doi.org/10.1016/j.jsb.2006.03.017

Pauling, L., & Corey, R. B. (1951). Configurations of polypeptide chains with favored orientations around single bonds: Two new pleated sheets. *Proceedings of the National Academy of Sciences of the United States of America*, *37*(11), 729–740. https://doi.org/10.1073/pnas.37.11.729

Pauling, L., & Corey, R. B. (1953). Two Rippled-Sheet Configurations of Polypeptide Chains, and a Note about the Pleated Sheets. *Proceedings of the National Academy of Sciences of the United States of America*, *39*(4), 253–256. https://doi.org/10.1073/pnas.39.4.253

Phillips, J. C., Hardy, D. J., Maia, J. D. C., Stone, J. E., Ribeiro, J. V., Bernardi, R. C., Buch, R., Fiorin, G., Hénin, J., Jiang, W., McGreevy, R., Melo, M. C. R., Radak, B. K., Skeel, R. D., Singharoy, A., Wang, Y., Roux, B., Aksimentiev, A., Luthey-Schulten, Z., … Tajkhorshid, E. (2020). Scalable molecular dynamics on CPU and GPU architectures with NAMD. *The Journal of Chemical Physics*, *153*(4), 044130. https://doi.org/10.1063/5.0014475

Quinn, T. P., Tweedy, N. B., Williams, R. W., Richardson, J. S., & Richardson, D. C. (1994). Betadoublet: De novo design, synthesis, and characterization of a β-sandwich protein. *Proceedings of the National Academy of Sciences of the United States of America*, *91*(19), 8747–8751. https://doi.org/10.1073/pnas.91.19.8747

Raman, S., Machaidze, G., Lustig, A., Aebi, U., & Burkhard, P. (2006). Structure-based design of peptides that self-assemble into regular polyhedral nanoparticles. *Nanomedicine: Nanotechnology, Biology, and Medicine*, *2*(2), 95–102. https://doi.org/10.1016/j.nano.2006.04.007

Raymond, D. M., & Nilsson, B. L. (2018). Multicomponent peptide assemblies. *Chemical Society Reviews*, *47*(10), 3659–3720. https://doi.org/10.1039/C8CS00115D

Richardson, J. S. (1977). β-Sheet topology and the relatedness of proteins. *Nature*, *268*(5620), 495–500. https://doi.org/10.1038/268495a0

Rivier, J., Brown, M., & Vale, W. (1975). D-Trp8-somatostatin: An analog of somatostatin more potent than the native molecule. *Biochemical and Biophysical Research Communications*, *65*(2), 746–751. https://doi.org/10.1016/S0006-291X(75)80208-7

Rudra, J. S., Ding, Y., Neelakantan, H., Ding, C., Appavu, R., Stutz, S., Snook, J. D., Chen, H., Cunningham, K. A., & Zhou, J. (2016). Suppression of Cocaine-Evoked Hyperactivity by Self-Adjuvanting and Multivalent Peptide Nanofiber Vaccines. *ACS Chemical Neuroscience*, *7*(5), 546–552. https://doi.org/10.1021/acschemneuro.5b00345

Rudra, J. S., Mishra, S., Chong, A. S., Mitchell, R. A., Nardin, E. H., Nussenzweig, V., & Collier, J. H. (2012). Self-assembled peptide nanofibers raising durable antibody responses against a malaria epitope. *Biomaterials*, *33*(27), 6476–6484. https://doi.org/10.1016/j.biomaterials.2012.05.041

Rudra, J. S., Sun, T., Bird, K. C., Daniels, M. D., Gasiorowski, J. Z., Chong, A. S., & Collier, J. H. (2012). Modulating Adaptive Immune Responses to Peptide Self-Assemblies. *ACS Nano*, *6*(2), 1557–1564. https://doi.org/10.1021/nn204530r

Rudra, J. S., Tian, Y. F., Jung, J. P., & Collier, J. H. (2010). A self-assembling peptide acting as an immune adjuvant. *Proceedings of the National Academy of Sciences*, *107*(2), 622. https://doi.org/10.1073/pnas.0912124107

Rughani, R. V., Salick, D. A., Lamm, M. S., Yucel, T., Pochan, D. J., & Schneider, J. P. (2009). Folding, self-assembly, and bulk material properties of a de novo designed three-stranded β-sheet hydrogel. *Biomacromolecules*, *10*(5), 1295–1304. https://doi.org/10.1021/bm900113z

Sahoo, J. K., Braegelman, A. S., & Webber, M. J. (2018). Immunoengineering with supramolecular peptide biomaterials. *Journal of the Indian Institute of Science*, *98*(1), 69–79. https://doi.org/10.1007/s41745-018-0060-x

Sanchez, C. J., Akers, K. S., Romano, D. R., Woodbury, R. L., Hardy, S. K., Murray, C. K., & Wenke, J. C. (2014). D-Amino Acids Enhance the Activity of Antimicrobials against Biofilms of Clinical Wound Isolates of Staphylococcus aureus and Pseudomonas aeruginosa. *Antimicrobial Agents and Chemotherapy*, *58*(8), 4353. https://doi.org/10.1128/AAC.02468-14

Sarroukh, R., Goormaghtigh, E., Ruysschaert, J.-M., & Raussens, V. (2013). ATR-FTIR: A "rejuvenated" tool to investigate amyloid proteins. *Biochimica et Biophysica Acta (BBA) - Biomembranes*, *1828*(10), 2328–2338. https://doi.org/10.1016/j.bbamem.2013.04.012

Schneider, J. P., Pochan, D. J., Ozbas, B., Rajagopal, K., Pakstis, L., & Kretsinger, J. (2002). Responsive Hydrogels from the Intramolecular Folding and Self-Assembly of a Designed Peptide. *Journal of the American Chemical Society*, *124*(50), 15030–15037. https://doi.org/10.1021/ja027993g

Schneidman-Duhovny, D., Hammel, M., & Sali, A. (2010). FoXS: A web server for rapid computation and fitting of SAXS profiles. *Nucleic Acids Research*, *38*(Web Server issue), W540-544. https://doi.org/10.1093/nar/gkq461

Seroski, D. T., Dong, X., Wong, K. M., & Hudalla, G. A. (2020). Charge guides pathway selection in β-sheet fibrillizing peptide co-assembly. *Communications Chemistry*, *3*(172), 1–11. https://doi.org/10.1038/s42004-020-00414-w

Shores, L. S., Kelly, S. H., Hainline, K. M., Suwanpradid, J., MacLeod, A. S., & Collier, J. H. (2020). Multifactorial design of a supramolecular peptide anti-IL-17 vaccine toward the treatment of psoriasis. *Frontiers in Immunology*, *11*, 1855. https://doi.org/10.3389/fimmu.2020.01855

Si, Y., Wen, Y., Kelly, S. H., Chong, A. S., & Collier, J. H. (2018). Intranasal delivery of adjuvant-free peptide nanofibers elicits resident CD8+ T cell responses. *Journal of Controlled Release*, *282*(April), 120–130. https://doi.org/10.1016/j.jconrel.2018.04.031

Stendahl, J. C., Rao, M. S., Guler, M. O., & Stupp, S. I. (2006). Intermolecular forces in the self-assembly of peptide amphiphile nanofibers. *Advanced Functional Materials*, *16*(4), 499–508. https://doi.org/10.1002/adfm.200500161

Svergun, D., Barberato, C., & Koch, M. H. J. (1995). CRYSOL – a Program to Evaluate X-ray Solution Scattering of Biological Macromolecules from Atomic Coordinates. *Journal of Applied Crystallography*, *28*(6), Article 6. https://doi.org/10.1107/S0021889895007047

Swanekamp, R. J., DiMaio, J. T. M., Bowerman, C. J., & Nilsson, B. L. (2012). Coassembly of Enantiomeric Amphipathic Peptides into Amyloid-Inspired Rippled β-Sheet Fibrils. *Journal of the American Chemical Society*, *134*(12), 5556–5559. https://doi.org/10.1021/ja301642c

Swanekamp, R. J., Welch, J. J., & Nilsson, B. L. (2014). Proteolytic stability of amphipathic peptide hydrogels composed of self-assembled pleated β-sheet or coassembled rippled β-sheet fibrils. *Chemical Communications*, *50*(70), 10133–10136. https://doi.org/10.1039/C4CC04644G

Taraban, M. B., Feng, Y., Hammouda, B., Hyland, L. L., & Yu, Y. B. (2012). Chirality-Mediated Mechanical and Structural Properties of Oligopeptide Hydrogels. *Chemistry of Materials*, *24*(12), 2299–2310. https://doi.org/10.1021/cm300422q

Tateishi, T., Kojima, T., & Hiraoka, S. (2018). Chiral self-sorting process in the self-assembly of homochiral coordination cages from axially chiral ligands. *Communications Chemistry*, *1*(1), Article 1. https://doi.org/10.1038/s42004-018-0020-4

Toyama, B. H., & Weissman, J. S. (2011). Amyloid structure: Conformational diversity and consequences. *Annual Review of Biochemistry*, *80*, 557–585. https://doi.org/10.1146/annurev-biochem-090908-120656

Tria, G., Mertens, H. D. T., Kachala, M., & Svergun, D. I. (2015). Advanced ensemble modelling of flexible macromolecules using X-ray solution scattering. *IUCrJ*, *2*(2), 207–217. https://doi.org/10.1107/S205225251500202X

Truby, R. L., & Lewis, J. A. (2016). Printing soft matter in three dimensions. *Nature*, *540*, 371. https://doi.org/10.1038/nature21003

United States Food and Drug Administration. (2020). *Vaccines licensed for use in the US*. https://www.fda.gov/vaccines-blood-biologics/vaccines/vaccines-licensed-use-united-states

Vargiu, A. V., Iglesias, D., Styan, K. E., Waddington, L. J., Easton, C. D., & Marchesan, S. (2016). Design of a hydrophobic tripeptide that self-assembles into amphiphilic superstructures forming a hydrogel biomaterial. *Chemical Communications*, *52*(35), 5912–5915. https://doi.org/10.1039/C5CC10531E

Vetter, V., Denizer, G., Friedland, L. R., Krishnan, J., & Shapiro, M. (2018). Understanding modern-day vaccines: What you need to know. *Annals of Medicine*, *50*(2), 110–120. https://doi.org/10.1080/07853890.2017.1407035

Villarreal, R., & Casale, T. B. (2020). Commonly used adjuvant human vaccines: Advantages and side effects. *Journal of Allergy and Clinical Immunology: In Practice*, *8*(9), 2953–2957. https://doi.org/10.1016/j.jaip.2020.04.045

Wade, D., Boman, A., Wåhlin, B., Drain, C. M., Andreu, D., Boman, H. G., & Merrifield, R. B. (1990). All-D amino acid-containing channel-forming antibiotic peptides. *Proceedings of the National Academy of Sciences*, *87*(12), 4761. https://doi.org/10.1073/pnas.87.12.4761

Wang, K., Keasling, J. D., & Muller, S. J. (2005). Effects of the sequence and size of non-polar residues on self-assembly of amphiphilic peptides. *International Journal of Biological Macromolecules*, *36*(4), 232–240. https://doi.org/10.1016/j.ijbiomac.2005.06.006

Wang, Y., Li, X., Zhang, Y., Wang, L., & Yang, Z. (2019). A supramolecular hydrogel to boost the production of antibodies for phosphorylated proteins. *Chemical Communications*, *55*(82), 12388–12391. https://doi.org/10.1039/C9CC05633E

Wang, Z., Liang, C., Shi, F., He, T., Gong, C., Wang, L., & Yang, Z. (2017). Cancer vaccines using supramolecular hydrogels of NSAID-modified peptides as adjuvants abolish tumorigenesis. *Nanoscale*, *9*(37), 14058–14064. https://doi.org/10.1039/C7NR04990K

Wang, Z., Shang, Y., Tan, Z., Li, X., Li, G., Ren, C., Wang, F., Yang, Z., & Liu, J. (2020). A supramolecular protein chaperone for vaccine delivery. *Theranostics*, *10*(2), 657–670. https://doi.org/10.7150/thno.39132

Woolfson, D. N. (2005). The design of coiled-coil structures and assemblies. *Advances in Protein Chemistry*, *70*(04), 79–112. https://doi.org/10.1016/S0065-3233(05)70004-8

Wu, Y., & Collier, J. H. (2017). α-Helical coiled-coil peptide materials for biomedical applications. *Wiley Interdisciplinary Reviews: Nanomedicine and Nanobiotechnology*, *9*(2), e1424. https://doi.org/10.1002/wnan.1424

Wu, Y., Norberg, P. K., Reap, E. A., Congdon, K. L., Fries, C. N., Kelly, S. H., Sampson, J. H., Conticello, V. P., & Collier, J. H. (2017). A supramolecular vaccine platform based on α-helical peptide nanofibers. *ACS Biomaterials Science and Engineering*, *3*(12), 3128–3132. https://doi.org/10.1021/acsbiomaterials.7b00561

Xie, Y.-Y., Qin, X.-T., Zhang, J., Sun, M.-Y., Wang, F.-P., Huang, M., Jia, S.-R., Qi, W., Wang, Y., & Zhong, C. (2022). Self-assembly of peptide nanofibers with chirality-encoded antimicrobial activity. *Journal of Colloid and Interface Science*, *622*, 135–146. https://doi.org/10.1016/j.jcis.2022.04.058

Xu, Y., Wang, Y., Yang, Q., Liu, Z., Xiao, Z., Le, Z., Yang, Z., & Yang, C. (2019). A versatile supramolecular nanoadjuvant that activates NF-κB for cancer immunotherapy. *Theranostics*, *9*(11), 3388–3397. https://doi.org/10.7150/thno.34031

Yang, C., Chu, L., Zhang, Y., Shi, Y., Liu, J., Liu, Q., Fan, S., Yang, Z., Ding, D., Kong, D., & Liu, J. (2015). Dynamic biostability, biodistribution, and toxicity of L/D-peptide-based supramolecular nanofibers. *ACS Applied Materials and Interfaces*, *7*(4), 2735–2744. https://doi.org/10.1021/am507800e

Yang, C., Shi, F., Li, C., Wang, Y., Wang, L., & Yang, Z. (2018). Single Dose of Protein Vaccine with Peptide Nanofibers As Adjuvants Elicits Long-Lasting Antibody Titer. *ACS Biomaterials Science & Engineering*, *4*(6), 2000–2006. https://doi.org/10.1021/acsbiomaterials.7b00488

Yang, S., Wang, M., Wang, T., Sun, M., Huang, H., Shi, X., Duan, S., Wu, Y., Zhu, J., & Liu, F. (2023). Self-assembled short peptides: Recent advances and strategies for potential pharmaceutical applications. *Materials Today Bio*, *20*, 100644. https://doi.org/10.1016/j.mtbio.2023.100644

Yokoi, H., Kinoshita, T., & Zhang, S. (2005). Dynamic reassembly of peptide RADA16 nanofiber scaffold. *Proceedings of the National Academy of Sciences of the United States of America*, *102*(24), 8414–8419. https://doi.org/10.1073/pnas.0407843102

Yousefpour, P., Ni, K., & Irvine, D. J. (2023). Targeted modulation of immune cells and tissues using engineered biomaterials. *Nature Reviews Bioengineering*, *1*(2), Article 2. https://doi.org/10.1038/s44222-022-00016-2

Yu, Y. C., Berndt, P., Tirrell, M., & Fields, G. B. (1996). Self-assembling amphiphiles for construction of protein molecular architecture. *Journal of the American Chemical Society*, *118*(50), 12515–12520. https://doi.org/10.1021/ja9627656

Zacco, E., Anish, C., Martin, C. E., Berlepsch, H. V., Brandenburg, E., Seeberger, P. H., & Koksch, B. (2015). A self-assembling peptide scaffold for the multivalent presentation of antigens. *Biomacromolecules*, *16*(7), 2188–2197. https://doi.org/10.1021/acs.biomac.5b00572

Zhang, H., Park, J., Jiang, Y., & Woodrow, K. A. (2017). Rational design of charged peptides that self-assemble into robust nanofibers as immune-functional scaffolds. *Acta Biomaterialia*, *55*, 183–193. https://doi.org/10.1016/j.actbio.2017.03.041

Zhang, S. (2020). Self-assembling peptides: From a discovery in a yeast protein to diverse uses and beyond. *Protein Science*, *29*(11), 2281–2303. https://doi.org/10.1002/pro.3951

Zhang, S., & Altman, M. (1999). Peptide self-assembly in functional polymer science and engineering. *Reactive and Functional Polymers*, *41*(1), 91–102. https://doi.org/10.1016/S1381-5148(99)00031-0

Zhang, S., Holmes, T., Lockshin, C., & Rich, A. (1993). Spontaneous assembly of a self-complementary oligopeptide to form a stable macroscopic membrane. *Proceedings of the National Academy of Sciences*, *90*(8), 3334. https://doi.org/10.1073/pnas.90.8.3334

Zhang, S., Marini, D. M., Hwang, W., & Santoso, S. (2002). Design of nanostructured biological materials through self-assembly of peptides and proteins. *Current Opinion in Chemical Biology*, *6*(6), 865–871. https://doi.org/10.1016/s1367-5931(02)00391-5

Zhao, G., Chandrudu, S., Skwarczynski, M., & Toth, I. (2017). The application of self-assembled nanostructures in peptide-based subunit vaccine development. *European Polymer Journal*, *93*, 670–681. https://doi.org/10.1016/j.eurpolymj.2017.02.014

Zheng, Y., Mao, K., Chen, S., & Zhu, H. (2021). Chirality Effects in Peptide Assembly Structures. *Frontiers in Bioengineering and Biotechnology*, *9*. https://www.frontiersin.org/articles/10.3389/fbioe.2021.703004

Zhou, P., Deng, L., Wang, Y., Lu, J. R., & Xu, H. (2016). Different nanostructures caused by competition of intra- and inter-beta-sheet interactions in hierarchical self-assembly of short peptides. *Journal of Colloid and Interface Science*, *464*, 219–228. https://doi.org/10.1016/j.jcis.2015.11.030